

NUREG/CR-0522
LA-7567-PR

Progress Report

Nuclear Reactor Safety

Quarterly Progress Report

July 1—September 30, 1978

University of California

120555008386 2 ANR487B3
US ARC
SECY PUBLIC DOCUMENT ROOM
BRANCH CHIEF
WASHINGTON DC 20555

79 08070803

508 • 034



LOS ALAMOS SCIENTIFIC LABORATORY

Post Office Box 1663 Los Alamos, New Mexico 87545

Affirmative Action/Equal Opportunity Employer

The four most recent reports in this series, unclassified, are LA-7039-PR, LA-7195-PR, NUREG/CR-0062 LA-7278-PR, and NUREG/CR-0385 LA-7481-PR.

This work was partially supported by the US Department of Energy, Division of Reactor Development and Demonstration.

NOTICE

This report was prepared as an account of work sponsored by an agency of the United States Government. Neither the United States Government nor any agency thereof, or any of their employees, makes any warranty, expressed or implied, or assumes any legal liability or responsibility for any third party's use, or the results of such use, of any information, apparatus, product or process disclosed in this report, or represents that its use by such third party would not infringe privately owned rights.

The views expressed in this report are not necessarily those of the US Nuclear Regulatory Commission.

UNITED STATES
DEPARTMENT OF ENERGY
CONTRACT W-7405-ENG. 36

508 033

NUREG/CR-0522
LA-7567-PR
Progress Report
R4, R7, and R8

Nuclear Reactor Safety
Quarterly Progress Report
July 1—September 30, 1978

Compiled by
James F. Jackson
Michael G. Stevenson

Manuscript submitted: November 1978
Date published: December 1978

Prepared for Office of Nuclear Regulatory Research
Division of Reactor Safety Research
Office of Nuclear Reactor Regulation
Division of Systems Safety
US Nuclear Regulatory Commission
Washington, DC 20555



508 036

CONTENTS

ABSTRACT - - - - -	-
I. INTRODUCTION - - - - -	1
(J. F. Jackson and M. G. Stevenson, Q-DO)	
II. LWR SAFETY RESEARCH - - - - -	2
(J. F. Jackson, Q-DO)	
A. TRAC Code Development and Verification - - - - -	2
(J. C. Vigil and R. J. Pryor, Q-6)	
1. TRAC Code Development - - - - -	3
(J. M. Sicilian, Q-6)	
a. Standardization of Input and Output Routines - - - - -	3
(R. J. Pryor, Q-6)	
b. Dynamic Memory Allocation - - - - -	4
(J. M. Sicilian, Q-6)	
c. Improvements to the Program Maintenance Code, HORSE - - - - -	4
(R. P. Harper, Q-6)	
d. Improved Overlay Structure - - - - -	4
(J. M. Sicilian, Q-6)	
e. Consistent Database for One-Dimensional Components - - - - -	4
(J. M. Sicilian, Q-6)	
f. Improved Graphics Postprocessor - - - - -	4
(J. C. Ferguson, Q-6)	
2. Fluid Dynamics Methods - - - - -	5
(D. R. Liles, Q-6)	
a. One-Dimensional, Two-Fluid, Hydrodynamics - - - - -	5
(J. H. Mahaffy, Q-6)	
b. Droplet Field - - - - -	5
(D. R. Liles, Q-6)	
3. Heat Transfer Methods - - - - -	6
(W. L. Kirchner, Q-6)	
a. BWR Radiation Heat Transfer - - - - -	6
(D. A. Mandell, Q-6)	

CONTENTS (cont)

c.	Quench Front Modeling - - - - -	9
	(W. L. Kirchner and R. J. Pryor, Q-6)	
4.	TRAC Code Assessment - - - - -	11
	(K. A. Williams, Q-6)	
a.	TRAC Calculation of U.S. Standard Problem 8 - - - - -	12
	(J. R. Ireland and P. B. Bleiweis, Q-6)	
b.	TRAC Calculation of Standard Problem 6 -	21
	(K. A. Williams, Q-6)	
c.	TRAC Calculation of Marviken Full-Scale Critical Flow Test 4 - - - - -	27
	(G. J. E. Willcutt, Jr. and R. J. Pryor, Q-6)	
5.	TRAC Sensitivity Analysis - - - - -	30
	(M. D. McKay, S-1)	
B.	TRAC Applications - - - - -	32
	(J. C. Vigil and P. B. Bleiweis, Q-6)	
1.	PWR ECCS Bypass Sensitivity Study - - - - -	33
	(P. B. Bleiweis, K. A. Williams, J. R. Ireland, D. Dobranich, D. R. Liles, and J. J. Pyun, Q-6)	
2.	TRAC Calculations of the Japanese Cylindrical Core Test Facility - - - - -	41
	(D. Dobranich, Q-6)	
3.	TRAC Calculations of the INEL Air-Water Test Series - - - - -	47
	(M. M. Giles, INEL and P. B. Bleiweis, Q-6)	
C.	Thermal-Hydraulic Research for Reactor Safety Analysis - - - - -	53
	(C. W. Hirt, T-3)	
1.	Steam Source Calculations for Large-Scale Japanese and German Experiments - - - - -	53
	(W. C. Rivard and M. D. Torrey, T-3)	
2.	Large-Scale Critical Flow Analysis - - - - -	55
	(J. R. Travis and W. C. Rivard, T-3)	
3.	Droplet Spray Modeling - - - - -	59
	(J. K. Dukowicz and T. D. Butler, T-3)	

CONTENTS (cont)

a.	Governing Equations and Solution Procedures - - - - -	60
b.	Numerical Examples - - - - -	62
D.	LWR Experiments - - - - - (H. H. Helmick, Q-8)	65
1.	Video Stereogrammetry - - - - - (C. R. Mansfield and J. F. Spalding, Q-8)	65
a.	Steam Test Loop - - - - -	66
b.	Video Electronics Development - - - - -	66
c.	VS Probe Development - - - - -	66
d.	Heat Pipe Cooling - - - - -	66
e.	PKL Adaptor - - - - -	67
2.	Upper Plenum De-entrainment Experiment - - - - - (V. S. Starkovich, Q-8; and W. L. Kirchner and J. C. Dallman, Q-6)	67
3.	Hot-Film Anemometer - - - - - (P. F. Bird, Q-8)	69
4.	Data Acquisition System - - - - - (P. F. Bird, Q-8)	71
III.	LMFBR SAFETY RESEARCH - - - - -	72
	(M. G. Stevenson, Q-DO; and J. E. Boudreau, Q-7)	
A.	SIMMER Code Development and Applications - - - - -	72
	(L. L. Smith and C. R. Bell, Q-7)	
1.	Application of Statistical Correlation Methods to the Sensitivity Analysis of SIMMER-II Input Parameters - - - - -	73
	(R. D. Burns, III, Q-7)	
2.	SIMMER-II Analysis of the R-7 TREAT Test - - -	82
	(W. R. Bohl, Q-7)	
3.	Minimizing Errors in the Fertile/Fissile Fuel Model in SIMMER-II - - - - -	85
	(R. G. Steinke, Q-7)	

CONTENTS (cont)

B.	SIMMER Verification - - - - -	87
	(J. H. Scott, Q-7; and H. H. Helmick, Q-8)	
1.	Analysis of SRI International Expansion Experiments - - - - -	87
	(P. E. Rexroth and A. J. Suo-Anttila, Q-7)	
2.	Feasibility Study of UCS Simulation Experiment - - - - -	93
	(E. J. Chapyak, Q-7; and V. S. Starkovich, Q-8)	
C.	STF Study - - - - -	94
	(M. G. Stevenson, Q-DO)	
1.	STF Simulation with Critical Assemblies - - -	94
	(A. E. Evans, B. Pena, R. E. Malenfant, L. R. Creel, E. A. Plassmann, and M. B. Diaz, Q-14)	
IV.	HTGR SAFETY RESEARCH - - - - -	98
	(M. G. Stevenson, Q-DO)	
A.	Structural Investigations - - - - -	98
	(C. A. Anderson, Q-13)	
1.	Code Development for Analysis of Prestressed Concrete Reactor Vessels (PCRVs) - - - - -	98
	(C. A. Anderson and P. D. Smith, Q-13)	
2.	Experimental Seismic Program - - - - -	99
	(R. C. Dove and W. E. Dunwoody, Q-13)	
B.	Phenomena Modeling and Systems Analysis - - - - -	103
	(P. A. Secker, Q-6)	
1.	FSV Modeling - - - - -	103
	(P. A. Secker, G. J. E. Willcutt, Jr., and P. L. Rivera, Q-6; R. B. Lazarus, C-3; and T. McDonald, E-4)	
2.	Reactor Containment Analysis - - - - -	104
	(P. A. Secker and D. Dube, Q-6)	
3.	Feedwater Transients - - - - -	108
	(P. A. Secker, Q-6; and R. B. Lazarus, C-3)	
4.	Water Equation of State - - - - -	111
	(P. A. Secker, Q-6)	

CONTENTS (cont)

5.	LASAN Improvements - - - - -	113
	(P. A. Secker, Q-6; and R. B. Lazarus, C-3)	
V.	GCFR CORE DISRUPTIVE TEST PROGRAM - - - - -	114
	(D. L. Hanson, Q-13)	
A.	Program Planning - - - - -	114
	(D. L. Hanson, Q-13)	
B.	Analysis - - - - -	115
	(A. J. Giger, D. L. Hanson, and C. Prenger, Q-13)	
1.	Spacer-grid/Cladding Friction - - - - -	115
2.	FLS-1 Postmortem Analysis - - - - -	116
3.	DMFT Support Frame Thermal Analyses - - - - -	118
C.	Design - - - - -	119
	(A. J. Giger and W. E. Dunwoody, Q-13)	
D.	Fabrication and Procurement - - - - -	122
	(W. E. Dunwoody, Q-13)	
E.	Testing - - - - -	122
	(R. Renfro and D. L. Hanson, Q-13)	
VI.	CONTAINMENT SYSTEMS EVALUATIONS AND STUDIES - - - - -	124
	(R. G. Gido, Q-6)	
A.	Containment Evaluation - - - - -	124
	(R. G. Gido, Q-6)	
B.	Containment Subcompartment Analysis - - - - -	124
1.	Insulation Blockage Sensitivity Study - - - - -	?
	(J. S. Gilbert, Q-6)	
3.	Loss-Coefficient Compressibility Effects - - - - -	129
	(A. Koestel, LASL Consultant; and R. G. Gido, Q-6)	
	REFERENCES - - - - -	133

FIGURES

Fig. 1.	Quench front position history for FLECHT Test No. 3541. - - - - -	10
Fig. 2.	TRAC component schematic for Standard Problem 8 (Test S-06-3). - - - - -	13
Fig. 3.	TRAC vessel noding for Standard Problem 8. - - - -	13
Fig. 4.	Axial power distribution for Standard Problem 8. -	13
Fig. 5.	Combined ECC volumetric flow rate (LPIS, HPIS, and accumulator) for Standard Problem 8. - - - -	14
Fig. 6.	S-06-3 Semiscale LOFT counterpart nozzle. - - - -	15
Fig. 7.	Suppression tank pressure for Standard Problem 8. -	15
Fig. 8.	Upper plenum pressure for Standard Problem 8. - - -	18
Fig. 9.	Pump inlet density -- Standard Problem 8. - - - -	18
Fig. 10.	Intact loop cold-leg density -- Standard Problem 8.	18
Fig. 11.	Intact cold-leg flow 42 cm from vessel center -- Standard Problem 8. - - - - -	18
Fig. 12.	Pressurizer pressure for Standard Problem 8. - - -	19
Fig. 13.	Pressure in broken hot leg for Standard Problem 8.	19
Fig. 14.	Pressure drop across simulated pump in broken hot leg -- Standard Problem 8. - - - - -	20
Fig. 15.	Hot-leg break flow 1 057 cm from vessel center (pump side) -- Standard Problem 8. - - - - -	20
Fig. 16.	Cold-leg break flow 238 cm from vessel center (vessel side) -- Standard Problem 8. - - - - -	20
Fig. 17.	Low power rod cladding temperatures for Standard Problem 8. - - - - -	21
Fig. 18.	High power rod temperatures for Standard Problem 8.	21
Fig. 19.	TRAC noding diagram for Semiscale Test S-02-6. - -	23
Fig. 20.	TRAC vessel noding for Semiscale Test S-02-6. - - -	24
Fig. 21.	Axial power distribution for Standard Problem 6. -	24

FIGURES (cont)

Fig. 22.	Core heater temperature for high power rod (Semiscale Test S-02-6). - - - - -	24
Fig. 23.	Core heater temperature for low power rod (Semiscale Test S-02-6). - - - - -	24
Fig. 24.	Vessel pressure for Semiscale Test S-02-6. - - - - -	25
Fig. 25.	Break mass flow for Semiscale Test S-02-6 (experimental value calculated using FDB-23 and GB-23 VR). - - - - -	25
Fig. 26.	Break mass flow for Semiscale Test S-02-6 [experimental value calculated using FTB-21 (corrected) and GB-21VR]. - - - - -	26
Fig. 27.	Broken loop fluid density for Semiscale Test S-02-6. - - - - -	26
Fig. 28.	TRAC noding of Marviken vessel and pipe. - - - - -	28
Fig. 29.	TRAC noding of Marviken Test 4 nozzle. - - - - -	28
Fig. 30.	Marviken Test 4 mass flux. - - - - -	29
Fig. 31.	Marviken Test 4 pressure near top of vessel. - - - - -	29
Fig. 32.	Marviken Test 4 temperature 20.5 m above vessel bottom. - - - - -	29
Fig. 33.	Hot rod maximum cladding temperature for the 20 TRAC runs of Standard Problem 5. - - - - -	31
Fig. 34.	Summary statistics for hot rod maximum cladding temperature. - - - - -	31
Fig. 35.	W-test for normality of the hot rod maximum cladding temperature. - - - - -	31
Fig. 36.	Normal tolerance limits for hot rod maximum cladding temperature. - - - - -	31
Fig. 37.	Sensitivity functions for hot rod maximum cladding temperature. - - - - -	32
Fig. 38.	PWR vessel noding. - - - - -	35
Fig. 39.	PWR base case cladding temperatures. - - - - -	36

FIGURES (cont)

Fig. 40.	PWR lower plenum liquid fraction. - - - - -	36
Fig. 41.	PWR lower plenum pressures. - - - - -	36
Fig. 42.	Fraction of injection water that bypasses the lower plenum -- PWR study. - - - - -	37
Fig. 43.	PWR unwrapped downcomer velocities at 18.2 s. - -	37
Fig. 44.	PWR unwrapped downcomer velocities at 27.9 s. - -	38
Fig. 45.	PWR unwrapped downcomer velocities at 38.7 s. - -	38
Fig. 46.	Cladding temperatures for PWR 150% break case. -	39
Fig. 47.	PWR peak rod (13) cladding temperatures. - - - -	40
Fig. 48.	PWR cladding temperatures for complete dumping case. - - - - -	40
Fig. 49.	CCTF vessel water inventory. - - - - -	43
Fig. 50.	CCTF lower plenum liquid temperature. - - - - -	43
Fig. 51.	CCTF lower plenum pressure. - - - - -	43
Fig. 52.	CCTF cladding temperature (Rod #10, Level 2). -	43
Fig. 53.	CCTF unwrapped downcomer velocity vectors at 3.6 s. - - - - -	44
Fig. 54.	CCTF unwrapped downcomer velocity vectors at 9.1 s. - - - - -	44
Fig. 55.	CCTR unwrapped downcomer velocity vectors at 14.1 s. - - - - -	45
Fig. 56.	CCTF unwrapped downcomer velocity vectors at 33.2 s. - - - - -	45
Fig. 57.	TRAC air-water vessel model. - - - - -	47
Fig. 58.	Vessel pressure for air-water test Y10. - - - - -	49
Fig. 59.	Hot-leg mixture velocity for air-water test Y10.	49
Fig. 60.	Calculated fallback collector water volume for air-water test Y02. - - - - -	50
Fig. 61.	Vapor fraction at gamma densitometer level (air-water test Y-06). - - - - -	51

FIGURES (cont)

Fig. 62.	Square root of gas vs liquid Kutateladze numbers for the density and water injection ratio tests. - - - - -	52
Fig. 63.	Geometry and water levels for the two proposed steam source vessels for the Japanese (A) and German (B) large-scale experiments. Dimensions are in meters. - - - - -	54
Fig. 64.	Calculated discharge flow rate and vessel pressure for vessel (A) using the SOLA-LOOP and K-FIX codes. - - - - -	55
Fig. 65.	Calculated discharge flow rate and vessel pressure for vessel (B) using the SOLA-LOOP and K-FIX codes. - - - - -	55
Fig. 66.	Marviken discharge pipe, test nozzle, and rupture disc assembly. - - - - -	56
Fig. 67.	Dimensions of the Marviken test nozzles. - - - - -	57
Fig. 68.	Mass flow rates for Marviken Test #1. - - - - -	58
Fig. 69.	Mass flow rates for Marviken Test #2. - - - - -	58
Fig. 70.	Mass flow rates for Marviken Test #4. - - - - -	59
Fig. 71.	Spray tip penetration comparison with experiment. - - - - -	63
Fig. 72.	Particle plots and velocity vectors in the staggered control rod configuration. - - - - -	63
Fig. 73.	Percentage of droplet mass flux de-entrainment in the staggered control rod configuration. - - -	64
Fig. 74.	Performance of PKL stereographic lens system. - -	67
Fig. 75.	Slab upper plenum simulation experiment. - - - - -	69
Fig. 76.	Droplet cross flow in slab upper plenum simulator (10 m/s and 3.8 kg/m). - - - - -	70
Fig. 77.	Scattergram of p_1^* and kinetic energy. - - - - -	79
Fig. 78.	Experimental apparatus. - - - - -	88
Fig. 79.	Water surface displacement vs time for D-006 (no structure) and D-004 (UCS and UIS). - - - - -	90

FIGURES (cont)

Fig. 80.	Schematic of upper core structure simulation experimental apparatus. - - - - -	95
Fig. 81.	Results of hodoscope scans across corners of a 127-pin assembly. - - - - -	96
Fig. 82.	Hodoscope sensitivity to a single-pin void as a function of the position of the void in test bundle. - - - - -	97
Fig. 83.	Single block impact test. - - - - -	100
Fig. 84.	Force-time history. - - - - -	101
Fig. 85.	Assemblage of plastic (model) blocks. - - - - -	102
Fig. 86.	Graphite model, graphite prototype, and plastic model blocks (right to left) for two-dimensional seismic tests. - - - - -	102
Fig. 87.	PCRV pressure and helium mass response for the FSV DBDA. - - - - -	106
Fig. 88.	Containment pressure response for the FSV DBDA. - -	106
Fig. 89.	Containment temperature response for the FSV DBDA.-	107
Fig. 90.	Containment helium mass fraction following the FSV DBDA. - - - - -	107
Fig. 91.	Containment pressure response to a FSV steam line break accident. - - - - -	108
Fig. 92.	Containment temperature response to a FSV steam line break accident. - - - - -	109
Fig. 93.	Containment molecular weight during a FSV steam line break accident. - - - - -	109
Fig. 94.	Steam generator outlet steam temperature response to a 100 K step increase in reheater inlet helium temperature. - - - - -	110
Fig. 95.	Reheater outlet steam temperature response to a 100 K step increase in reheater inlet helium temperature. - - - - -	110

FIGURES (cont)

Fig. 96. Alumina sleeve exposed by sloughing of SS cladding. - - - - - 117

Fig. 97. Photo shows steel accumulated above spacer grid #7. - - - - - 117

Fig. 98. Radiograph shows steel accumulated above spacer grids #6 and #7. - - - - - 118

Fig. 99. Guard heater cavity thermal model network. - - - - - 120

Fig. 100. Support frame. - - - - - 120

Fig. 101. Unwrapped side view of reactor cavity annulus nodes with insulation blockage locations indicated. - - - - - 126

Fig. 102. Insulation blockage locations indicated in unwrapped top view of nodes around the nozzles and piping penetration nodes. - - - - - 126

Fig. 103. Vertical cross section of the reactor vessel with nodalization and coordinate system indicated. - - - - - 127

Fig. 104. Abrupt flow area change geometries. - - - - - 129

Fig. 105. Curves for r , \hat{C} , and M_1 for $\gamma = 1.4$ and $A_0/A_1 = 1/4$ (M is Mach number). - - - - - 132

Fig. 106. Compressible expansion loss coefficient for $\gamma = 1.4$. - - - - - 132

TABLES

I.	Radiative Heat Transfer Nomenclature - - - - -	8
II.	TRAC Noding Study for FLECHT Test 3541 - - - - -	11
III.	Comparison of Calculated and Measured Initial Conditions for Standard Problem 8 - - - - -	16
IV.	Table of Events -- Standard Problem 8 - - - - -	17
V.	Noding and Running Times for Standard Problem 8 -	22
VI.	TRAC Computing Statistics for Test S-02-6 - - - -	27
VII.	Table of Events U.S. PWR Sensitivity Study -- Basecase - - - - -	39
VIII.	CCRT Initial Conditions - - - - -	42
IX.	Air-Water Test Flow Conditions - - - - -	48
X.	Fallback and Density Results for Air-Water Tests -	51
XI.	Summary of Results of 15 SIMMER-II Calculations -	76
XII.	Timing of Significant Events for TREAT Test R-7 -	85
XIII.	Analytical vs Experimental Results for the SRI International Bubble Expansion Experiments - - - -	90
XIV.	Summary of SIMMER-II Energetics Analysis - - - - -	92
XV.	Single Block Impact Predictions and Test Results -	101
XVI.	CHAP Modules - - - - -	105
XVII.	Spacer-Grid/Cladding Contact Configuration and Friction Formulas - - - - -	116
XVIII.	DMFT Support Frame Nominal Design - - - - -	119
XIX.	Insulation Blockage Location Description - - - - -	125
XX.	Maximum Values of Selected Pressures, Forces, and Moments Resulting from Insulation Blockage of Various Reactor Cavity Flow Areas - - - - -	128

ABSTRACT

Development of the TRAC LWR safety code continued during the last quarter, with the final program structure changes being completed for the TRAC-PLA version. Progress was also made in several TRAC model development areas including droplet field, one-dimensional two-fluid hydrodynamics, quench front, and BWR radiative heat transfer. In the code assessment (verification) area, work focused on the analysis of three experiments using coarse-mesh models to minimize running time and on a sensitivity analysis of a heated Semiscale blowdown test. Other TRAC applications included a sensitivity study to examine some of the effects of downcomer dynamics on calculated peak clad temperatures during a LOCA in a typical PWR. An initial TRAC calculation of the Japanese Cylindrical Core Test Facility (CCTF) and a series of TRAC calculations of the Idaho National Engineering Laboratory (INEL) air-water tests were performed. In the thermal-hydraulics research area, investigations were made into the dynamics of proposed steam sources for large-scale German and Japanese experiments. Improved phase-change models led to excellent predictions of critical two-phase flows in the large-scale Marviken blowdown tests. Also, a new computational method for treating droplet fields with a distribution of drop sizes was developed.

LMFBR safety studies included completion of a SIMMER-II sensitivity study of a voided core postdisassembly expansion problem. The SIMMER-II calculated results for maximum kinetic energy in 15 cases ranged from about 2.5-20 MJ as compared to an isentropic expansion calculation value of about 100 MJ. SIMMER-II was also used to analyze TREAT loss-of-flow test R-7, and, in general, the agreement between calculated and experimental results was encouraging. SIMMER verification analyses also included calculations of SRI International bubble expansion experiments, again with encouraging agreement between calculations and experimental data. A detailed scaling and preliminary feasibility study of a postdisassembly upper core structure simulation experiment was completed. In LMFBR safety test facilities work, hodoscope scanning of a 127-pin bundle in the PARKA critical facility was continued.

Structural investigations in the HTGR safety research area included completion of single impact tests of graphite and plastic model blocks. A major milestone was reached in completing all component modules for the CHAP-2 (Ft. St. Vrain) HTGP systems analysis program. CHAP-2 studies were made of depressurization accidents with air and steam ingress to the primary system and of feedwater transients.

In the GCFR core disruptive test program, postmortem examinations of the FLS-1 37-pin disruptive test indicated considerable molten cladding flow occurred in the experiment. Investigations were made into the cause of heater rod failure in this experiment.

Containment systems evaluation work included studies of the effects of blockages of reactor cavity flow areas assumed to be caused by pieces of insulation loosened during a LOCA. The MOD-2 version of the COMPARE code was prepared for release to the National Energy Software Center (formerly the Argonne Code Center).

NUCLEAR REACTOR SAFETY

Compiled by

James F. Jackson
and
Michael G. Stevenson

I. INTRODUCTION

(J. F. Jackson and M. G. Stevenson, Q-DO)

This quarterly report summarizes technical progress from a continuing nuclear reactor safety research program conducted at the Los Alamos Scientific Laboratory (LASL). This research effort concentrates on providing an accurate and detailed understanding of the response of nuclear reactor systems to a broad range of postulated accident conditions. Both analytical and experimental projects are included.

The report is mainly organized according to reactor type. Major sections deal with Light Water Reactors (LWRs), Liquid Metal Fast Breeder Reactors (LMFBRs), High-Temperature Gas-Cooled Reactors (HTGRs), and Gas-Cooled Fast Reactors (GCFRs).

The research discussed in this report was performed by a number of divisions and groups at LASL. The names and group affiliations of the individual staff members responsible for the work are given at the beginning of each section. Most of the work was performed in the Energy (Q) Division. Other divisions contributing to the program were the Theoretical (T) Division, Computer Science and Services (C) Division, the Systems, Analysis, and Assessment (S) Division, and the Dynamic Testing (M) Division.

Most of this research was funded by the Nuclear Regulatory Commission (NRC), with certain projects being funded by the Department of Energy (DOE).

508 050

II. LWR SAFETY RESEARCH

(J. F. Jackson, Q-DO)

Three of the major projects in LASL's light water reactor safety research program are reported in this section. The first is the development, testing against experimental data, and application of the Transient Reactor Analysis Code (TRAC). The second involves thermal-hydraulic research in key problem areas of importance to water reactor safety. The third is an experimental program that supports modeling development activities and investigates new instrumentation techniques for safety experiments.

A. TRAC Code Development and Verification

(J. C. Vigil and R. J. Pryor, Q-6)

TRAC is an advanced, best estimate computer program for the analysis of postulated accidents in LWRs. It features a nonhomogeneous, nonequilibrium, multidimensional fluid dynamics treatment; detailed heat transfer models; and a flow-regime-dependent constitutive equation package to describe the basic physical phenomena that occur under accident conditions. It can be used to calculate initial steady-state conditions and the major phases (blowdown, bypass, refill, and reflood) of a loss-of-coolant accident (LOCA) in a continuous and consistent manner.

The first version of TRAC, called TRAC-P1, is directed toward pressurized water reactor (PWR) LOCAs. An improved version, TRAC-PIA, will be released through the National Energy Software Center at the end of the calendar year. Later versions of the code will treat boiling water reactors (BWRs) and provide capabilities for Anticipated Transients Without Scram (ATWS) and Reactivity Insertion Accident (RIA) analyses.

In conjunction with the TRAC development effort and as part of a closely coupled code assessment effort, the code is being applied to a broad range of water-reactor safety experiments. These experiments are designed to study separate and integral effects that occur during all phases of a LOCA. TRAC posttest calculations are

compared with the experimental results to test the thermal-hydraulic models in the code. Pretest calculations to evaluate the predictive capability of TRAC are in progress and will receive increased emphasis in FY 1979.

During the quarter, a number of code improvements were made involving standardized input/output (I/O) capabilities, memory allocation, overlay structure, database arrangement, graphics postprocessor, and program maintenance. Progress was also made in several model development areas including droplet field, one-dimensional two-fluid hydrodynamics, quench front, and BWR radiative heat transfer. In the code assessment area, work was focused on the analysis of three experiments using coarse-mesh models to minimize running time and on a sensitivity analysis of a heated Semiscale blowdown test.

1. TRAC Code Development

(J. M. Sicilian, Q-6)

Program structure changes for TRAC-PLA were completed this quarter. These changes include a new binary I/O package, dynamic allocation at execution of both small core memory (SCM) and large core memory (LCM), a new overlay structure, and a consistent data structure for one-dimensional components. Significant progress was also made in the development of an improved graphics postprocessor and a new program maintenance controller.

a. Standardization of Input and Output Routines

(R. J. Pryor, Q-6)

The 14 TRAC subroutines, which handle binary I/O operations have been replaced by 4 subroutines. The new I/O routines are much simpler than their predecessors, and more importantly, all nonstandard I/O operations have been removed and replaced with standard binary read and write statements. This enhances the portability of the code since no conversion of the I/O routines should be required to install TRAC outside LASL. As a secondary benefit, the new I/O routines require less storage and execute faster than those they replaced.

b. Dynamic Memory Allocation

(J. M. Sicilian, Q-6)

TRAC has been modified to adjust automatically its LCM size to fit each problem during its execution and to use all available SCM at each point in the calculation. These changes provide greater flexibility in problem size, reduce the cost of running TRAC at LASL, and simplify modification of the program. Because they utilize system features of LTSS, these capabilities will be removed for release versions of TRAC, although the structure needed to reimplement them will remain.

c. Improvements to the Program Maintenance Code, HORSE

(R. P. Harper, Q-6)

A new version of HORSE has been developed which, together with modifications to the program source and binary files, will allow simultaneous work on several versions of TRAC (e.g., PWR version and BWR version). This version of HORSE has been tested and will be put into production on completion of TRAC-PIA.

d. Improved Overlay Structure

(J. M. Sicilian, Q-6)

A new overlay structure for TRAC has been implemented. This overlay structure modifies the hydrodynamic iteration section of TRAC, dividing this calculation into prepass, outer iteration, and postpass overlays rather than the previous division by component type. This modification reduces the expense of running TRAC on systems which cannot load overlays from LCM as is done at LASL.

e. Consistent Database for One-Dimensional Components

(J. M. Sicilian, Q-6)

The data array areas for one-dimensional components have been rearranged. This resulted in definition of consistent pointer tables for one-dimensional components. Because of this consistency, a great deal of redundant coding has been removed from the component subroutines.

f. Improved Graphics Postprocessor

(J. C. Ferguson, Q-6)

A new graphics postprocessor program, TRCPLOT, has been programmed and tested with prototypical data. This program will

replace the utility program GRIT that is currently being used. The new postprocessor is more flexible and efficient than its predecessor. Work to permit use of this postprocessor with TRAC-generated data is currently under way and should be completed during the next quarter.

2. Fluid Dynamics Methods

(D. R. Liles, Q-6)

Progress during the quarter centered on producing a working one-dimensional, two-fluid, hydrodynamics package along with a three-dimensional vessel module with droplet field for inclusion in the TRAC-P2 version. In addition, a significant effort was spent in debugging and testing TRAC-PIA prior to its anticipated December 1978 release.

a. One-Dimensional, Two-Fluid, Hydrodynamics

(J. H. Mahaffy, Q-6)

A version of TRAC is now running with the one-dimensional, semi-implicit, drift-flux package replaced by a two-fluid, hydrodynamics model. The replacement of the drift-flux equations with a two-fluid formulation provides a more natural representation of countercurrent vapor-liquid two-phase flow. It also facilitates the addition of extra field equations (for droplet modeling for example) should that prove desirable in future code versions.

The full two-fluid code is now being tested on a sequence of simple problems. The decision to include this one-dimensional, two-fluid capability in version P2 will be postponed until the result of timing studies and sample verification studies are complete.

b. Droplet Field

(D. R. Liles, Q-6)

It has been decided to retain a separate droplet density as well as energy equation in the additional three-dimensional field equations. The appropriate computer files to incorporate the droplet field into TRAC have been created and successfully compiled. Debugging of the droplet modification is in progress.

508 054

3. Heat Transfer Methods

(W. L. Kirchner, Q-6)

Effort during this quarter was focused on BWR fuel element heat transfer and improved quench front modeling. A basic, generalized set of modules to describe the complex BWR fuel element radiation heat transfer processes has been coded. Improvements have been made to the quench front modeling to ensure consistency between quench front positions and fuel rod thermal conditions, independent of nodding selection.

a. BWR Radiation Heat Transfer

(D. A. Mandell, Q-6)

Work was initiated on the radiative heat transfer model to be incorporated into the BWR version of the TRAC code. The model consists of radiative heat transfer to the vapor and to the droplets, as well as surface-to-surface radiative heat transfer between an arbitrary number of rod groups.

Radiative heat transfer within an absorbing, emitting, and scattering medium is governed by integrodifferential equations. These equations can be solved analytically only for very simple geometries and/or only for limiting conditions, such as an optically thin or optically thick gas.¹ Because numerical solutions of these equations are also formidable, a number of assumptions are made which represent a compromise between the exact solution and the need for a fast, convenient computer method. The following assumptions are made.

1. The N surfaces are gray and diffuse for both emission and reflection.
2. Each rod is one surface at a constant, known temperature (the temperature from the previous time step will be used).
3. At a given horizontal location, the water vapor and droplet temperatures have constant, but different, known values (temperatures from the previous time step will be used).
4. Scattering will be neglected.
5. The vapor and drops will be assumed to be optically thin (a gas is optically thin if the absorption

coefficient times a characteristic length is much less than one).

The basic equations for the net radiative heat flux from each surface to the other surfaces and to the two-phase mixture can be derived in a manner similar to the equations derived by Siegel and Howell.² The derivation given in Ref. 2 must be modified by using the intensity of radiation for a two-phase mixture obtained from the equation of transfer. This result is given by Deruaz and Petitpain.³

The following set of equations govern the radiative heat transfer phenomena, under the assumptions discussed above (nomenclature is defined in Table I).

$$\sum_{j=1}^N \left(\frac{\delta_{kj}}{\epsilon_j} - F_{kj} \frac{(1 - \epsilon_j)}{\epsilon_j} \bar{\tau}_{kj} \right) q_j = \sum_{j=1}^N \left[\left(\delta_{kj} - F_{kj} \bar{\tau}_{kj} \right) \sigma T_j^4 - F_{kj} \bar{\alpha}_{kj} e_b^{eq} \right] \quad (1)$$

where

$$e_b^{eq} = \frac{(1-\alpha) n_L^2 K^L \sigma T_L^4 + \alpha n_V^2 K^V \sigma T_V^4}{\pi [(1-\alpha) n_L^2 K^L + \alpha n_V^2 K^V]}$$

$$\bar{\alpha}_{kj} = K^{eq} L_{kj}$$

$$\bar{\tau}_{kj} = 1 \text{ for optically thin conditions,}$$

$$K^{eq} = \frac{(1-\alpha) n_L^2 K^L + \alpha n_V^2 K^V}{(1-\alpha) n_L^2 + \alpha n_V^2}$$

$$K^L = \pi N_d R^2, \text{ and}$$

$$K^V = K_p(T)$$

TABLE I
RADIATIVE HEAT TRANSFER NOMENCLATURE

e_b^{eq}	equivalent black-body emissive power
F_{kj}	view factor of surface j as seen from surface k
L_{kj}	geometrical mean beam length from surface k to surface j
n_L	real part of liquid index of refraction
n_V	real part of vapor index of refraction
N	total number of surfaces
N_d	droplet number density
q_j	net heat flux leaving surface j
R	droplet radius
T_j	temperature of surface j
T_L	liquid temperature
T_V	vapor temperature
ϵ	void fraction
$\bar{\tau}_{ij}$	absorptivity from surface j to surface i
$\bar{\tau}_{ji}$	transmissivity from surface j to surface i
τ_{kj}	= 0 if $k \neq j$ = 1 if $k = j$
ϵ_j	emissivity of surface j
σ	Stefan-Boltzmann constant
K^L	liquid absorption coefficient
K^V	vapor absorption coefficient
K_p	Planck mean absorption coefficient

In order to determine the appropriate number of rod groups to be used in the TRAC code, and to evaluate the assumptions made in the radiative heat transfer model, the above equations are being

coded separately. This code will be used to verify the proposed radiative heat transfer model. The code is modular so that future model improvements can be easily made and its incorporation into TRAC accomplished in a straightforward manner.

b. Quench Front Modeling

(W. L. Kirchner and R. J. Pryor, Q-6)

Several important model improvements were incorporated into the reflood package of the TRAC code during this quarter. In particular, the quench front location was forced to be consistent with the radial conduction fuel rod temperature calculation. This was achieved by relating the quench front position to a reference temperature and the critical heat flux (CHF) clad temperature:

$$\Delta z_{QF} = 1 - \frac{T_i - T_{CHF}}{T_R - T_{CHF}} \Delta z_i , \quad (2)$$

where

Δz_{QF} = quench front position within a mesh cell,

Δz_i = axial length of mesh cell,

T_i = clad surface temperature,

T_{CHF} = critical heat flux clad temperature, and

T_R = reference temperature.

The CHF clad temperature is identical to that used in the heat transfer coefficient selection. This ensures consistency within the code as the quench front enters and leaves a mesh cell. The reference temperature is the clad temperature at the time the quench front enters a mesh cell. This choice is made so that movement of the quench front is not accelerated as the average clad temperature falls. The net result of this methodology is direct coupling between quench front propagation and fuel rod stored energy effects. The actual quench front velocity is calculated as before by the Dua and Tien model,⁴ but this value is now used only in assessing

the heat transfer rate. The heat transfer coefficient used in the quench front correlation is from Yu,⁵ which includes subcooling effects.

Figure 1 illustrates the agreement achieved between the improved code prediction and FLECHT forced flooding Test 3541 (the TRAC-P1 prediction is also shown for comparison⁵). The new method also is an improvement over the old in that the sensitivity to noding selection has been significantly reduced. This is also evident in the smoothness of the quench front envelope as compared to the release version (TRAC-P1) prediction in Fig. 1.

Several sensitivity studies were completed to investigate the effects of heat transfer and hydrodynamic mesh spacing on the predictions. Table II lists the key results for FLECHT Test 3541 with several noding selections that would reasonably cover the range of TRAC applications. This FLECHT test was in a 12-ft heated bundle at a high flooding rate and a high subcooling. Because an interpolation method is applied to initialize the fine-mesh temperature field, the initial conditions (axial temperature profile), for reasonable mesh sizes (less than a meter), are slightly

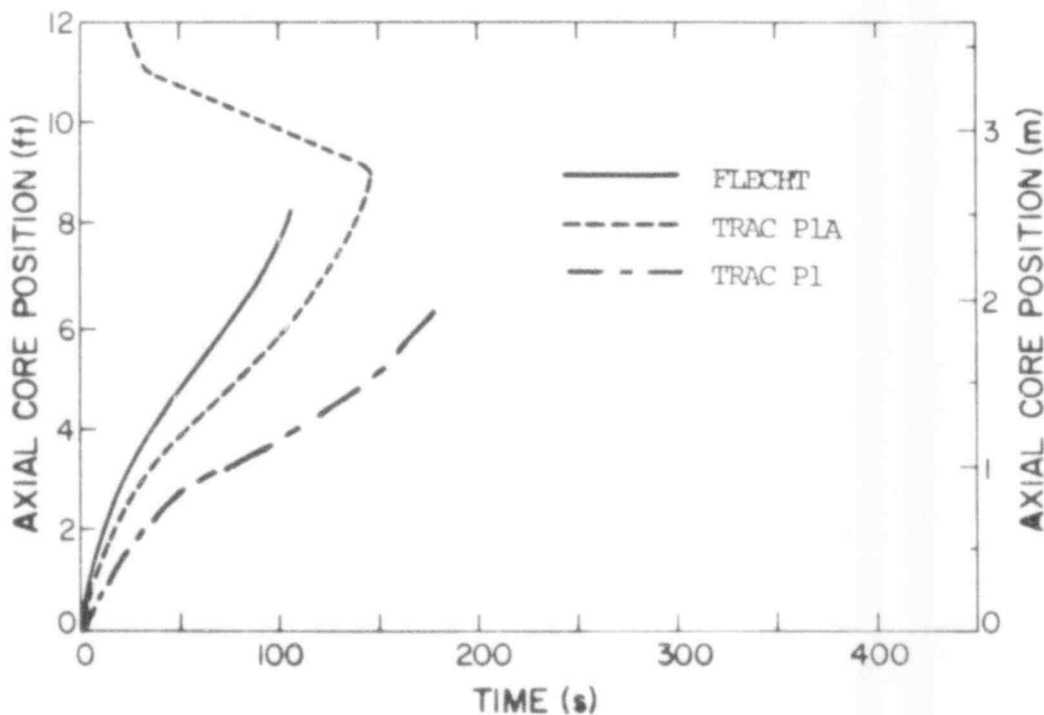


Fig. 1. Quench front position history for FLECHT Test No. 3541.

TABLE II
TRAC NODING STUDY FOR FLECHT TEST 3541

	Hydro Levels In Core	Radial Conduction Levels In Core	Peak Clad Temperature (K)	Time to Peak Clad Temperature (s)	Time to Quench At Core Midplane (s)
Base case	9	45	1 162	7.7	103
Coarse-mesh hydro	5	25	1 173	6.0	117
Fine-mesh hydro	20	100	1 170	11.1	93
Fine-mesh conduction	9	90	1 158	7.3	99

sensitive to the noding (these differences converge as the noding is refined). This accounts for some of the discrepancies, particularly in peak cladding temperatures. Also, for noding selections that are less than a one-to-one correspondence to the FLECHT stepped axial power profile, the averaging of the power shape results in additional discrepancies. The variation in results as a function of the hydrodynamic mesh cell length is due mainly to the axial void fraction profile used in the heat transfer coefficient calculation in the post-CHF regimes. The conclusion drawn from this exercise is that in the range of nodings expected for TRAC applications, the reflood methodology is not a strong function of noding size.

4. TRAC Code Assessment

(K. A. Williams, Q-6)

The assessment effort this quarter concentrated on evaluating the ability of TRAC to calculate experiments using coarser noding than was initially intended. In particular, the three-dimensional vessel noding was reduced by a factor of about five, while the one-dimensional noding was reduced by a factor of two from that previously used for assessment problems. The motivation for this coarse noding was to decrease running times as part of an exercise to evaluate the feasibility of developing faster versions of TRAC. The nodings used in these calculations were initial judgmental choices, and are likely to be far from optimum.

The results for three problems including Marviken Test 4 (a full-scale critical flow test), Standard Problem 6 (Semiscale Test S-02-6, a heated small-break experiment), and Standard Problem 8 (Semiscale Test S-06-3, a full-break LOCA through reflood) are reported in this section. Comparisons between experimental data and TRAC calculations for a wide variety of system variables show relatively good agreement; however, it appears that some additional model development will be needed for use in a fast-running "coarse-mesh" version of TRAC.

The effect of modeling and database changes made during this quarter were evaluated by recalculating most problems from the "standard" verification set to be included with the TRAC-PIA manual. The results of these calculations indicate that the current code is giving improved results in areas where modeling changes were made, e.g., reflood heat transfer.

Work was begun to provide a pretest prediction of the first loss-of-fluid test (LOFT) nuclear test L2-2 and for a test from the Semiscale MOD-3 facility. In preparation for these pretest predictions, posttest analyses are in progress for LOFT isothermal test L1-5 and Semiscale MOD-3 test S-07-1.

a. TRAC Calculations of U.S. Standard Problem 8

(J. R. Ireland and P. B. Bleiweis, Q-6)

Steady state and transient calculations of Semiscale Test S-06-3 (U.S. Standard Problem 8) were performed as part of an NRC-requested computer code competition. This test was a full 200% break LOCA from blowdown through reflood. As in the other competition problems, the objective was to demonstrate the ability to obtain reasonable results at reduced computer running times.

Figure 2 shows a TRAC schematic of the Semiscale system which was modeled by 15 TRAC components and 15 junctions. The vessel noding is shown in Fig. 3 and the axial power distribution is shown in Fig. 4. Three axial core levels were used to model the axial power shape. Since two azimuthal segments and one radial ring were used in the core region, two average powered rods along with a high powered and a low powered rod were used for heat transfer

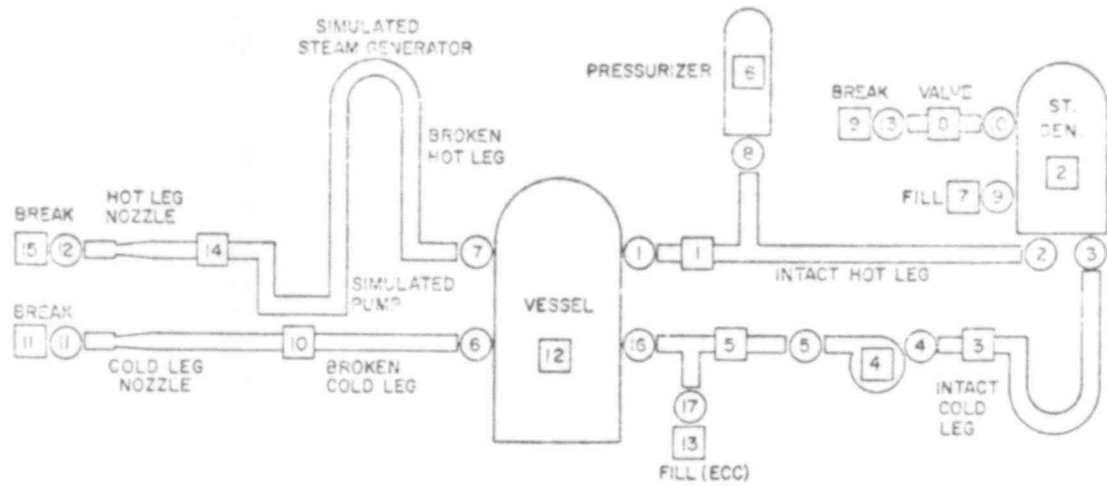


Fig. 2. TRAC component schematic for Standard Problem 8 (Test S-06-3).

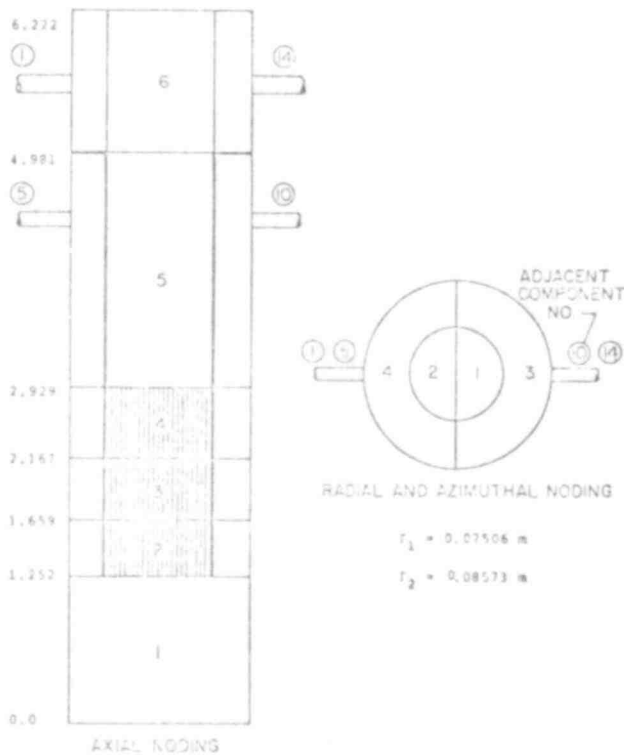


Fig. 3. TRAC vessel noding for Standard Problem 8.

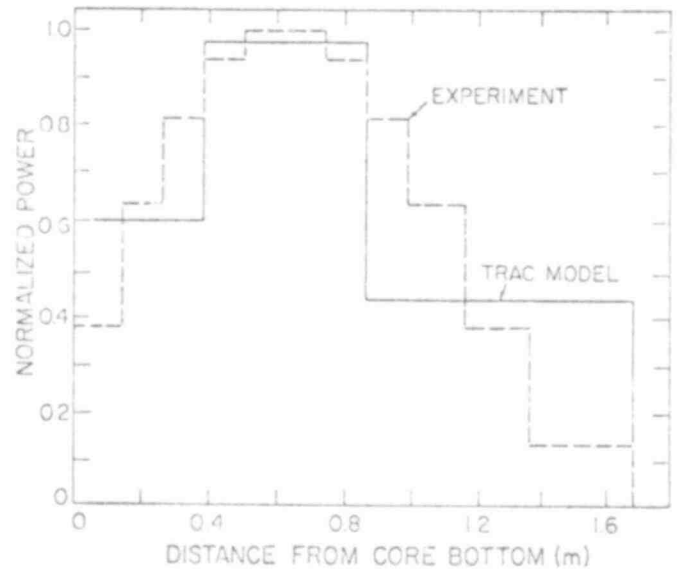


Fig. 4. Axial power distribution for Standard Problem 8.

and peak clad temperature calculations. A total of 112 TRAC cells (24 cells in the vessel) were used to model the Semiscale system. As mentioned above, the nodding was reduced from that normally employed for developmental assessment calculations. The emergency core cooling system (ECCS) flows were modeled with a fill component by lumping the measured accumulator low-pressure injection system (LPIS) and high-pressure injection system (HPIS) volumetric flows to obtain an effective ECCS velocity vs time. This curve is shown in Fig. 5. The break nozzle nodding for both the broken cold leg and broken hot leg are shown in Fig. 6, and the simulated containment suppression tank back pressure, modeled as a break component in TRAC, is shown in Fig. 7. This pressure boundary condition was used on both the broken hot leg and the broken cold leg.

The steady-state option in TRAC was used to generate initial conditions prior to transient initiation. These calculated

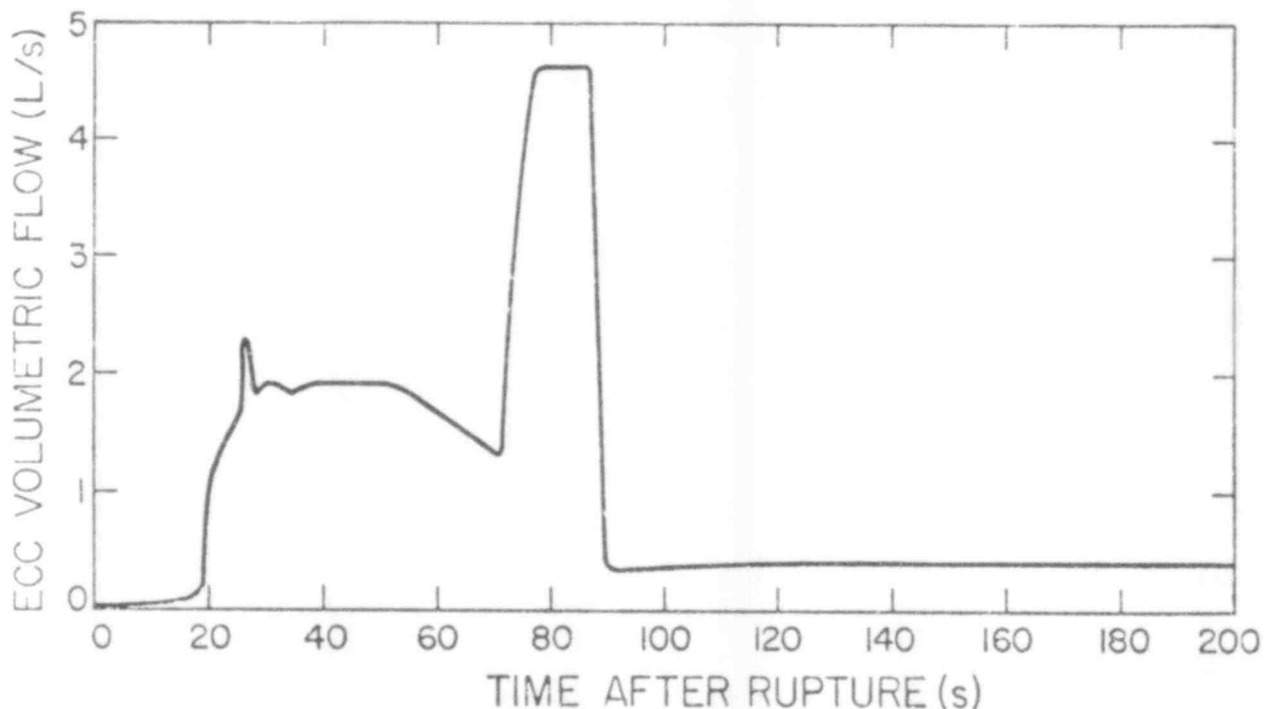
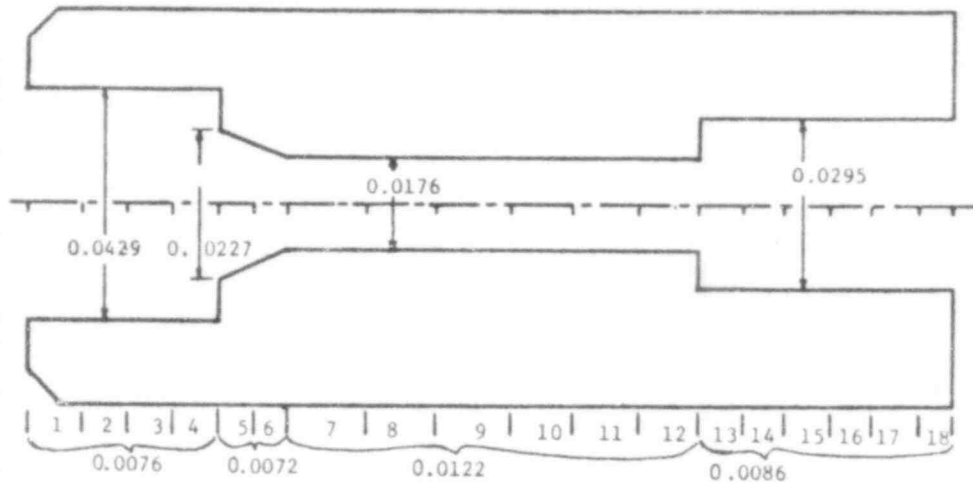


Fig. 5. Combined ECC volumetric flow rate (LPIS, HPIS, and accumulator) for Standard Problem 8.



Total Length = 0.169 4 m = 6.67 in.

Fig. 6. S-06-3 Semiscale LOFT counterpart nozzle.

conditions are compared with measured data in Table III. As can be seen, the agreement is very good. Table IV summarizes important events that occurred during the transient calculation. The calculation was stopped at 250 s after the high power rod quenched through the core midplane.

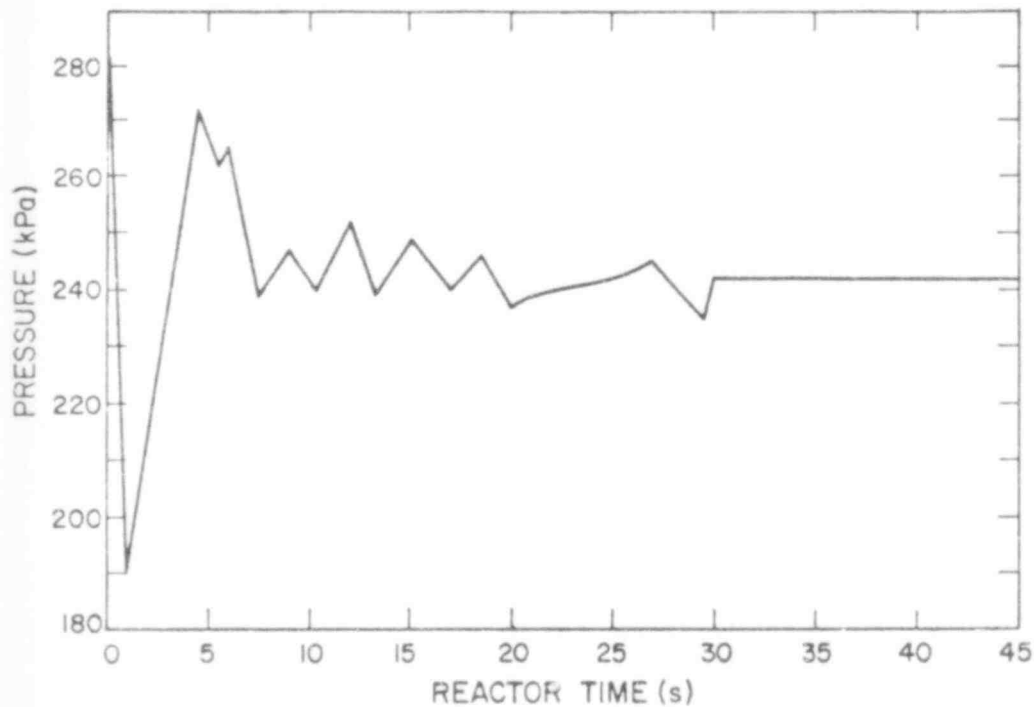


Fig. 7. Suppression tank pressure for Standard Problem 8.

TABLE III
COMPARISON OF CALCULATED AND MEASURED INITIAL CONDITIONS
FOR STANDARD PROBLEM 8

<u>Parameter</u>	<u>Calculated</u>	<u>Measured</u>
1. Initial power (75% of full power)	(input)	1.0058×10^6 W
2. Pump speed (~ constant)	(input)	170.0 rad/s
3. Power decay	(input)	Time-dependent
4. High power rod linear power	(input)	39.4 kW/m
5. Low power rod linear power	(input)	24.9 kW/m
6. Intact cold-leg flow rate	4.76	4.75 (kg/s)
7. Core volumetric flow rate	0.00734	0.00704 (m ³ /s)
8. Upper plenum pressure	1.58×10^7	1.577×10^7 Pa
9. Inlet fluid temperature to vessel	562.1	564.2 K
10. Outlet fluid temperature from vessel	601.4	599.8 K
11. Steam generator secondary side average fluid temperature	555.1	557.9 K
12. Steam generator secondary side average pressure	6.6×10^6	6.57×10^6 Pa
13. Steam generator secondary flow rate	0.57	0.41 (kg/s)
14. High power rod cladding temperature at midcore	694.4	690.0 K
15. Low power rod cladding temperature at midcore	669.1	672.0 K
16. ECC water temperature	(input)	510 K ($t \leq 20$ s 301 K $t > 20$ s

A comparison of the calculated and experimental upper plenum pressure is shown in Fig. 8 for the first 40 s of the transient. This comparison shows that TRAC slightly underpredicts the pressure for most of the blowdown; however, the agreement is still quite good. The difference can be attributed to the coarse nodding

TABLE IV
TABLE OF EVENTS -- STANDARD PROBLEM 8

<u>Event</u>	<u>Time (s)</u>
1. 200% double-ended cold-leg break, reactor power tripped	0.0
2. Begin HPIS flow	0.5
3. Begin isolating steam generator secondary side	8.0
4. Pressurizer empties (level below 0.1 m)	15.0
5. Accumulator flow initiated	18.5
6. High power rod first peak clad temperature reached (1 120 K)	20.0
7. Steam generator secondary side inlet valve closed	22.0
8. Begin LPIS flow, steam generator secondary side outlet valve closed	25.0
9. High power rod second peak clad temperature reached (1 124 K)	51.0
10. Bottom node of high power rod quenched	69.0
11. Accumulator flow ends	90.0
12. Low power rod quenches (through core midplane)	130.0
13. High power rod quenches (through core midplane)	240.0

in the core and the rough approximation that was made to obtain the axial power shape (Fig. 4). These effects cause the power in the central high power region to be lower than the actual case, resulting in a lower vessel pressure.

Comparisons of the intact loop pump inlet density and cold-leg density are shown in Figs. 9 and 10. Both comparisons show good agreement between the calculated and experimental values over most of the transient. However, as can be seen from Fig. 10, the calculated intact loop cold-leg density begins to show some oscillations after 20 s. The reason for this is that the ECC system is modeled with a short pipe connected to a fill in TRAC, whereas in the real

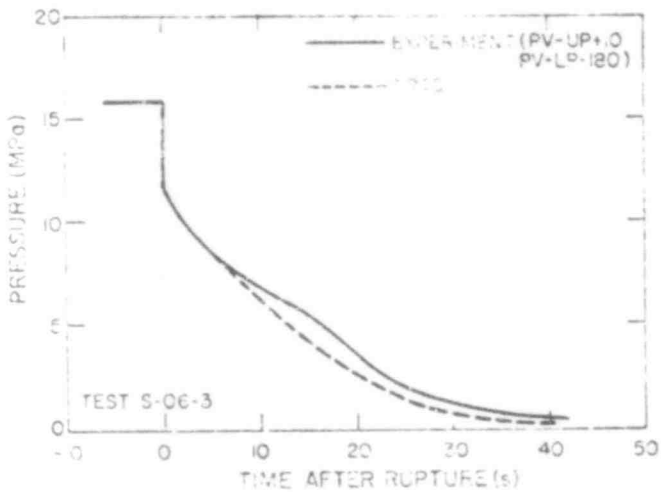


Fig. 8. Upper plenum pressure for Standard Problem 8.

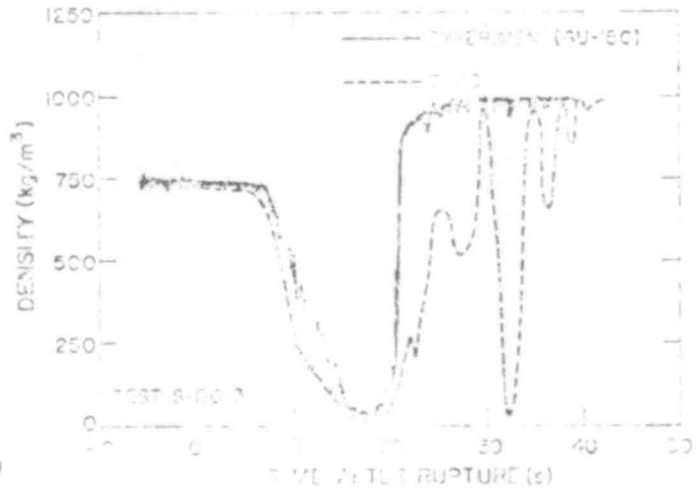


Fig. 10. Intact loop cold-leg density -- Standard Problem 8.

system, a complicated piping network connects the accumulator, LPIS and HPIS to the intact cold leg, which in effect creates a time delay before the cold ECC water reaches the cold leg. It should be noted that these oscillations are actually seen in the experiment farther out in time. Figure 11 shows a comparison of the calculated and measured flow in the intact cold leg. Note that even though

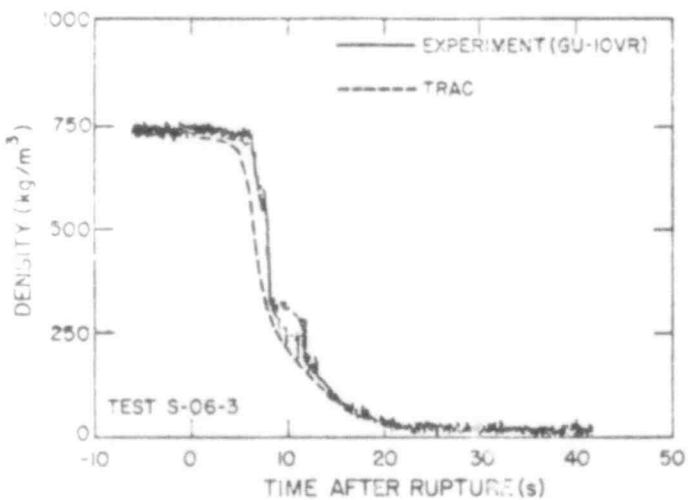


Fig. 9. Pump inlet density -- Standard Problem 8.

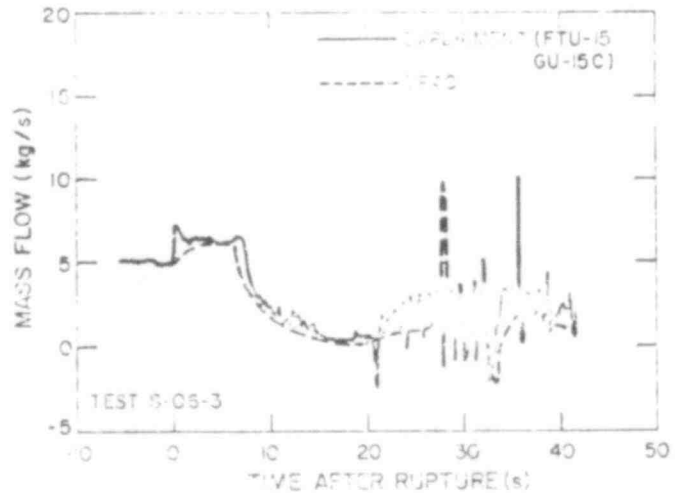


Fig. 11. Intact cold-leg flow 42 cm from vessel center -- Standard Problem 8.

the intact cold-leg density calculation shows some oscillations (Fig. 10), the calculated flow is in excellent agreement with the experimental data (Fig. 11).

Comparisons of the pressurizer pressure and broken hot-leg pressure are shown in Figs. 12 and 13. Calculated values for those variables are generally in good agreement with the reported data. The underprediction of the pressure can be explained by Fig. 14, which shows the pressure drop across the simulated pump in the broken hot leg. Most of the pressure drop in the system occurs in this component. It is seen that the calculated pressure drop is somewhat lower than the data, which results in a lower system pressure. This result coupled with the coarse noding in the core may explain why the TRAC calculation blows down at a faster rate compared to the experiment.

The calculated and experimental break flows are shown in Figs. 15 and 16. It is seen that the calculated hot-leg break flow is in good agreement with the experimental data whereas the calculated cold-leg break flow underpredicts the subcooled blowdown portion

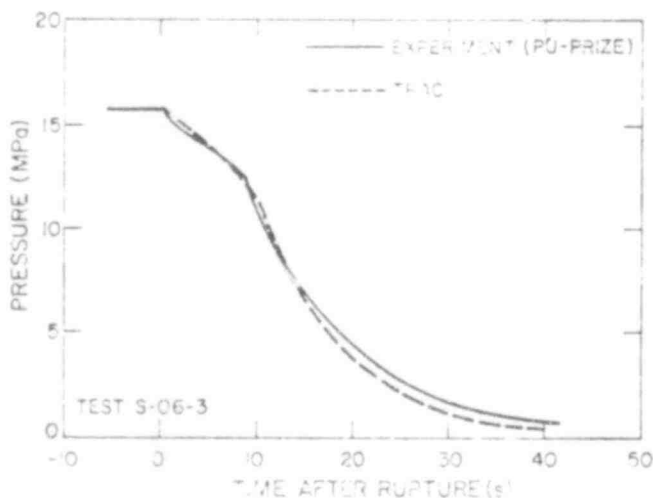


Fig. 12. Pressurizer pressure for Standard Problem 8.

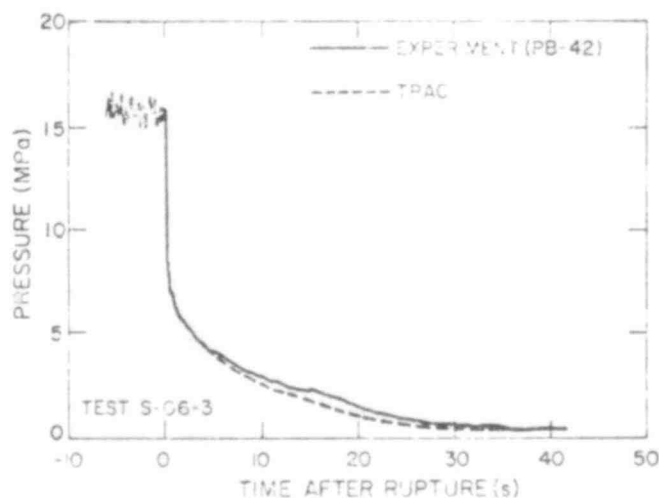


Fig. 13. Pressure in broken hot leg for Standard Problem 8.

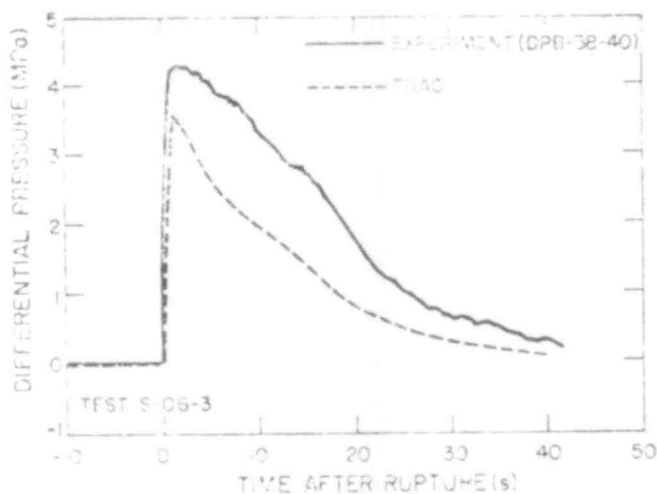


Fig. 14. Pressure drop across simulated pump in broken hot leg -- Standard Problem 8.

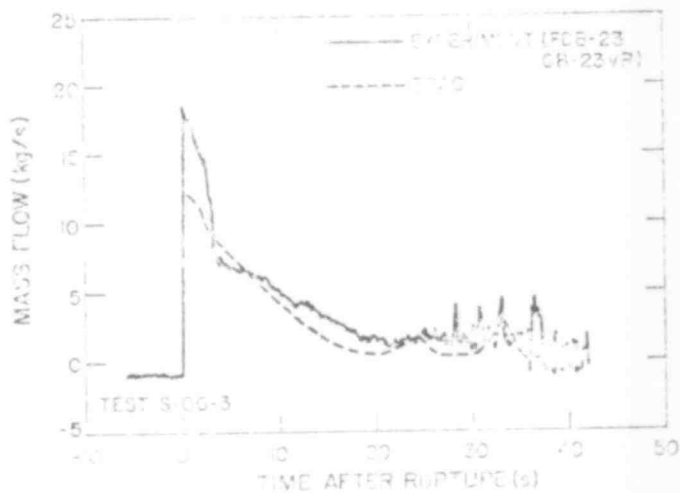


Fig. 16. Cold-leg break flow 238 cm from vessel center (vessel side) -- Standard Problem 8.

of the curve. This is due to boiling in the nozzle, which decreases the flow. This discrepancy is being investigated further.

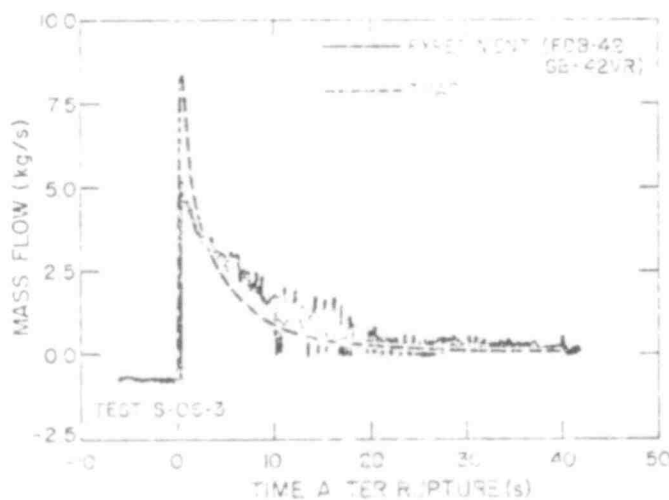


Fig. 15. Hot-leg break flow 1057 cm from vessel center (pump side) -- Standard Problem 8.

Comparisons for the low power and high power rod cladding temperatures are shown in Figs. 17 and 18. These comparisons are for the middle core level (core midplane) at about the 0.74 m (29-in.) elevation. The peak clad temperature occurs during blowdown for both rods and the calculated magnitudes and times of each peak are in good agreement with the reported data. The low power rods quench about 20 s too early in the calculation while the high power rods quench about 70 s too late. The high power rods quench too late because of the large change in the

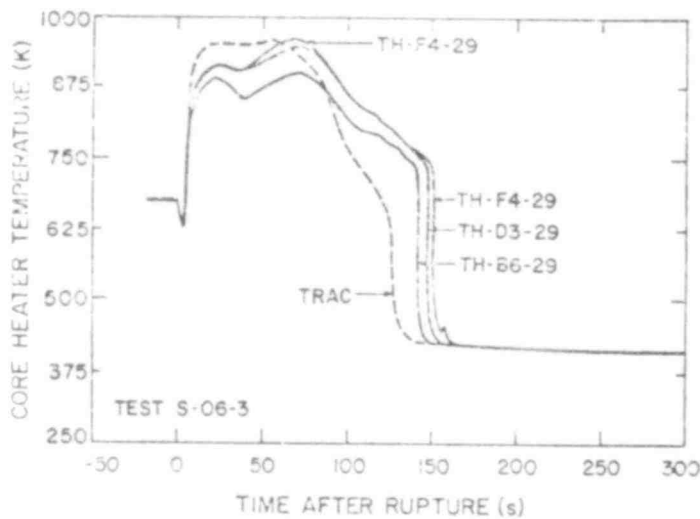


Fig. 17. Low power rod cladding temperatures for Standard Problem 8.

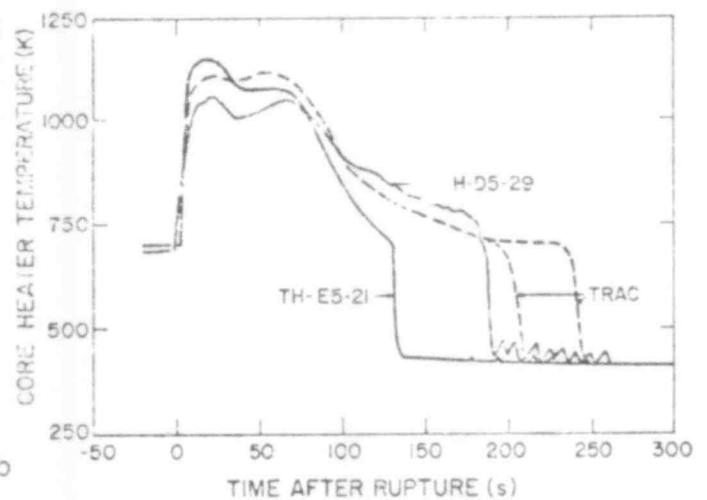


Fig. 18. High power rod temperatures for Standard Problem 8.

power step between core level 1 and core level 2 (see Figs. 3 and 4). If more axial nodes were to be used in the core, resulting in a smoother transition between power steps, the quench front would propagate faster and thus quench the rod earlier.

Table V summarizes the timing statistics for the calculation. A total Central Processor Unit (CPU) time of about 170 min was required for the 250 s transient using a total of 112 mesh cells (24 in the vessel).

In conclusion, the results for this TRAC calculation of U.S. Standard Problem 8 are generally in good agreement with the measured data. This indicates that the coarse vessel noding is adequate for relatively fast scoping calculations. A more detailed vessel noding would improve the agreement between the calculation and the experiment at the expense of increased running times.

b. TRAC Calculation of Standard Problem 6

(K. A. Williams, Q-6)

Semiscale Test S-02-6 (Standard Problem 6) was a single-ended, cold-leg pipe break experiment using 37 active heater rods having a tested power of 1.56 MW.⁷ The radial power profile was peaked with the four center heater rods having a peak axial power

TABLE V
 NODING AND RUNNING TIMES FOR STANDARD PROBLEM 8

<u>Fluid Mesh Cells</u>	
3-D Vessel	24
Nozzle	13
Pressurizer	3
Steam Generator	15
All other one-dimensional components	<u>52</u>
Total	112

<u>Reactor Time (s)</u>	<u>Running Time</u>	<u>CPU Time (min.)</u>
10		11.5
20		18.2
30		24.5
40		38.0
50		49.4
60		61.2
70		75.3
80		94.2
90		104.2
100		108.1
110		112.4
120		116.3
150		135.4
200		151.8
250		169.3

generation rate of 46.75 kW/m as compared to 37.86 kW/m for the remaining powered rods. This test is a small break experiment having a break area of 6% of the total pipe area.

This calculation was part of the NRC code competition set and running time was a primary consideration. Therefore, the problem noding was substantially reduced from that normally used for Semiscale assessment problems. For example, the TRAC model for Standard Problem 5 (heated Semiscale blowdown) used 10 axial levels in the core region with a total of 128 fluid cells in the vessel; the coarse model for Standard Problem 6 has only 3 axial levels in the core with a total of 24 cells in the vessel (Figs. 19 and 20).

Coarse noding of the core region results in the axial power steps in the heater rods not being resolved (Fig. 21) and thus cladding temperatures will not be predicted as well as they were

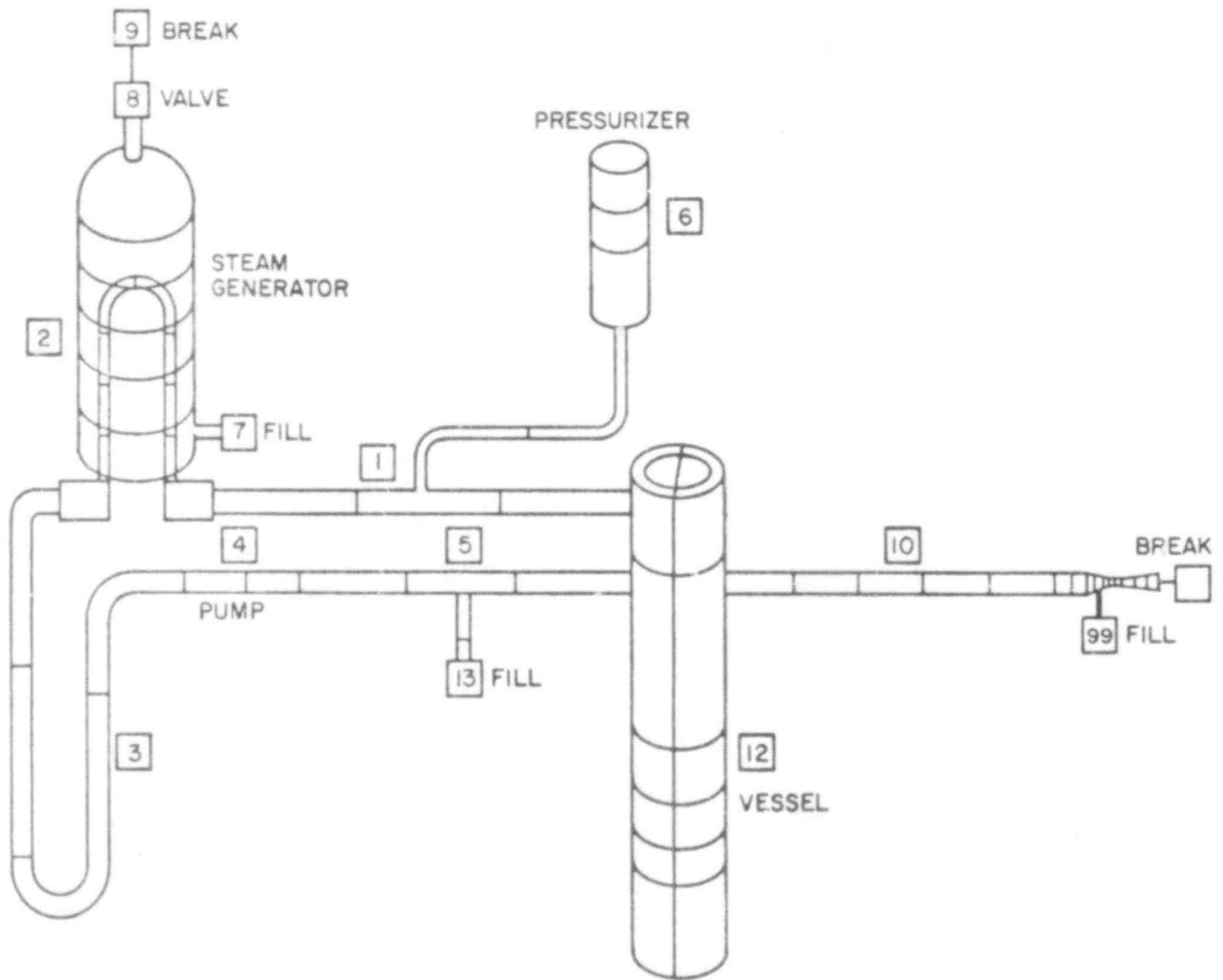


Fig. 19. TRAC noding diagram for Semiscale Test S-02-6.

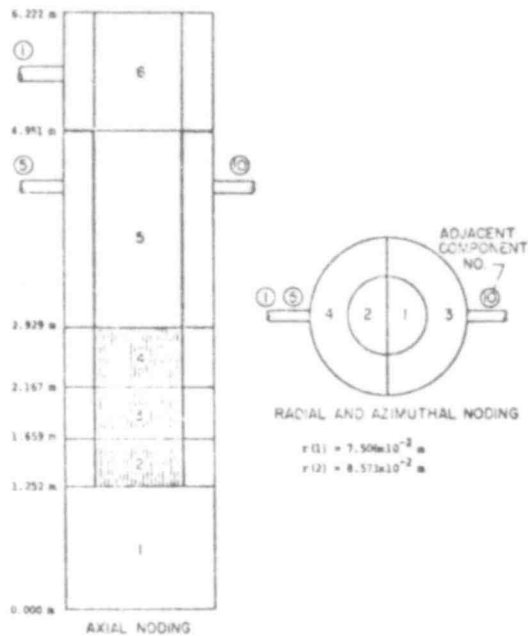


Fig. 20. TRAC vessel noding for Semiscale Test S-02-6.

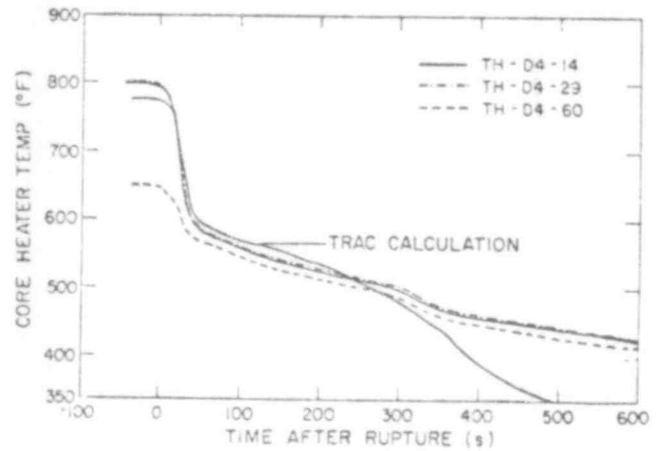


Fig. 22. Core heater temperature for high power rod (Semiscale Test S-02-6).

for Standard Problem 5.⁸ However, the highest power level (core level 2) is closely approximated and should provide the best cladding temperature predictions. Figures 22 and 23 show the experimental data and TRAC calculations for high and low power rods, respectively, at the

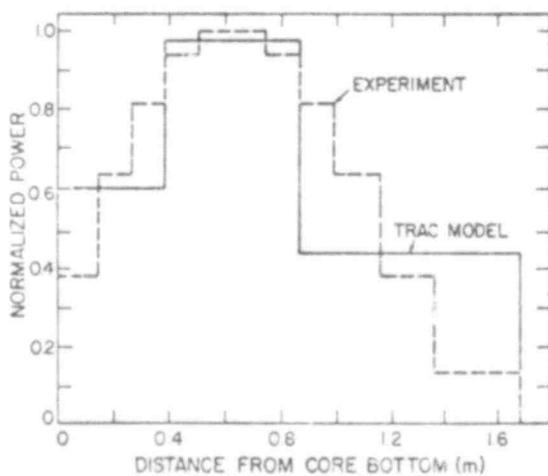


Fig. 21. Axial power distribution for Standard Problem 6.

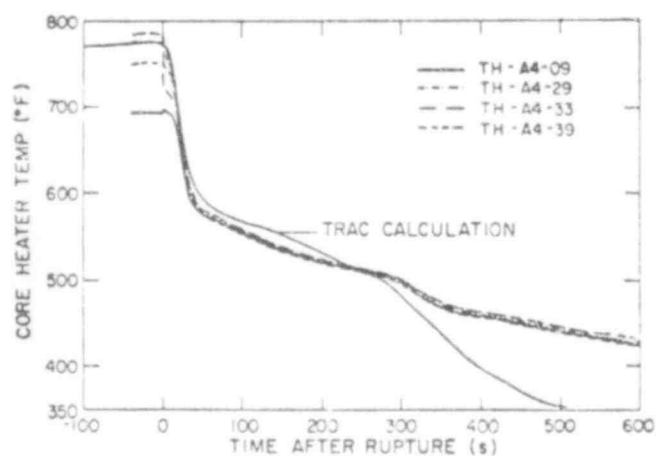


Fig. 23. Core heater temperature for low power rod (Semiscale Test S-02-6).

core peak power location. For this small break experiment, the rods do not go into departure from nucleate boiling (DNB), but rather cool down monotonically. The TRAC calculations are in excellent agreement for both the high and low power rods for the calculated steady state and give relatively good agreement during the first 30 s when the rod temperatures drop by about 200 K. This agreement continues for the first five minutes into the blowdown, after which the calculated cladding temperatures drop faster than actually occurred in the experiment. A comparison between pressures in the reactor vessel (Fig. 24) reveals the same effect. This relationship between pressure and rod temperatures is to be expected since the rod surface temperatures follow saturation during this period.

The cause of the discrepancy after 300 s can be attributed to an inaccurate prediction of discharge mass flow rate after this time. This is seen from the comparison of break flows in Figs. 25 and 26. The TRAC curve is the same in both figures; the difference is in the instrumentation used to obtain the experimental mass flow. Experimental results in Fig. 25 were obtained by combining a drag disk (FDB-23) momentum flux measurement with a gamma beam (GB-23 VR) density measurement; those in Fig. 26 used a turbine meter (FTB-21) volumetric flow measurement with another gamma beam (GB-21 VR) density measurement. These figures show a sudden reduction in the experimental break flow occurring at roughly 60 s. Until this time,

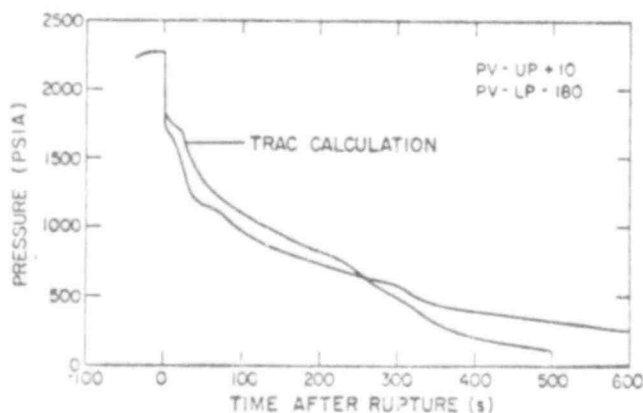


Fig. 24. Vessel pressure for Semiscale Test S-02-6.

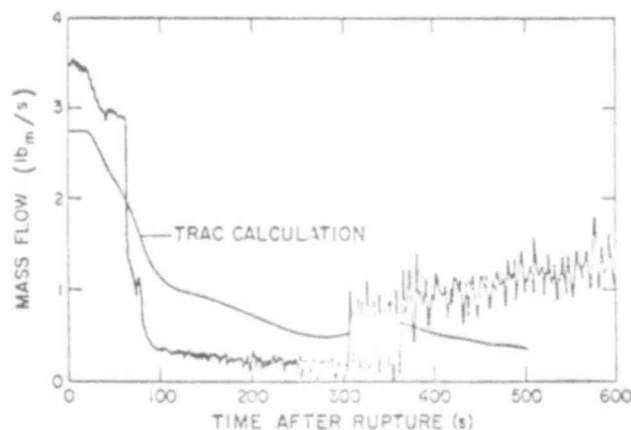


Fig. 25. Break mass flow for Semiscale Test S-02-6 (experimental value calculated using FDB-23 and GB-23 VR).

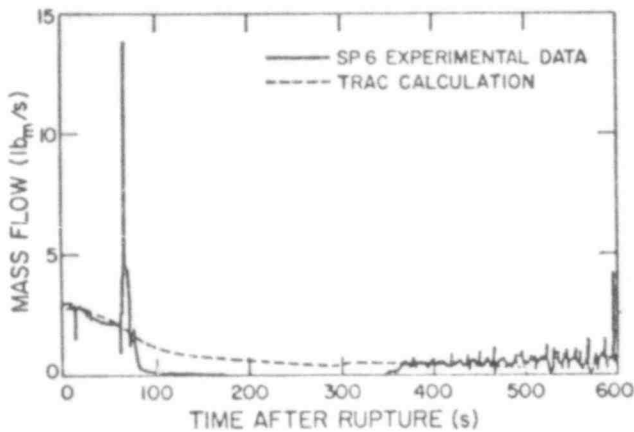


Fig. 26. Break mass flow for Semiscale Test S-02-6 [experimental value calculated using FTB-21 (corrected) and GB-21 VR].

the TRAC calculation is in agreement with the data of Fig. 26 which is reported⁷ to be most accurate at early times. The cause for this sudden reduction in mass flow appears to be as follows. For this small break experiment the water level in the downcomer is probably receding, as in a draining tank. At roughly 60 s, the water level has fallen low enough to "uncover" the broken cold leg resulting in a low density mixture being discharged. This effect is clearly shown in Fig. 27.

The reason TRAC does not predict this "uncovering" and sudden reduction in mass flow is two-fold. The first reason is the use of coarse noding; Fig. 20 shows that the mesh cell connected to the broken leg extends for 180° azimuthally and is approximately 2 m below the cold-leg elevation. Since the mixture density entering the broken leg is being donor-celled from this large fluid cell, this results in a much larger density and consequently an overprediction

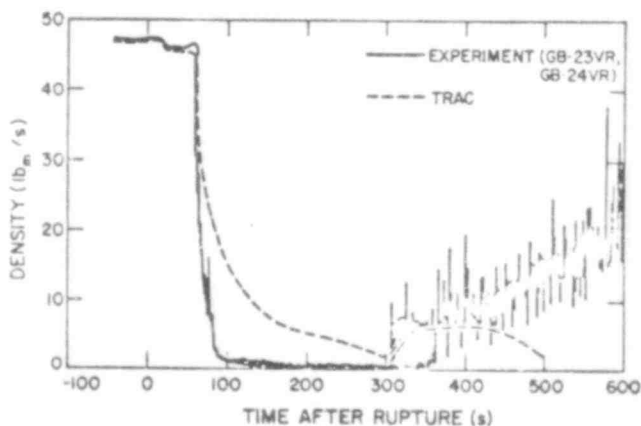


Fig. 27. Broken loop fluid density for Semiscale Test S-02-6.

of the mass flow. The second reason is that the calculated mixture in the downcomer does not collapse completely, which would allow a higher quality mixture to exit the vessel. Resolution of this problem, which is accentuated by the use of a coarse noding, will require further model development.

The computer statistics for this calculation are given in Table VI. Use of coarse noding significantly reduces the running

TABLE VI
TRAC COMPUTING STATISTICS FOR TEST S-02-6

Fluid Mesh Cells

One-dimensional cells:	Semi-implicit	36
	Fully-implicit	15
Three-dimensional cells:	Semi-implicit	24
Total fluid cells:		75

Computing Requirements

<u>Real Time (s)</u>	<u>CPU Time (min.)</u>
50	12.7
100	25.2
200	39.6
300	53.9
400	68.9
500	85.3

Average Time Step:	16×10^{-3} s
Average Computing Cost:	2.2×10^{-3} s/time-step/mesh cell

times for problems of this type and warrants the model development effort that is required to improve the accuracy of the calculated results.

c. TRAC Calculation of Marviken Full-Scale Critical Flow Test 4

(G. J. E. Willcutt, Jr. and R. J. Pryor, Q-6)

Marviken critical flow tests examine the blowdown of a large pressure vessel. The blowdown occurs through a pipe and nozzle with the entrance to the pipe protruding into the bottom of the vessel.⁹ The vessel maximum diameter is over 5 m, and the height from the vessel top to the nozzle exit is about 32 m. Test 4 used a nozzle with a 0.590-m minimum diameter. Measured initial conditions are a 5 MPa pressure at the top of the vessel and a rather complicated temperature profile. The temperature profile includes saturated steam at 535.5 K in the top 7 m, saturated water for the

508 070

next 7 m, and a series of ramps and plateaus in water temperature down to 497 K at the bottom of the vessel and 474 K at the nozzle inlet.

TRAC noding for the vessel and pipe is shown in Fig. 28 while the detailed noding used in the nozzle is shown in Fig. 29. Because this experiment can be modeled with the one-dimensional TRAC capability, fast running times were expected and therefore no special effort was made to reduce the number of mesh cells below that normally used in developmental assessment calculations. A semi-implicit pipe with 15 fluid cells was used to model the vessel maximum diameter section and top, and a fully implicit pipe with 45 fluid cells was used to model the lower curved part of the vessel, the pipe, and the nozzle. A zero velocity fill component supplied

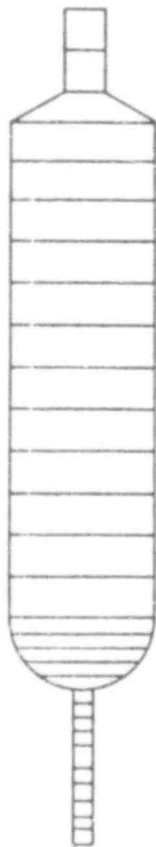


Fig. 28. TRAC noding of Marviken vessel and pipe.

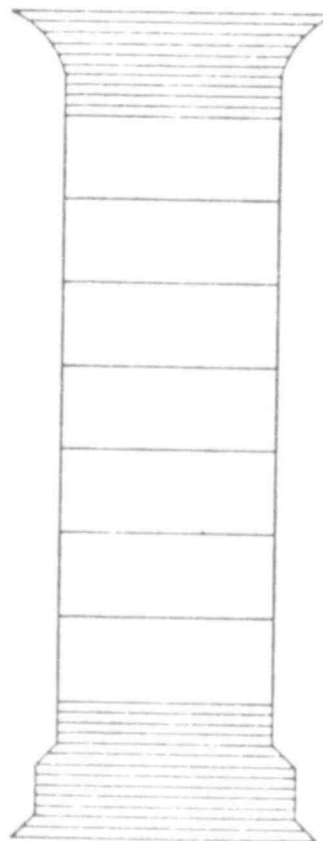


Fig. 29. TRAC noding of Marviken Test 4 nozzle.

boundary conditions at the upper end of the vessel and a fixed pressure break component was used at the nozzle exit.

Nozzle mass flux calculations are compared with the measured results in Fig. 30. TRAC results agree very closely with the initial peak, somewhat underpredict the subcooled part of the blowdown, and agree well with the saturated part of the blowdown (20-45 s). Near the end of the blowdown, the TRAC results are between the two measurements. TRAC pressure and temperature results near the top of the vessel (Figs. 31 and 32) agree very well with the data for the entire transient except for a short period during the first 3 s. During this early period, the data show a dip due to delayed nucleation in the deionized water which is not modeled in TRAC.

The TRAC annular slip model for pipes did not include any

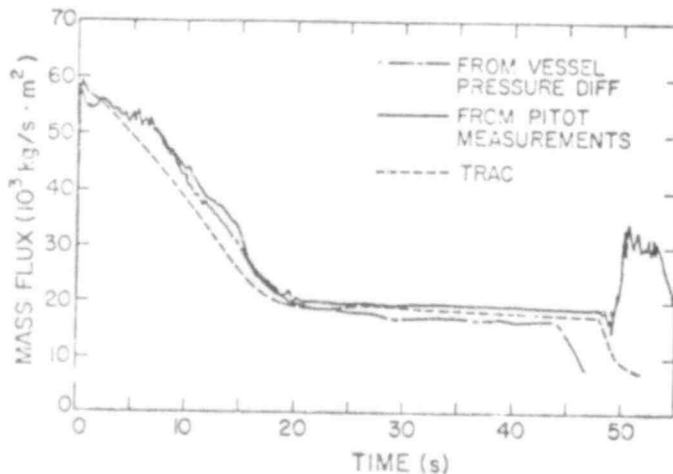


Fig. 30. Marviken Test 4 mass flux.

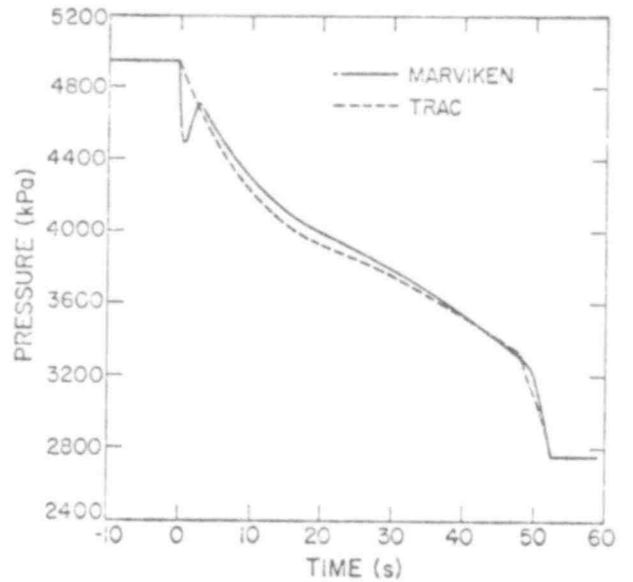


Fig. 31. Marviken Test 4 pressure near top of vessel.

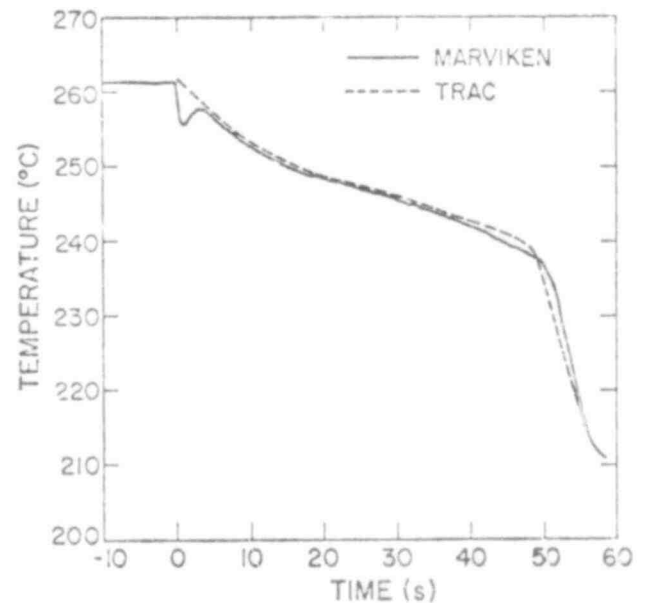


Fig. 32. Marviken Test 4 temperature 20.5 m above vessel bottom.

gravitational effects for vertical pipes so a term was added to provide gravitational separation for two-phase mixtures. Before this term was added, the vessel dome pressure dropped off about 5 s too early at the end of the transient. With this term, the pressure agrees very well with the data near the end of the transient.

This transient ran very fast using only 2.1 s of CDC-7600 CPU time for each second of transient time.

5. TRAC Sensitivity Analysis

(M. D. McKay, S-1)

First-stage analyses of TRAC for Standard Problem 5 (a heated Semiscale blowdown test) were made using Latin hypercube sampling¹⁰ (LHS) to select values of 10 input parameters. Uniform probability distributions were used for the parameter variations. The parameters varied were associated with the TRAC modeling of single-phase pipe friction, orifice pressure losses, net flashing rate between liquid and vapor, slip between liquid and vapor phases, and heat transfer correlations. The calculated output variables considered in this study included pressures, mass flow rates, volumetric flow rates, differential pressures, densities, liquid masses, and heater rod cladding temperature. Results for the hot rod maximum cladding temperature (HRMCT) will be discussed below.

Figure 33 contains the 20 plots of HRMCT and Fig. 34 contains summary statistics of the runs. Run number 8 (labeled 2 in Section 6-10 of Fig. 33) seemed to grow at an unusually high rate after 15 s, and was eliminated from analyses after that time (an error in the restart dump would explain this behavior and this possibility is being explored further). The runs that were not continued for 25 s are kept at their last value in Fig. 33 for plotting purposes. These runs, together with the times after which they were eliminated from analyses, are given in Fig. 34.

The probable range of variation of each output was estimated using tolerance limits. A tolerance limit is an interval derived from data which, with a certain confidence (say, 95%), covers a specified fraction (say, 90%) of the distribution of a random variable. Tolerance limits can be constructed without distributional assumptions using order statistics.¹¹ In addition, when normality is assumed, K-factors¹² can be used. For HRMCT, the

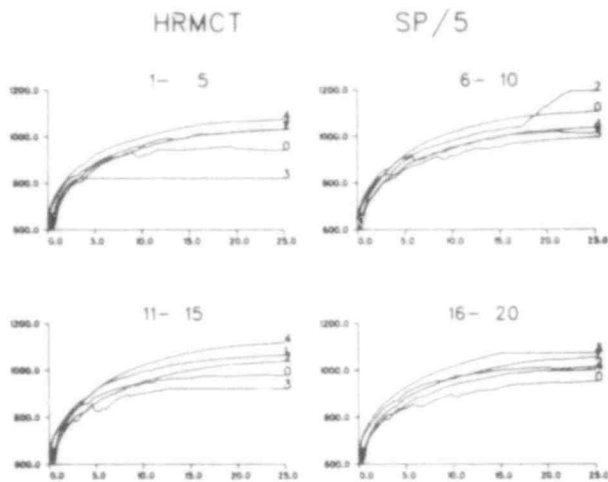


Fig. 33. Hot rod maximum cladding temperature for the 20 TRAC runs of Standard Problem 5.

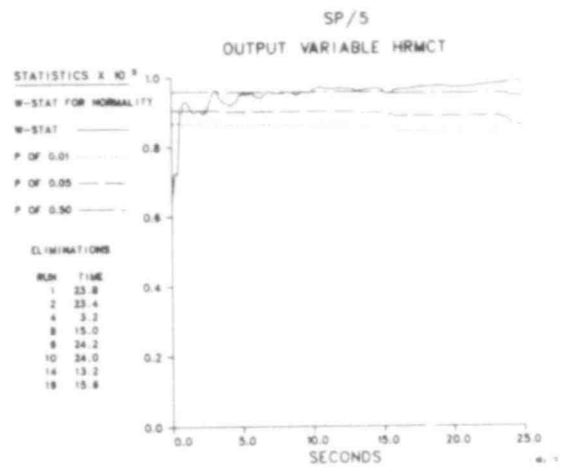


Fig. 35. W-test for normality of the hot rod maximum cladding temperature.

nonparametric and the normal tolerance limits were almost the same at 75% coverage. Figure 35 shows the value of the W-test¹³ for normality at each time point. The large values indicate no reason to question the normality assumption. The first, fifth, and fiftieth percentiles of W are also given in Fig. 35. Figure 36

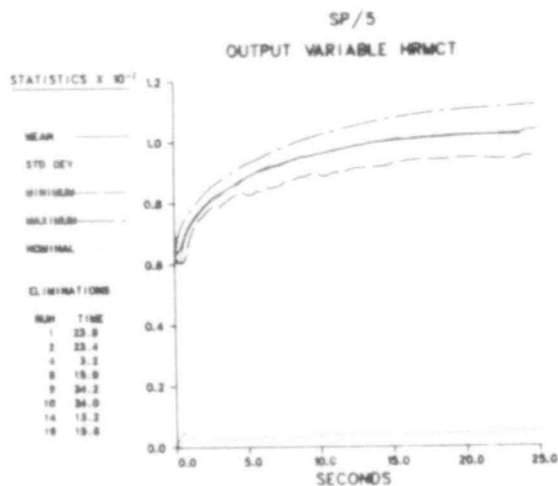


Fig. 34. Summary statistics for hot rod maximum cladding temperature.

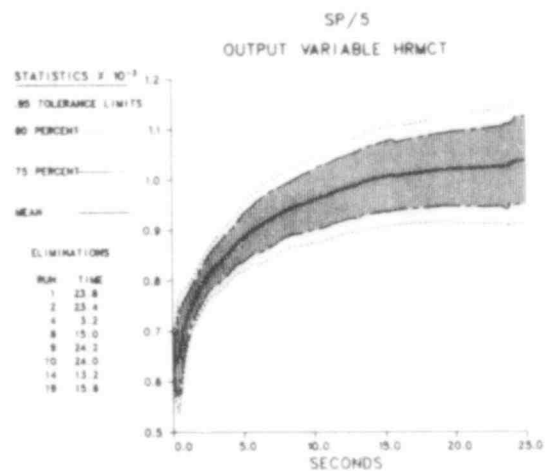


Fig. 36. Normal tolerance limits for hot rod maximum cladding temperature.

shows the 95% confident tolerance limits for both 75% and 90% coverages. We are 95% confident that values of the inputs chosen according to their independent uniform distributions will produce output values within the tolerance limits at least 90% (75%) of the time.

The relative importance of each input was determined by

1. selecting candidate subsets of the inputs using a stepwise partial correlation technique,¹⁴ and
2. calculating the relative importance of the inputs within the candidate subsets.

The candidate subsets were created independently at each time point and then filtered over time to produce the final candidate subsets. Partial correlations using the filtered candidate subsets only were used as sensitivity functions to measure relative importance. The final stage partial correlations are shown for the five selected inputs in Fig. 37. Input SHL (heat transfer coefficient between liquid phase and cladding/wall) dominates for the first 3 s and input SHV (heat transfer between vapor and cladding/wall) dominates for the remaining 22 s. When a variable

leaves the candidate subset, for example SSLIP at 12 s, its partial correlation goes to zero.

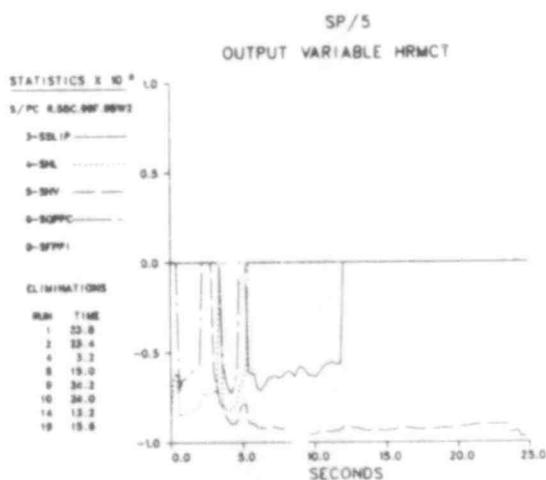


Fig. 37. Sensitivity functions for hot rod maximum cladding temperature.

B. TRAC Applications

(J. C. Vigil and P. B. Bleiweis, Q-6)

The work described in this section includes the application of TRAC to full-scale LWR transients and to the planned large-scale German and Japanese re-flood tests. These applications provide design assistance, pre-test predictions, and posttest

analyses for the experimental programs. In general, they are used to help with the planning, coordination, and analyses of the large-scale reflood experiments. TRAC applications to these experiments also help validate the code for use on full-scale LWR systems. Applications of TRAC to full-scale LWR systems provide best estimate predictions of the consequences of postulated transients. In addition to the above applications, TRAC is being used to analyze a variety of other tests and problems for outside users.

Part of the effort during the past quarter consisted of completing an NRC-requested TRAC sensitivity study to examine some of the effects of downcomer dynamics on calculated peak clad temperatures during a LOCA in a typical U.S. PWR. An initial TRAC calculation of the Japanese Cylindrical Core Reflood Test (JCCRT) was completed during the past quarter. Finally, a series of TRAC calculations of the Idaho National Engineering Laboratory (INEL) air-water tests were performed in support of the multinational reflood test program.

1. PWR ECCS Bypass Sensitivity Study

(P. B. Bleiweis, K. A. Williams, J. R. Ireland, D. Dobranich, D. R. Liles, and J. J. Pyun, Q-6)

The results of a series of TRAC sensitivity calculations performed at the request of the NRC are described in this section. The purpose of this study was to examine the sensitivity of LOCA-induced peak clad temperatures in a PWR to variations in ECC bypass behavior. In addition, a 150% double-ended guillotine break calculation was performed to determine the sensitivity of calculated peak clad temperatures to a variation in the break size.

This study was a follow-on to an earlier calculation of a complete LOCA sequence in a typical four-loop PWR.⁶ This earlier calculation used a peak linear power rating of 12 kW/ft. The results showed that the peak cladding temperature was 920 K and that this peak occurred during blowdown. The maximum temperature during reflood was 800 K. Nearly total bypass of the accumulator water was observed for the first 12 s of injection, resulting in about 40% of the accumulator flow being bypassed.

The calculations in this current study were based on the same basic PWR model, but with the linear power rating increased to about 15 kW/ft. This was done to simulate evaluation model conditions. In addition, several improvements were made to the basic model. The TRAC system model is identical to that used for the previous PWR LOCA calculation.⁶ However, the vessel noding (Fig. 38) was changed to include an extra axial level in the lower plenum below the downcomer to allow for radial vapor flow. Other major differences between the base case and the previous PWR calculation include the reduction of the lower plenum volume by about 10 m³ to account for the curvature of the vessel and structure in the lower plenum, more accurately calculated hydraulic diameters, a better modeling of the upper head flow areas, and a decrease in the effective wall thicknesses in the downcomer.

Three TRAC calculations were performed for this sensitivity study. The first, or base case calculation, was a 200% double-ended, cold-leg break LOCA performed from blowdown through refill and partially into reflood. This calculation was terminated when the rod midplane cladding temperatures during reflood had turned over. The second case was identical to the base case except that the break area was reduced from 200% to 150% (75% on each side of the broken cold leg). The third case was an attempt to change some of the models in TRAC to produce complete ECC delivery to the downcomer. In addition to these cases, separate ECC bypass calculations (similar to those performed⁸ for the CREARE experiments) were made for the PWR vessel model. Although not reported in detail here, these calculations provided some guidance on the range of modeling parameters required to go from complete ECC delivery to complete bypass. The results also indicated that the current modeling in TRAC is reasonable.

Figure 39 shows the base case midplane cladding temperatures calculated for the peak rod (rod 13) and for two rods in the inner (rod 5) and outer (rod 21) radial zones at the same azimuthal location as the peak rod (see Fig. 38 for rod locations). In addition, the cladding temperature time history of rod 21 at one axial level above the midplane is shown. All rods show double peaks during blowdown. Note that the second peak for rod 13 is slightly higher

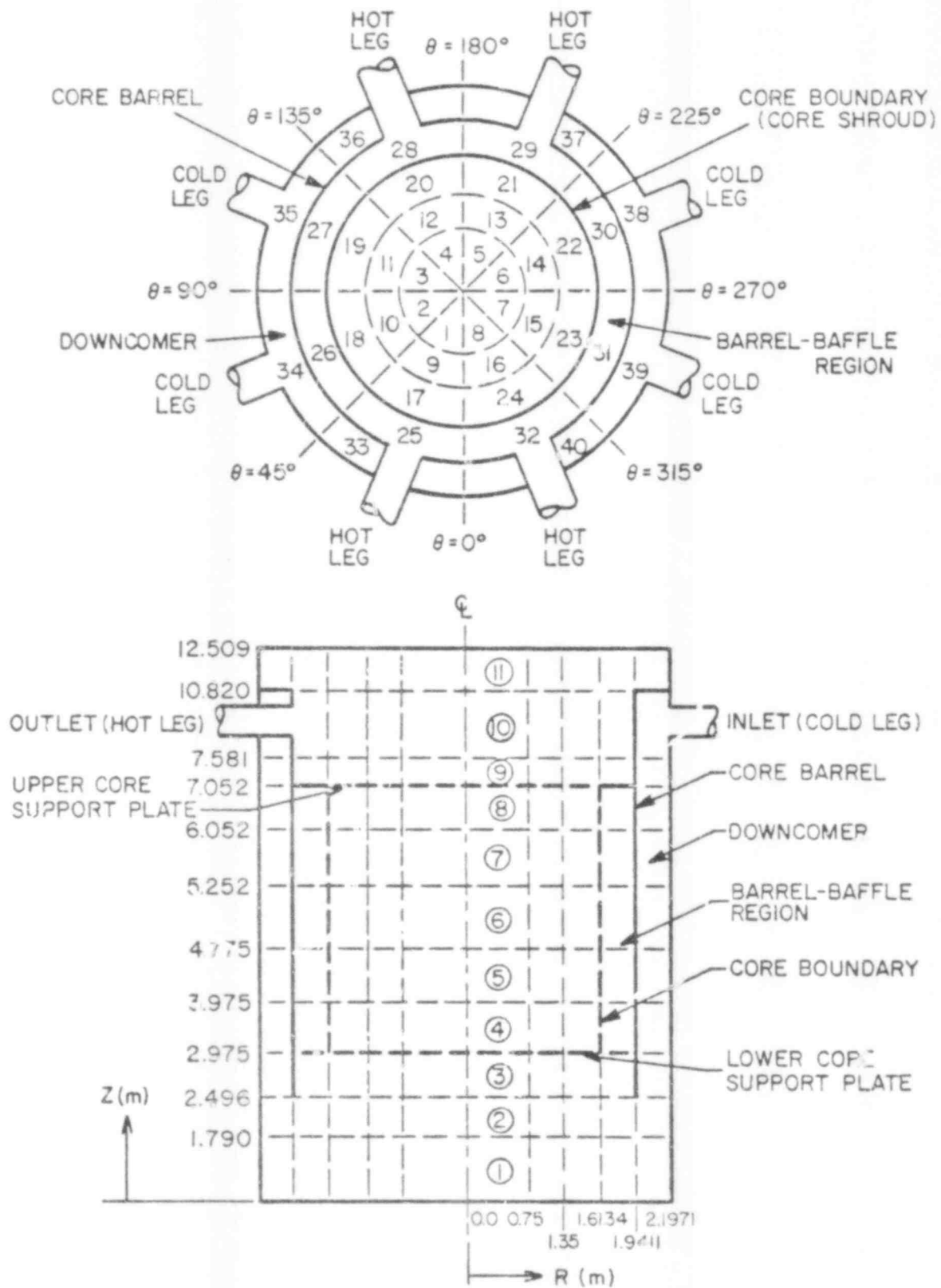


Fig. 38. PWR vessel noding.

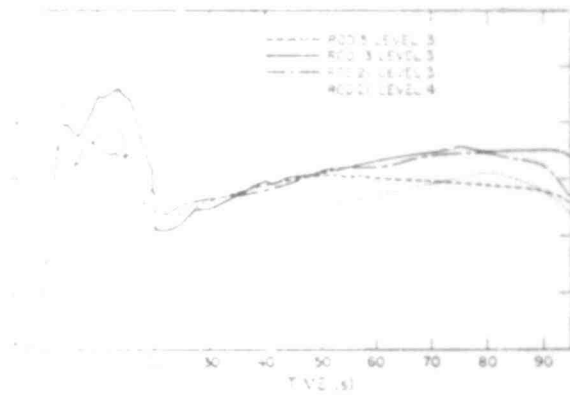


Fig. 39. PWR base case cladding temperatures.

However, as can be seen in Fig. 39, some rods (e.g., rod 21) peaked higher during reflood than during blowdown for axial positions above the midplane. This illustrates some of the multidimensional aspects of the thermal hydraulics calculated for the base case.

Figures 40 and 41 show the lower plenum liquid fractions and average lower plenum pressures for both the base and 150% break cases. Figure 42 shows the fraction of injected liquid (BPR) which bypasses the lower plenum for both cases. Almost total bypass occurs from about 11 s to about 36 s in the base case and is similar

than the first. After the second peak, the rods cooled substantially and then began a gradual rise until they peaked again during reflood. The calculation was terminated when all the rods had turned over after their reflood peaks, which was at about 95 s. The midplane temperature peaks were lower during reflood than during blowdown for most rods.

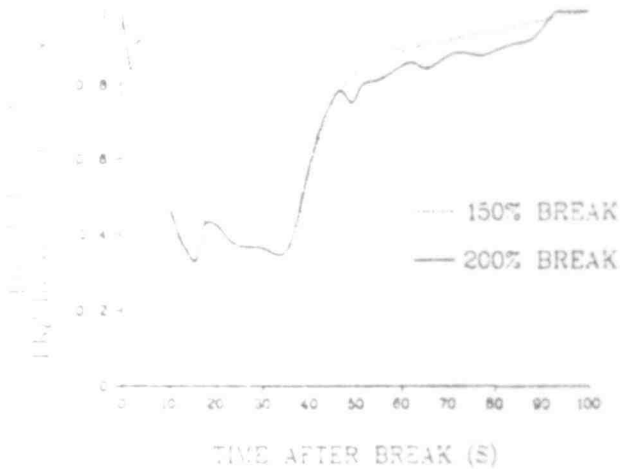


Fig. 40. PWR lower plenum liquid fraction.

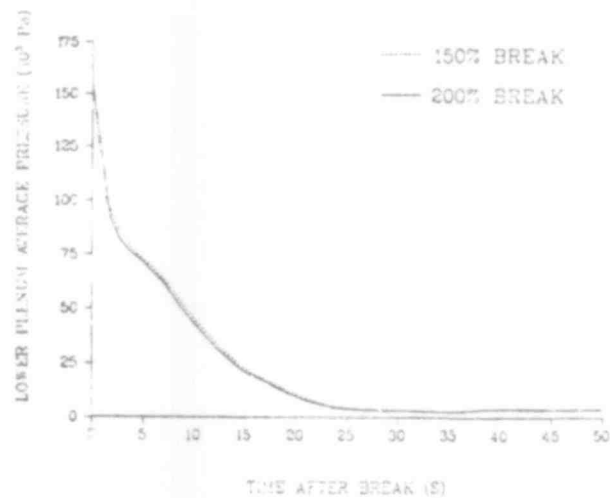


Fig. 41. PWR lower plenum pressures.

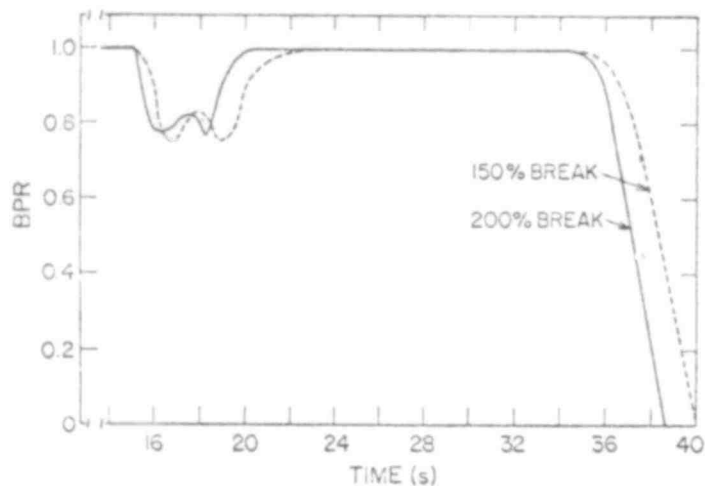


Fig. 42. Fraction of injection water that bypasses the lower plenum -- PWR study.

for the 150% break case. After this point the lower plenum fills rapidly with liquid. The accumulators empty at about 40 s and the remainder of the lower plenum filling is continued by the LPIS. Figures 43-45 show graphically unwrapped downcomer liquid and vapor velocities during this bypass period. The TRAC results show large vapor and liquid flows upward toward the break at the beginning of

bypass. As bypass continues and begins to decrease, countercurrent flow behavior is obtained as liquid begins to penetrate the

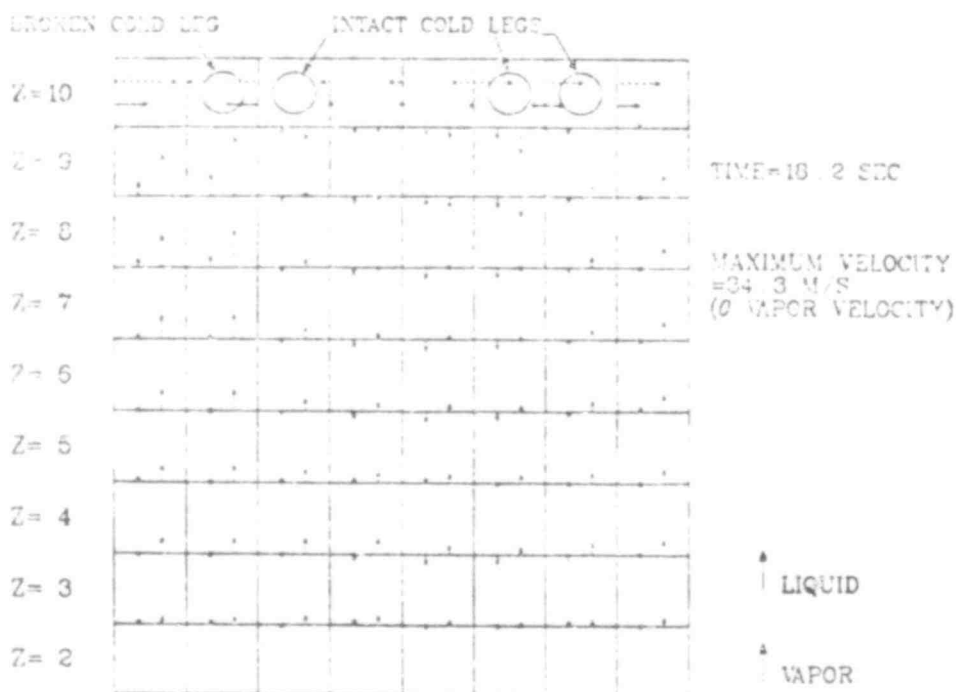


Fig. 43. PWR unwrapped downcomer velocities at 18.2 s.

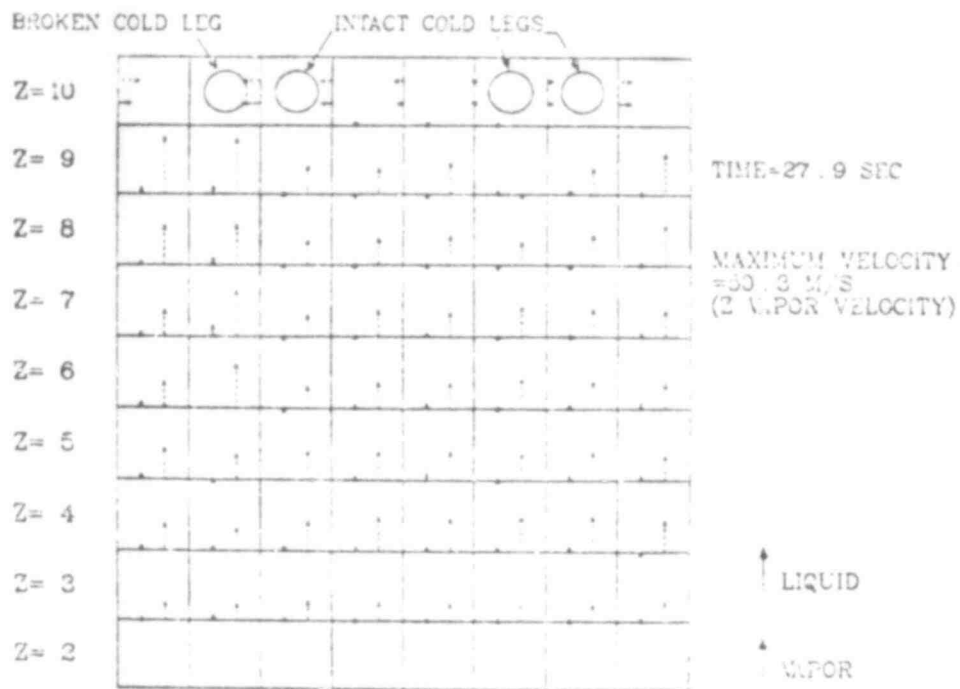


Fig. 44. PWR unwrapped downcomer velocities at 27.9 s.

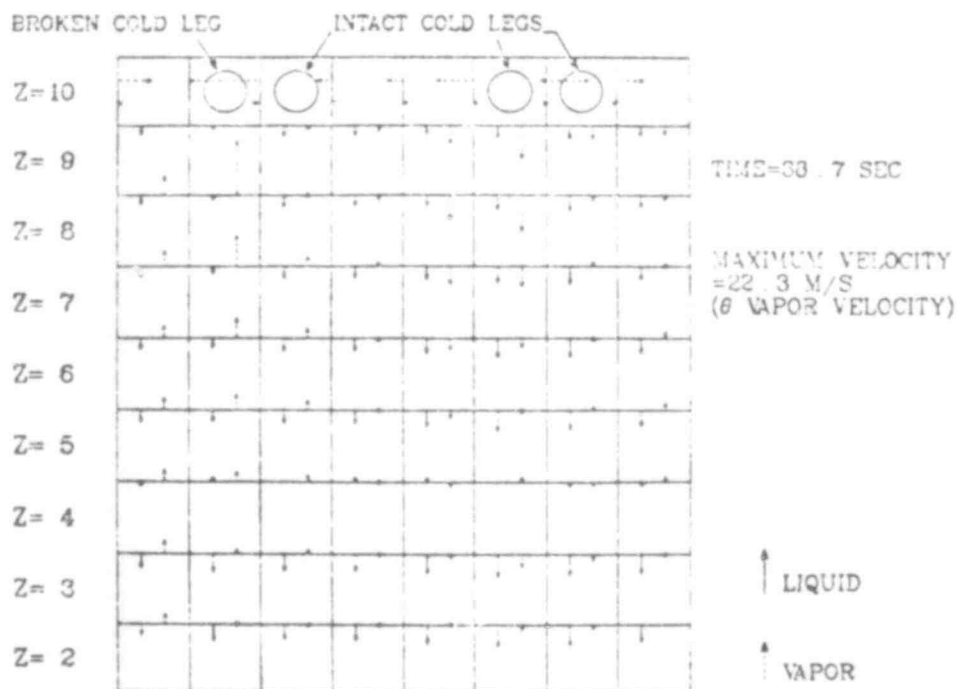


Fig. 45. PWR unwrapped downcomer velocities at 38.7 s.

downcomer. The sequence of important events for the base case is summarized in Table VII.

Probably the most significant conclusion that can be drawn from the base case calculation is that the peak clad temperatures remain far below critical levels even with almost total accumulator bypass. The heating rates during refill and reflood are near adiabatic, indicating that the reflood peak is not being underestimated due to overly optimistic heat transfer modeling.

Midplane cladding temperatures of rods 5, 13, and 21 for the 150% break case are shown in Fig. 46. As can be seen,

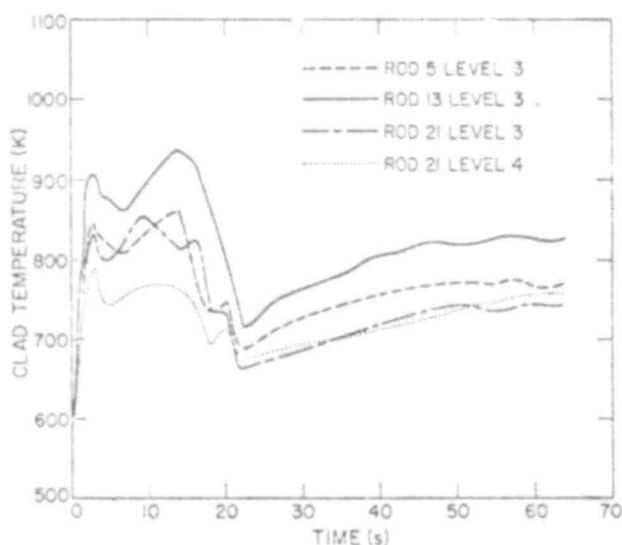


Fig. 46. Cladding temperatures for PWR 150% break case.

TABLE VII
TABLE OF EVENTS

U.S. PWR Sensitivity Study
-- Base Case

Time (s)	Event
0.0	200% double-ended cold-leg break
1.0	HPIS initiated in all intact loops -- setpoint 102.0×10^5 Pa
2.8	First peak clad temperature reached (rod 15 -- 949.7 K)
10.4	Accumulators turned on -- all intact loops -- setpoint 40.8×10^5 Pa
12.0	Bypass period begins
13.7	Second peak clad temperature reached (rod 13 -- 959.6 K)
16.0	Minimum water level in lower plenum reached
16.5	Pressurizer empties (level < 0.1 m) (pressure -- 17.0×10^5 Pa)
18.2	LPIS initiated in all intact loops -- setpoint 12.7×10^5 Pa
27.0	End of blowdown (approximate)
37.0	Bypass period ends -- lower plenum begins to refill
40.0	Accumulators empty in all intact loops
74.8	Peak clad temperature during reflood reached (rod 13 -- 856.6 K)
87.0	All rod clad temperatures turned over (approximate)

the temperatures behave in the same manner as those for the base case. A direct comparison of peak clad temperatures for the base case and for the 150% break case is shown in Fig. 47. The sequence of events of the 150% break case is very similar to that of the base case. Referring to Figs. 40-42, it is evident that the bypass and refill periods are also similar to the base case.

Since the 15 kW/ft base case and 150% break case show almost complete accumulator bypass, an additional calculation was run to examine a complete delivery situation. Rather severe changes in the basic TRAC modeling were required to do this. The interfacial friction in the downcomer region was reduced by several orders of magnitude. The wall friction in the downcomer and the condensation in the injection tees were also reduced. Changing these parameters by such large factors is considered to be unrealistic, but did serve to produce results near the limit of complete liquid delivery. It is believed that these variations far exceed the uncertainty in the modeling. Figure 48 shows the cladding temperatures for the same three rods referenced earlier. The peak temperature again occurred during blowdown and was 950 K. The temperatures dropped well below the high bypass case shortly after accumulator injection was initiated. The

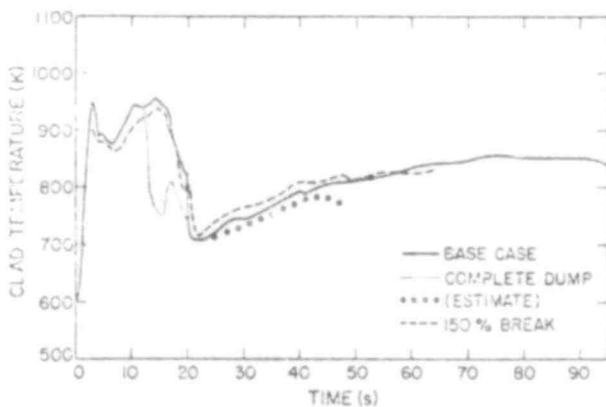


Fig. 47. PWR peak rod (13) cladding temperatures.

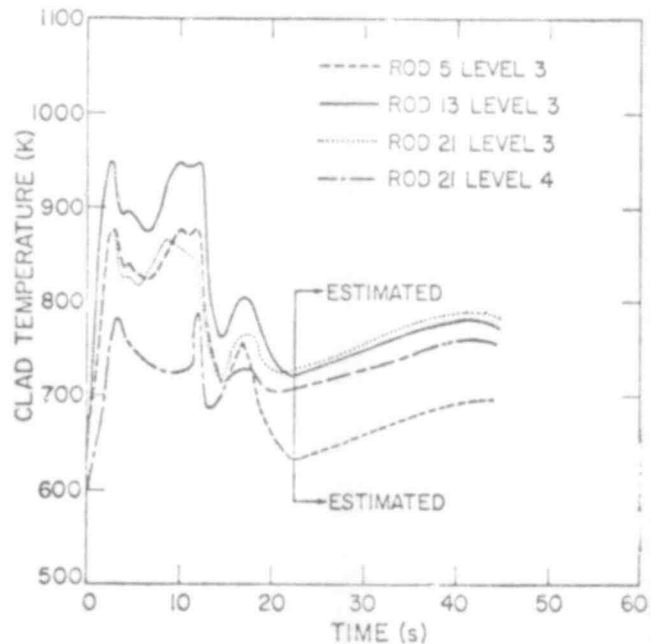


Fig. 48. PWR cladding temperatures for complete dumping case.

resulting peak temperature during reflood was estimated to be about 780 K. It was necessary to estimate the final reflood temperatures because the rather severe model changes required to obtain high delivery rates drastically increased the running time of the code. In any case, the peak temperature is nearly the same as in the high bypass cases, since it still occurs during blowdown. The accumulator flow was bypassed for only about 2 s resulting in about 5% bypass.

The following conclusions can be drawn from these calculations.

1. For the PWR model studied, which had a higher than best estimate linear power, the peak cladding temperatures were always below about 977 K (1 300°F), well below the critical level of 1 477 K (2 200°F). This was found to be true even in cases where substantial downcomer bypass was observed.
2. Peak cladding temperatures in various rods typically occurred during blowdown rather than reflood. This was always true for the hottest rods.
3. The differences in cladding temperatures between the 200 and 150% break cases were negligible.
4. System effects, such as condensation in the cold legs and the void fraction in the cold legs at injection, appear to be important in the overall behavior of liquid delivery.
5. The best estimate modeling currently in TRAC predicts substantial bypass for this reactor model. Comparisons with experiments to date indicate this modeling is reasonable.
6. If the modeling is changed to substantially reduce bypass, the peak temperature remains about the same since it occurred during blowdown, but the temperatures reached during reflood are decreased.

2. TRAC Calculations of the Japanese Cylindrical Core Test Facility

(D. Dobranich, Q-6)

An initial TRAC calculation of the CCTF was completed. The TRAC model for this calculation is the same as that reported previously.¹⁴ The calculation was run for about 33 s of problem time (average time step size of 3 ms) requiring 4.5 h of CDC-7600 CPU time.

The initial conditions for this run are listed in Table VIII. In general, most of the initial conditions are currently not well known and have been estimated from fragmentary information. Improved calculations will be made when more detailed information becomes available.

Figures 49-52 show the general behavior of the system during the transient. Figure 49 shows that the water inventory in the vessel initially decreases due to flashing. At approximately 9.0 s the ECC water has reached the vessel at which time the vessel water inventory begins to increase. The vessel water inventory continues to rise until the accumulator has emptied at approximately 16.0 s. Figures 50 and 51 show the lower plenum liquid temperature and pressure, respectively. The lower plenum liquid temperature has decreased to about 390 K after 30 s but is gradually rising while the pressure has stabilized to about 3.5×10^5 Pa. The LPIS continues to operate but does not supply sufficient liquid to refill

TABLE VIII
CCTF INITIAL CONDITIONS

Power	11.6 Mw (ANS decay heat correlation)
Cladding temperature	873 K
System pressure	5.83×10^5 Pa
Break pressure	3.0×10^5 Pa
Vessel wall temperature	573 K
Other vessel structural material temperature	430 K
Primary piping temperature	430 K
Water inventory	Lower plenum, injection piping, and header filled with saturated liquid
Accumulator	Liquid volume of 3.97 m^3 containing subcooled water at 330 K
LPIS	Constant injection rate of 25.0 kg/s using subcooled water at 330 K
Steam generator (secondary side)	60.0×10^5 Pa, 547 K, average void fraction = 0.25

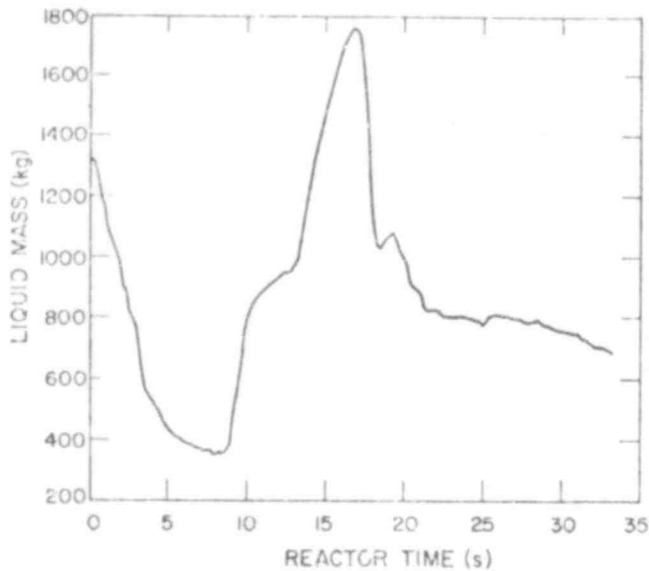


Fig. 49. CCTF vessel water inventory.

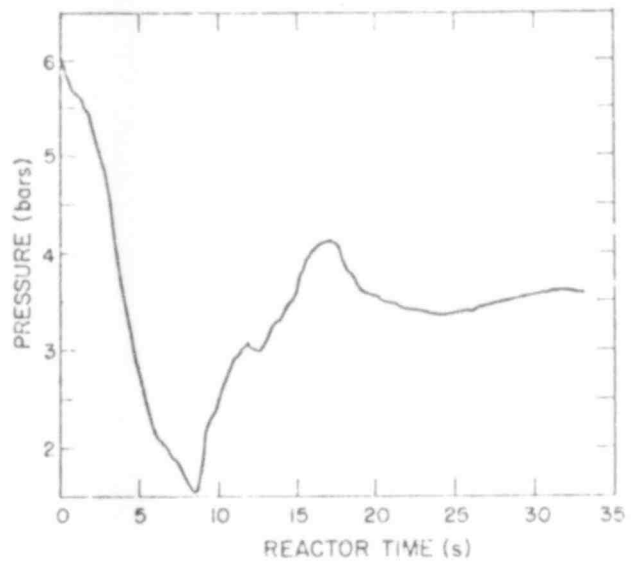


Fig. 51. CCTF lower plenum pressure.

the lower plenum. The cladding temperatures continue to increase during this period as shown in Fig. 52.

Figures 53-56 show the flow patterns in the downcomer, which has been graphically unwrapped to display the results. At 3.6 s the liquid is moving toward the broken cold leg as the system blows down from the initial 5.93×10^5 Pa. At 9.1 s the ECC liquid has

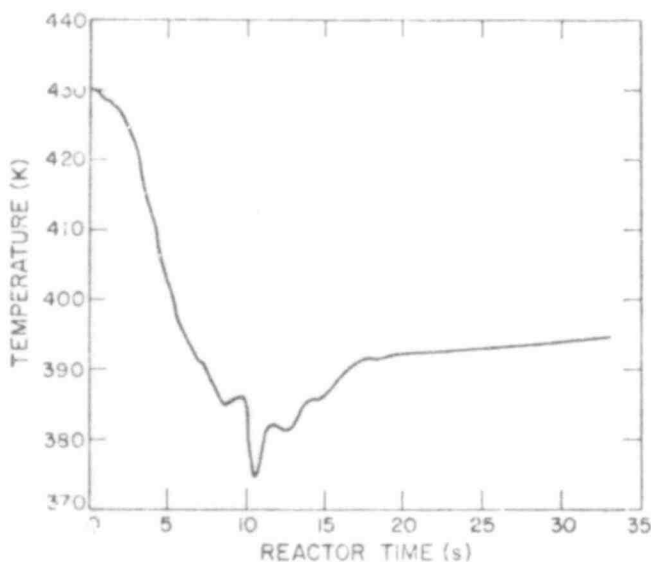


Fig. 50. CCTF lower plenum liquid temperature.

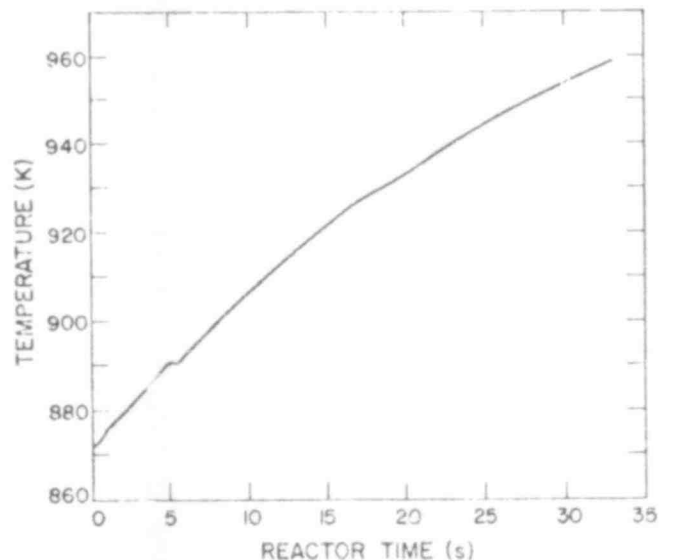


Fig. 52. CCTF cladding temperature (Rod #10, Level 2).

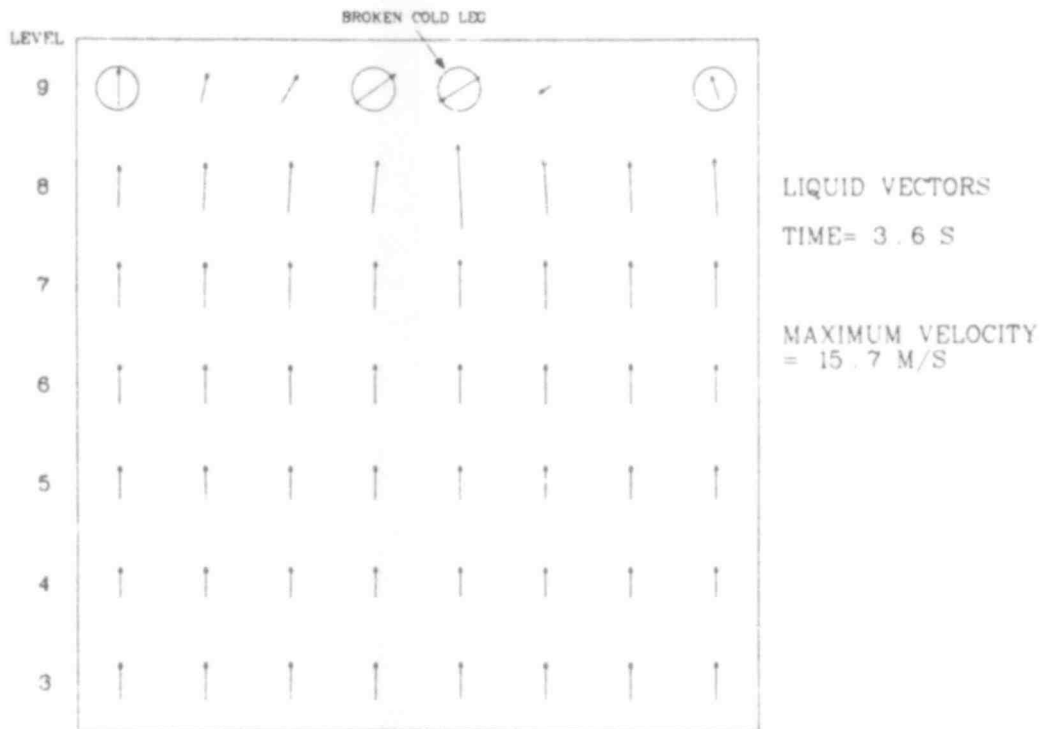


Fig. 53. CCTF unwrapped downcomer velocity vectors at 3.6 s.

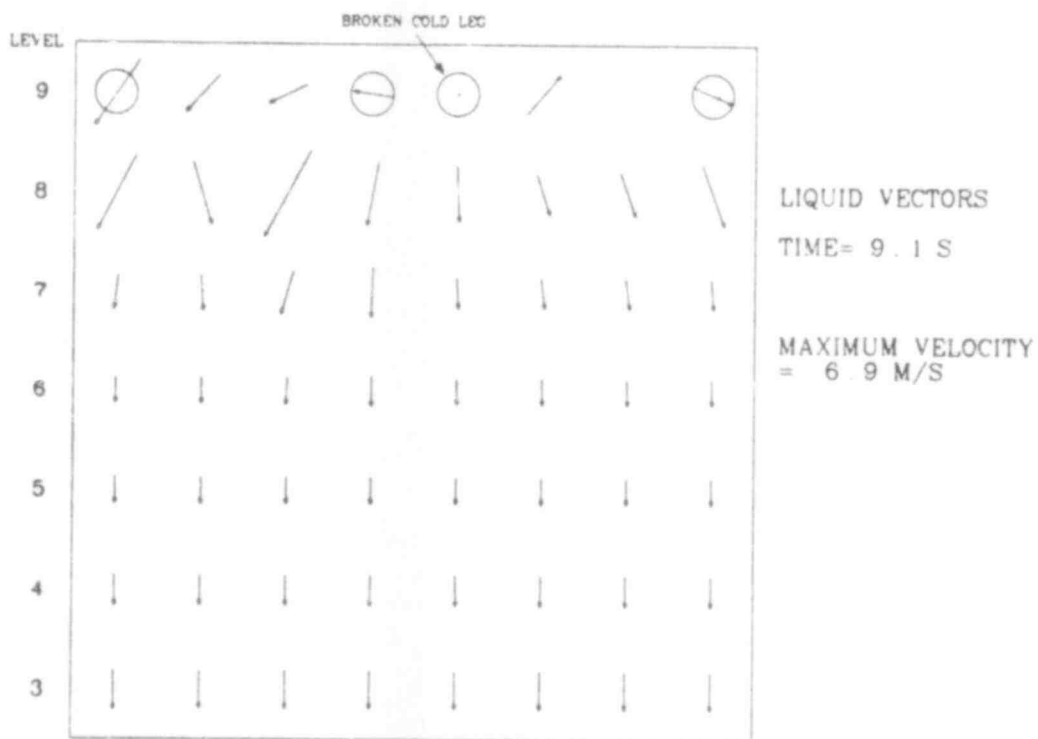


Fig. 54. CCTF unwrapped downcomer velocity vectors at 9.1 s.

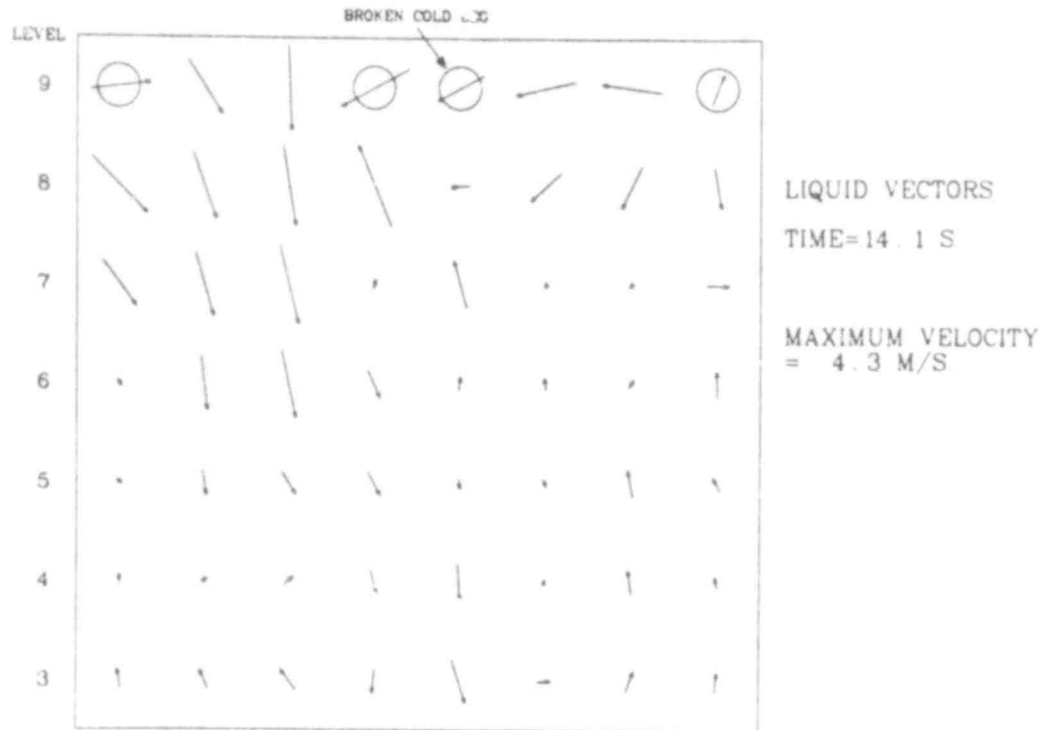


Fig. 55. CCTF unwrapped downcomer velocity vectors at 14.1 s.

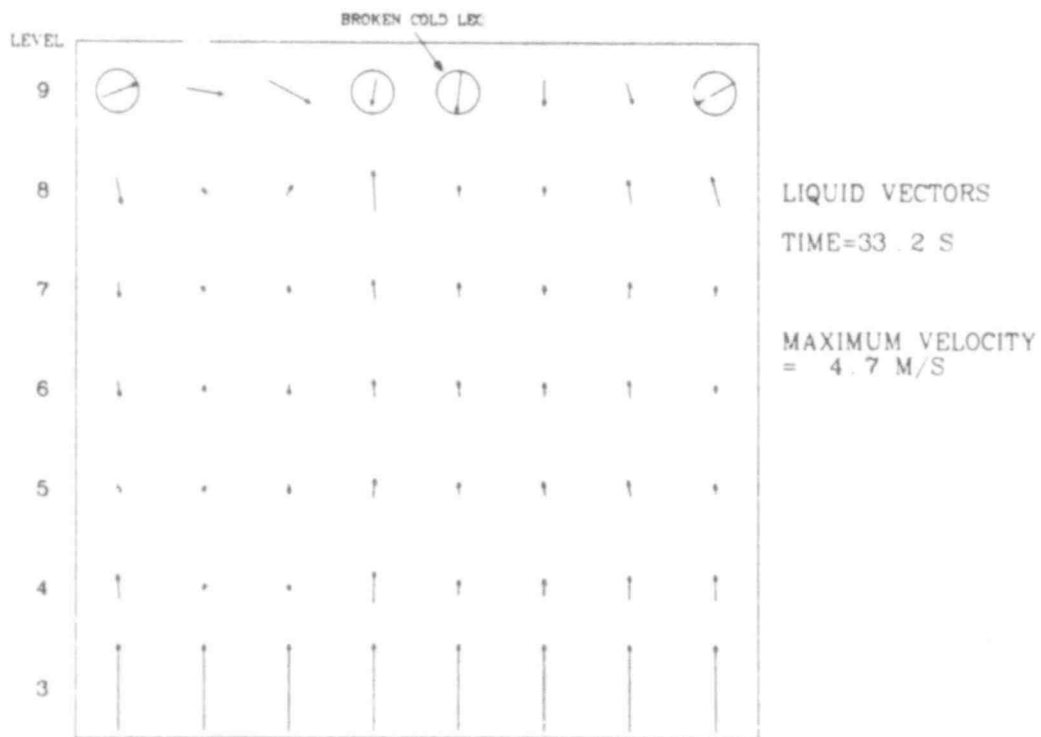


Fig. 56. CCTF unwrapped downcomer velocity vectors at 33.2 s.

reached the vessel and is penetrating into the downcomer and lower plenum (ECC liquid is injected into all three intact cold legs). At 14.1 s the accumulator is nearly empty and flows within the downcomer are beginning to turn around and go back out the break. At 33.2 s the liquid is flowing out the break faster than the LPIS can inject liquid in. The vessel still contains enough stored energy to flash the ECC water and pressurize the vessel enough to force the flow outward. Also contributing to the outward flow is the steam binding which occurs in the broken loop steam generator.

Several important conclusions can be made based on this initial TRAC calculation of the CCTF.

1. The header configuration does an adequate job at distributing the ECC liquid to the cold legs and in reducing the temperature change of the injected water.
2. The liquid initially in the lower plenum flashes, providing steam flows in the vessel similar to those found in a PWR during the refill stage.
3. ECC water is able to penetrate into the downcomer and lower plenum. There is very little bypass during the time the accumulator is supplying liquid.
4. Problems are encountered due to the fact that there are four loops but only two steam generators. Liquid from the broken cold leg enters the steam generator where it flashes. This creates a back pressure feeding through the hot legs and into the upper plenum which in turn slows the refilling rate. This is a steam binding effect; however, the liquid going into the steam generator comes from the broken cold leg rather than the hot legs. Steam binding does not occur on the intact loop side.
5. If the accumulator does not provide enough liquid to refill the lower plenum, the LPIS will be of little or no help. The system will continue to blow down (liquid in the vessel will be vaporized) and the core will not be quenched. Therefore, the accumulator liquid volume will be increased in future calculations.

3. TRAC Calculations of the INEL Air-Water Test Series

(M. M. Giles, INEL and P. B. Bleiweis, Q-6)

Analyses have been performed with TRAC to simulate the INEL Air-Water Test Facility (AWTF). Seven different air-water tests in the Y-Test Series were analyzed and the results are presented below.

The analyses were performed using a two-dimensional TRAC model of the AWTF with the Japanese Atomic Energy Research Institute (JAERI) 4-hole upper core support plate (UCSP). As shown in Fig. 57, the TRAC model consists of a vessel component with attached

pipes, fills, and breaks to represent the air and water injection sources and hot-leg outlet. The vessel component has 12 axial levels, the interfaces between most levels being placed at elevations where vessel flow area changes occur. Levels 7, 8, and 11 are required to provide pipe connection points and level 9 is included to represent the gamma densitometer location. Each axial level is divided in the X-direction into five cells. The spacing of these cells was chosen to allow modeling of the openings in the UCSP. On the axial level representing the UCSP (level 7), the two outside cells and the center cell are completely blocked off from all adjoining cells. The two remaining cells on that level are fully open in the axial direction, each open cell representing two of the UCSP orifices.

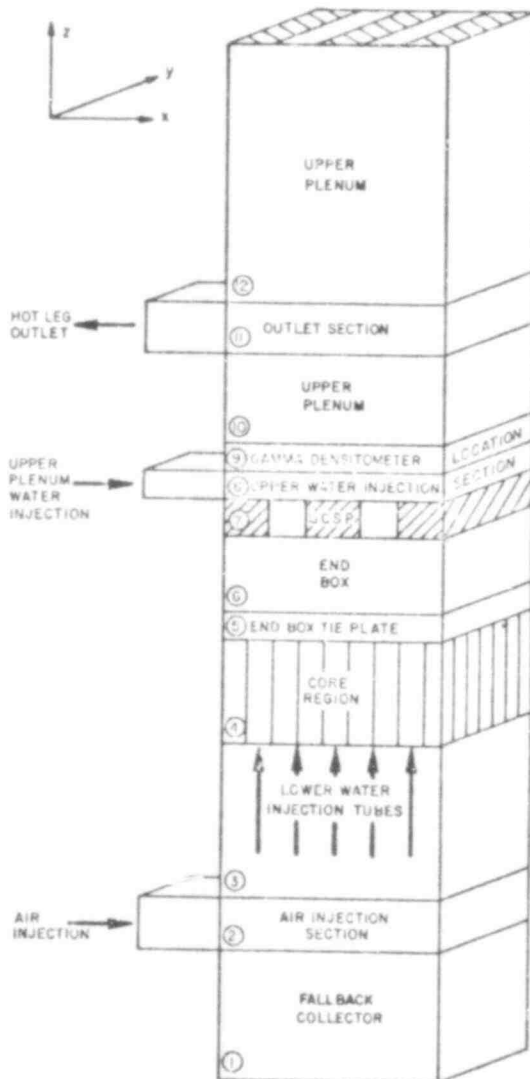


Fig. 57. TRAC air-water vessel model.

The water injection is simulated by vertical pipes connected to the plane separating axial levels 3 and 4. The upper plenum water injection is modeled by a pipe connected to a single outside cell on axial level 8, just above the UCSP. In the actual test vessel the upper plenum water injection takes place around the entire perimeter of the UCSP, but the single injection point used in the TRAC model is sufficient judging from the fairly uniform steady-state distribution of mixture density calculated across axial level 8. Lower core air injection is achieved by means of a single pipe connection to the vessel on axial level 2. This again is unlike the actual test apparatus where air is input through two injectors, one on each side of the vessel. However, the steady-state TRAC results indicate that the axial air velocities in the core are symmetrically distributed about the center cell by the time the air reaches axial level 4, justifying the use of a single air injection point.

A total of seven different air-water tests were analyzed using the previously described model. The flow conditions for these tests are summarized in Table IX. An initial TRAC run was begun with all components filled with stationary air at a pressure of 0.134 MPa. Air injection and upper plenum water injection were then begun and the model was run to a quasisteady-state condition with constant

TABLE IX
AIR-WATER TEST FLOW CONDITIONS

Test Number	Air Flow Rate (m ³ /s)	Lower Water Injection Rate (m ³ /s)	Upper Water Injection Rate (m ³ /s)
Y02	0.152	0.	0.932E-3
Y06	0.169	0.	0.915E-3
Y10	0.187	0.	0.909E-3
Y25	0.147	0.188E-3	0.777E-3
Y34	0.187	0.150E-3	0.767E-3
Y49	0.147	0.465E-3	0.443E-3
Y58	0.187	0.467E-3	0.447E-3

average air flow and with water froth exiting the vessel through the hot-leg outlet. This condition was characterized by large fluctuations in vessel pressure and hot-leg mixture velocity as shown in Figs. 58 and 59. This situation is similar to that in the actual test vessel where violently surging froth and slugs are observed in steady-state operation. About 20 s were required for the froth to reach the hot-leg axial level. The model was initialized in this manner using the actual test conditions for test Y10. On subsequent restart runs, the air and water inlet flows were reset to represent the particular test being simulated and the code was run for about 10 s of model time to allow the fallback rate into the water collector (axial level 1) to be determined. Typical fallback results are presented in Fig. 60, which shows the total volume of water in the fallback collector plotted as a function of time for test Y02. The plot is clearly linear after about 21 s. The brief nonlinear period from 20-21 s is due to the readjustment of flows within the vessel while changing from test Y10 conditions to test

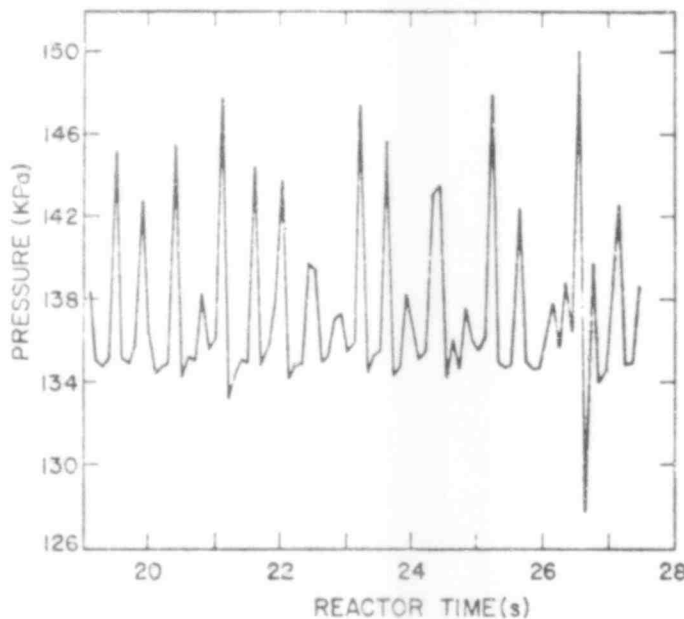


Fig. 58. Vessel pressure for air-water test Y10.

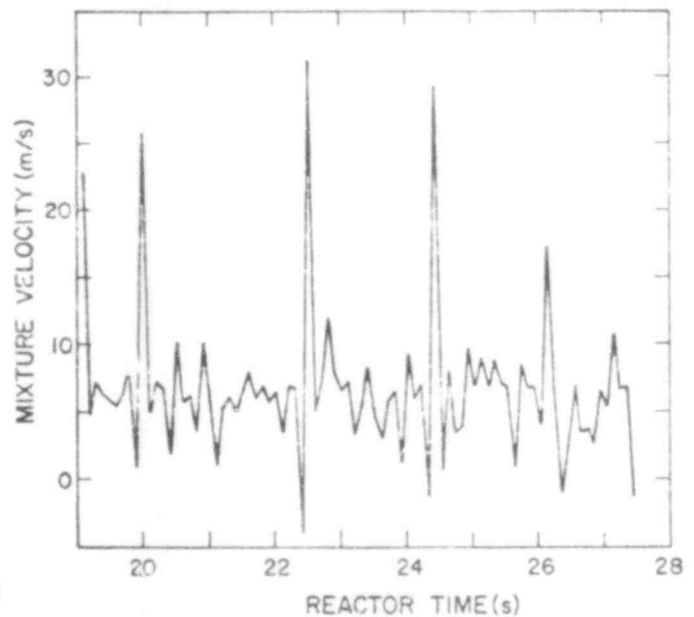


Fig. 59. Hot-leg mixture velocity for air-water test Y10.

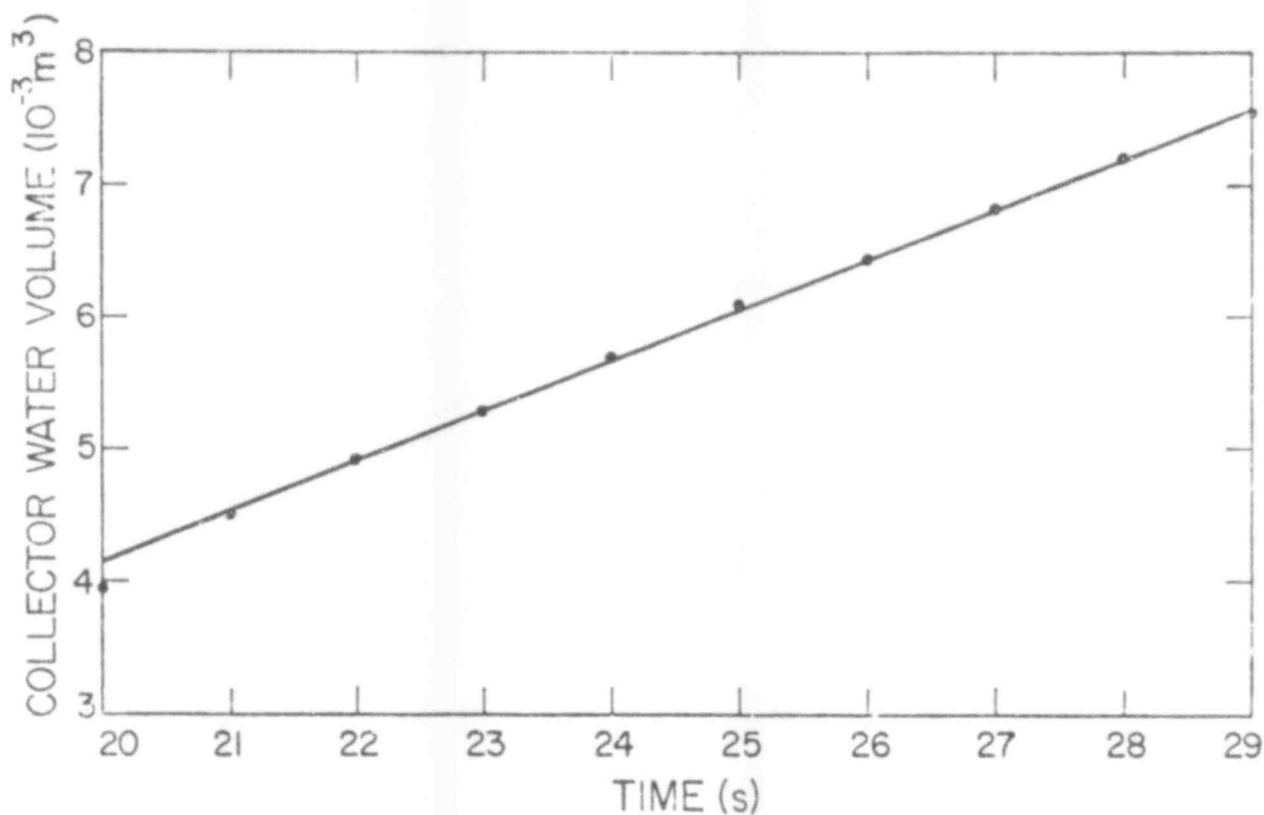


Fig. 60. Calculated fallback collector water volume for air-water test Y02.

Y02 conditions. The fallback rate for this test was determined from the slope of the linear portion of this plot. The same method was used for all other tests, and the results are tabulated in Table X. The slopes of the various fallback plots were determined by inspection, and it is estimated that the uncertainty in this method is typically $\pm 5\%$ leading to an uncertainty of this approximate magnitude in the TRAC fallback rates.

For each test, plots of vapor fraction were made for every cell on axial level 9. An example of these plots for test Y06 is shown in Fig. 61. From these plots, the time-averaged air fraction was estimated for each cell on axial level 9, and a volume-weighted average of these results was used to estimate the level 9 air-water mixture density for comparison with test gamma densitometer measurements. The uncertainty in these estimates is quite large,

TABLE X
FALLBACK AND DENSITY RESULTS FOR AIR-WATER TESTS

Test Number	Experimental Fallback Rate (m ³ /s)	TRAC Calculated Fallback Rate (m ³ /s)	Experimental Froth Density (kg/m ³)	TRAC Calculated Froth Density (kg/m ³)
Y02	0.471E-3	0.379E-3	366	390
Y06	0.332E-3	0.331E-3	301	266
Y10	0.273E-3	0.312E-3	315	270
Y25	0.707E-3	0.578E-3	375	260
Y34	0.370E-3	0.384E-3	272	260
Y49	0.726E-3	0.832E-3	351	260
Y58	0.196E-3	0.718E-3	260	280

perhaps as great as $\pm 30\%$. The TRAC and experimental density results are tabulated in Table X.

A comparison of experimental and TRAC fallback rates as shown in Table X indicates that with one exception (test Y58) these quantities are in good general agreement, the largest discrepancy

noted in the first six tests being about 20%. A similar general agreement is seen between the experimental and TRAC upper plenum froth densities. A useful comparison of TRAC and experimentally obtained fallback results is also shown in Fig. 62. In this figure, the square root of gas (air) Kutateladze number is plotted vs the liquid (fallback) Kutateladze number. These Kutateladze numbers were evaluated using the vessel flow area at the lower end box tie plate, i.e., at the point of

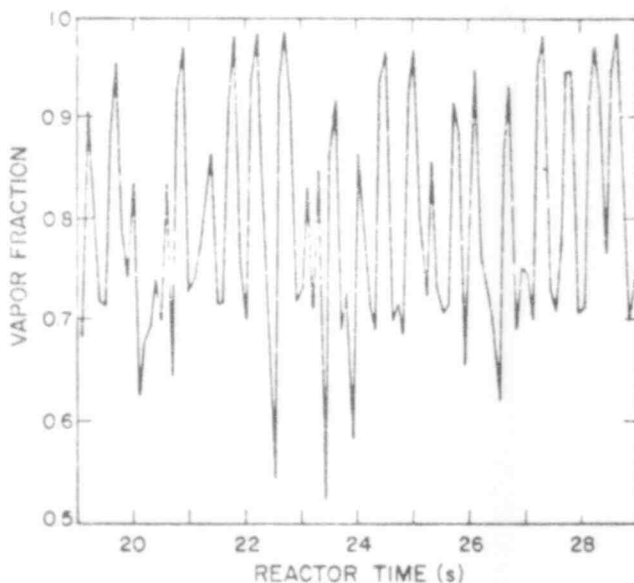


Fig. 61. Vapor fraction at gamma densitometer level (air-water test Y06).

508 100

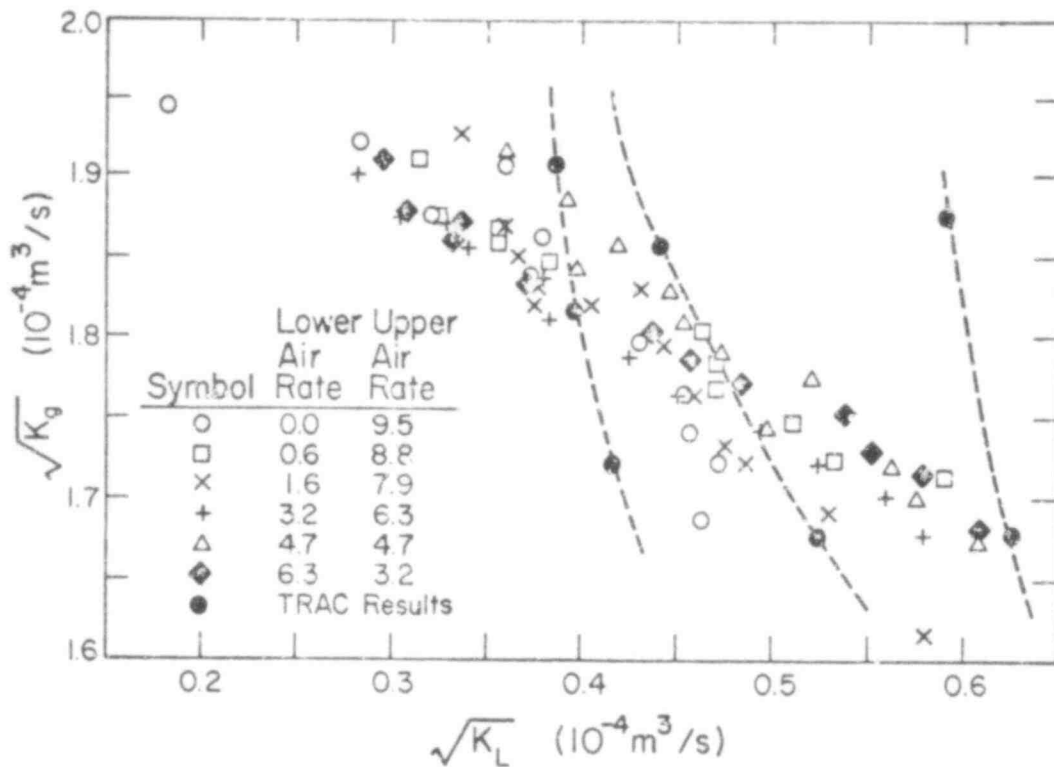


Fig. 62. Square root of gas vs liquid Kutateladze numbers for the density and water injection ratio tests.

maximum vessel flow restriction. These quantities are plotted for the seven TRAC analyses as well as for all of the X and Y Series test results. The TRAC results are labeled by their corresponding test number.

The air-water results presented above indicate that the basic physical modeling employed in TRAC is probably adequate for the prediction of the behavior near the UCSP in tests similar to these. However, it would be useful to perform TRAC calculations of the planned Oak Ridge steam-water tests on larger geometries to check the effects of scale.

C. Thermal-Hydraulic Research for Reactor Safety Analysis

(C. W. Hirt, T-3)

The analytical research program is designed to investigate specific problems that arise in LWR safety considerations and to develop new theoretical and numerical analysis methods. During this quarter significant progress was made in both the development and applications areas. A short-term study was completed that investigated several proposed steam sources for large-scale German and Japanese experiments. Another program has been the development of improved phase-change models and their use in predicting critical two-phase flows. Results reported here show excellent agreement in comparisons made with the large-scale Marviken blow-down tests. In preparation for the detailed investigation of droplet entrainment and de-entrainment in complex geometries, a new computational method for treating droplet fields with a distribution of drop sizes has been developed.

1. Steam Source Calculations for Large-Scale Japanese and German Experiments

(W. C. Rivard and M. D. Torrey, T-3)

Blowdown calculations have been performed with SOLA-LOOP and K-FIX for the large vessels proposed to supply steam for refill-type experiments. The essential features of the two vessel designs are shown in Fig. 63. Vessel (A) is intended to be used in conjunction with the Japanese experiments while vessel (B) is similar to the Routh's storage tank that is intended for use with the German experiments. In each case, the vessels contain saturated steam-water mixtures as shown and the discharge valves are slowly opened over a 2 s interval. Vessel (A) is pressurized initially to 0.6 MPa while vessel (B) is pressurized to 2.0 MPa. The calculations were performed to 4 s on vessel (A) and to 20 s on vessel (B). As the discharge valve is opened and the release wave reaches the water it immediately begins to boil. This results in a cooling of the remaining water because of the latent heat removed. In an equilibrium situation, the vessel pressure is always at the

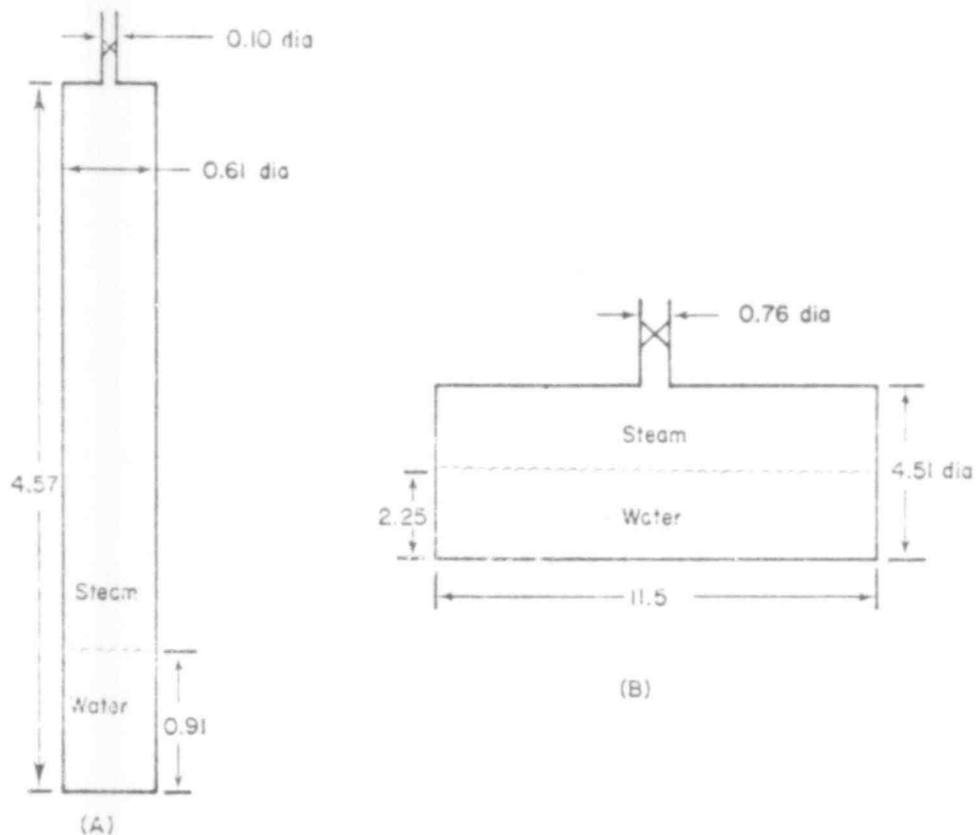


Fig. 63. Geometry and water levels for the two proposed steam source vessels for the Japanese (A) and German (B) large-scale experiments. Dimensions are in meters.

saturation value; hence, as the boiling continues the water temperature and the vessel pressure continuously decrease.

The calculated discharge flow rate and vessel pressure, which is very nearly uniform throughout the vessel, are shown for vessel (A) in Fig. 64a and 64b and for vessel (B) in Fig. 65a and 65b. The differences between the calculated results largely reflect differences in the vapor production rates. The rate used in SOLA-LOOP was that described in Ref. 15, which resulted in a few degrees centigrade departure from equilibrium in the discharge pipe. The rates of boiling and condensation used in K-FIX were large enough to maintain an equilibrium environment. At this time we cannot ascertain which flow rate best describes reality. The results indicate, however, the relative sensitivity of the flow rate to a departure of a few degrees centigrade from equilibrium. An improved vapor production model is being developed as part of our continuing effort in this area. Application of the new model to the large-scale

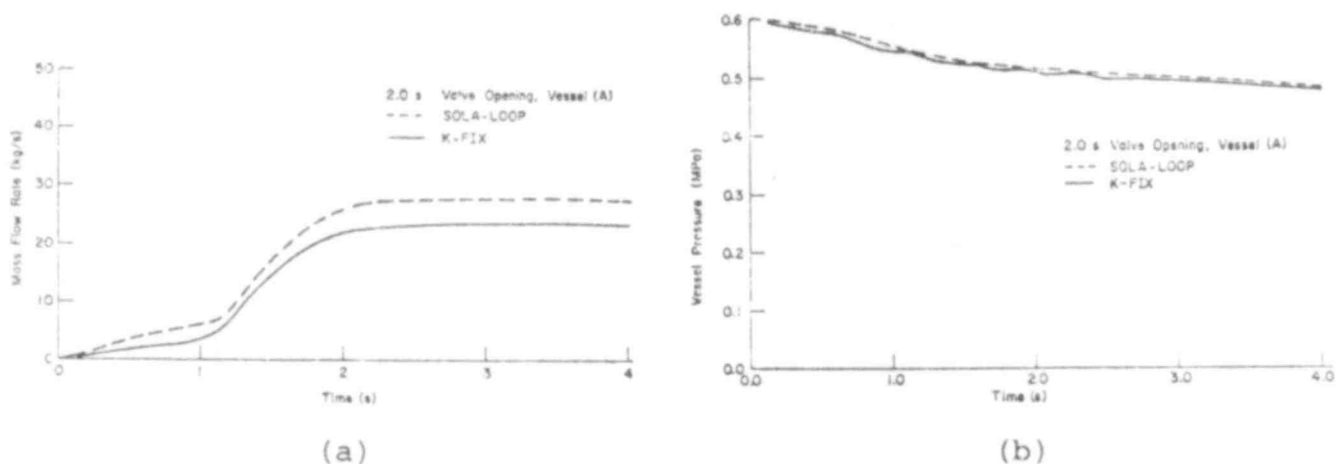


Fig. 64. Calculated discharge flow rate and vessel pressure for vessel (A) using the SOLA-LOOP and K-FIX codes.

Marviken experiments is discussed elsewhere in this report. Both calculations were made without slip. A calculation with slip was made with SOLA-LOOP, in which the gas speed was approximately twice the liquid speed, and essentially the same results were obtained.

2. Large-Scale Critical Flow Analysis

(J. R. Travis and W. C. Rivard, T-3)

An important part of LWR safety analyses is the prediction of critical flow rates or maximum discharge flow rates from reactor coolant pipes. Current critical flow models have been developed¹⁵ for the most part from data based on small-scale experiments. The

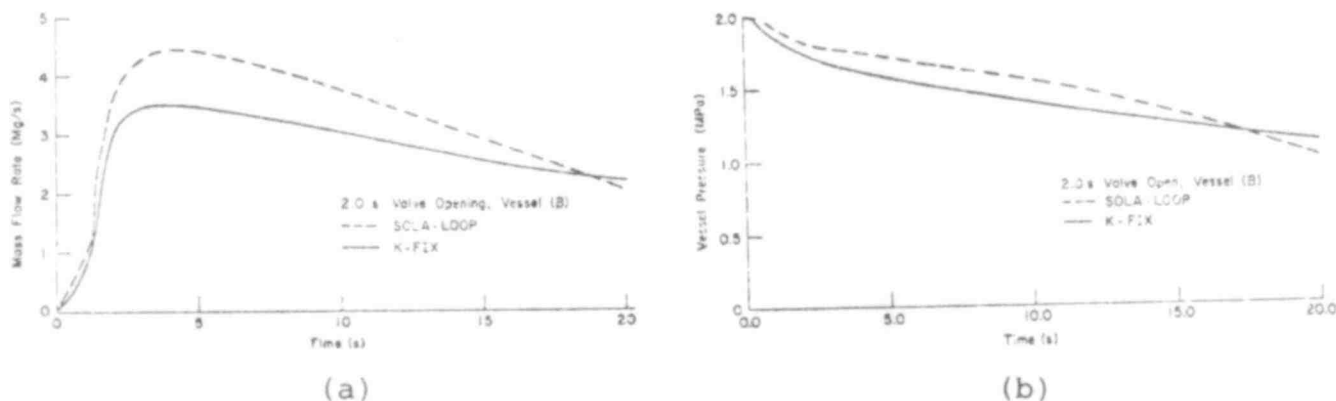


Fig. 65. Calculated discharge flow rate and vessel pressure for vessel (B) using the SOLA-LOOP and K-FIX codes.

purpose of the Critical Flow Test (CFT) project initiated at the Marviken Test Station in Sweden is to provide critical flow data for large diameter pipes in the range found in present reactor coolant systems.

The CFT facility contains a cylindrical shaped pressure vessel that is 21.52-m-tall and 5.22 m in diameter. A 0.752-m-diameter discharge pipe (Fig. 66) is connected to the bottom of the pressure vessel. At the lower end of the pipe, any one of the six nozzles

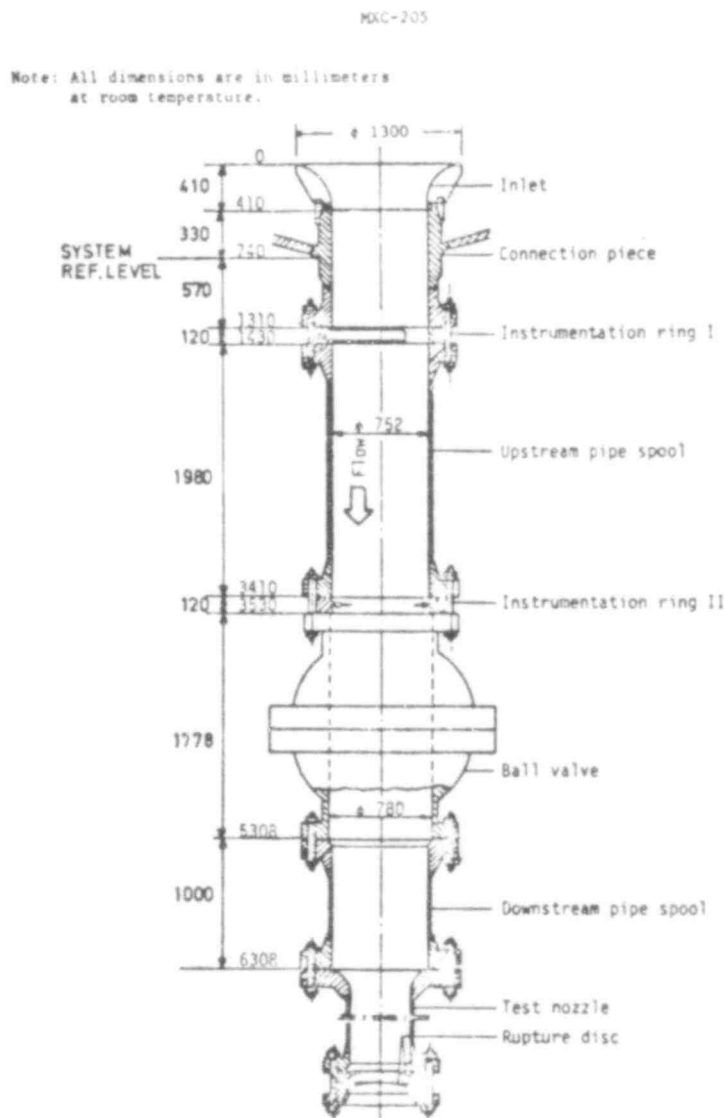


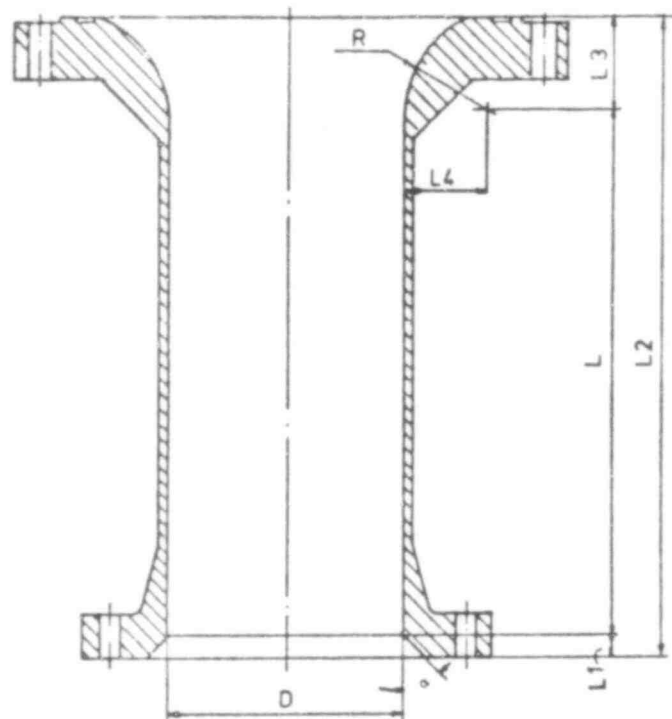
Fig. 66. Marviken discharge pipe, test nozzle, and rupture disc assembly.

shown in Fig. 67 may be attached. For each test, subcooled water resides at the bottom of the vessel and grades to saturated water above with a saturated steam cover volume at the top. Pressures, temperatures, and fluid levels are measured throughout the test facility, with particular attention being given to the fluid conditions in the discharge pipe, at the nozzle entrance, and in the nozzle itself.

We have analyzed tests 1, 2, and 4, and have obtained very good agreement between the calculated results and the observed data. Test 3 is the same as Test 4 except Test 3 has less initial

MDC-205

Note: All dimensions are in millimeters at room temperature.



D	L/D	L*	L1	L2	L3	L4	R	α
200	2.5	503	105	708	100	100	100	45°
300	1	290	55	495	150	150	150	45°
300	3	895	55	1100	150	150	150	45°
509	0	0	33	223	273	250	250	30°
509	1	510	55	790	225	220	250	45°
509	3	1520	55	1800	225	241	250	45°

* Test section length.

Fig. 67. Dimensions of the Marviken test nozzles.

508 106

subcooling, 15°C as compared with 30°C. Tests 1 and 2 were conducted using the test nozzle with a 300 mm constant diameter test section having a length-to-diameter ratio of 3. For these tests, the initial pressure was 5.0 MPa, and the initial subcoolings were 30°C and 15°C, respectively. Test 4 was conducted using the test nozzle with 509 mm constant diameter test section having a length-to-diameter ratio of 3 and essentially the same initial conditions as Test 1.

In the comparisons with the observed data, Figs. 68-70, we have performed a homogeneous equilibrium calculation (i.e., we have used a phase-change rate that is sufficiently high to keep the phases in equilibrium at all times and locations) and a calculation without phase change. In all tests, the data fall between these limiting cases, indicating that the flows are indeed non-equilibrium. Results from a nonequilibrium phase-change model are also presented in these figures, and are seen to be in very good agreement with the data. The nonequilibrium phase-change model, which is currently under development, makes use of the classical conduction limited analysis with the thermal diffusivity being replaced with an effective diffusivity, which is the sum of the

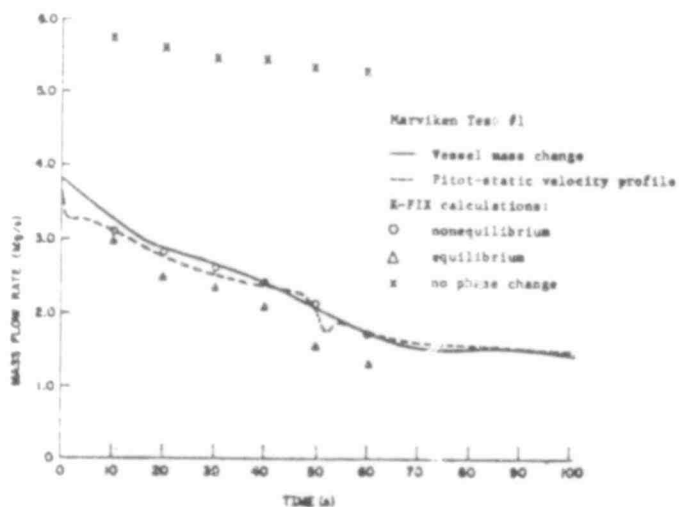


Fig. 68. Mass flow rates for Marviken Test #1.

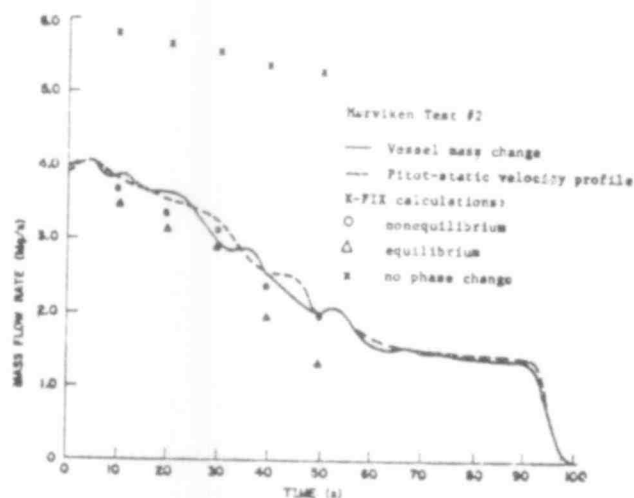


Fig. 69. Mass flow rates for Marviken Test #2.

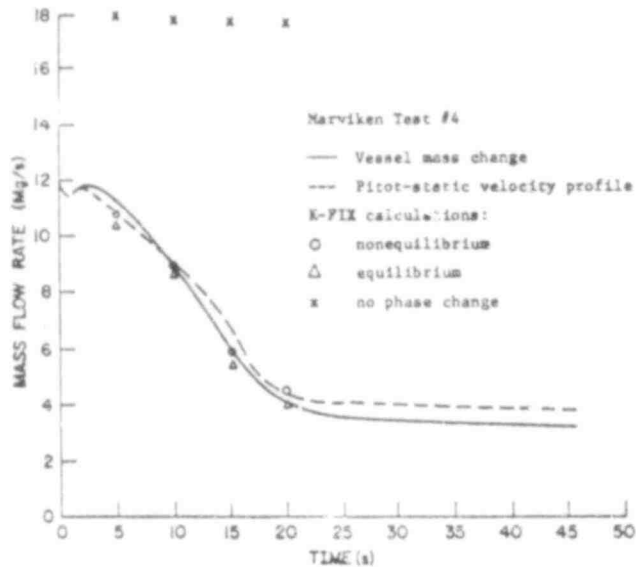


Fig. 70. Mass flow rates for Marviken Test #4.

thermal and turbulent contributions. We feel that several more comparisons with different critical flow configurations should be made before the model can be recommended for general use.

The results presented have been obtained with K-FIX from detailed quasisteady flow calculations that focus on flow through the nozzle for the development of the new nonequilibrium, vapor production model. Calculations that include the full discharge pipe and vessel have also been made using the SOLA-LOOP network code. Preliminary comparisons with the measured flow rate for Test #1 show good agreement to 60 s, which is as far as the calculation was run. Calculations of this type are necessary to investigate the late time portion of the blowdown because void fraction data at the nozzle entrance are lacking for many of the tests. The system calculations also allow additional comparisons to be made with data taken in the discharge pipe and vessel. Work in this area will be continuing into the next quarter.

3. Droplet Spray Modeling

(J. K. Dukowicz and T. D. Butler, T-3)

We are developing a new numerical technique to calculate the dynamics of dispersed droplets in a gaseous environment. This methodology consists of a fully interacting combination of an Eulerian representation for the continuous phase and a Lagrangian particle representation for the droplets. The Lagrangian description avoids numerical diffusion of the droplets while permitting individual attributes such as droplet size, temperature, and composition to be statistically assigned for each particle.

508 108

We anticipate that this new methodology will find its greatest utility for those problems in which a spectrum of droplet sizes is important to the dynamics. It appears to be a unique tool for analyzing current de-entrainment experiments. It also provides an alternative approach to the advanced two- and three-field models developed for analysis of reactor safety problems, and can be used to assess the accuracy of these latter approaches in selected problems.

Thus far, we have developed and applied the methodology to problems in incompressible two-phase flow without phase change. In this section we briefly outline the method of solution and show example solutions from two different applications. Complete details of the methodology will soon appear in a subsequent publication.¹⁶ Techniques to include the effects of compressibility and evaporation are now being developed. These extensions will appear in a subsequent progress report.

a. Governing Equations and Solution Procedure

The governing equations are the gas continuity equation,

$$\frac{\partial \theta \rho_g}{\partial t} + \nabla \cdot \rho_g \underline{u}_g = 0, \quad (3)$$

where θ is the void fraction and ρ_g and \underline{u}_g are the gas density and velocity, respectively. The momentum equation takes the form

$$\begin{aligned} \frac{\partial \theta \rho_g \underline{u}_g}{\partial t} + \nabla \cdot \theta \rho_g \underline{u}_g \underline{u}_g = & - \theta \nabla p + \theta \rho_g \underline{g} \\ & + \nabla \cdot \nu \theta \nabla \cdot \nu \theta \underline{u}_g - \frac{1}{V} \sum_k m_k \frac{d\underline{u}_{pk}}{dt}, \end{aligned} \quad (4)$$

in which p is the pressure, g is the acceleration due to gravity, ν is the kinematic viscosity (or the eddy viscosity in turbulent

flow). The last term in this equation represents the momentum exchange between the droplets and the gas. The indicated summation is over all the particles in a subvolume V , which is taken to be the volume of a computational cell in the finite difference solution procedure; m_k is the mass of particle k , and \underline{u}_{pk} is its velocity. The asterisk implies that the pressure gradient and gravity forces on the particle are not included in the summation. The particle equations are:

$$\frac{d\underline{x}_k}{dt} = \underline{u}_{pk} \quad , \quad (5)$$

in which \underline{x}_k is the position, and the momentum equation is,

$$m_k \frac{d\underline{u}_{pk}}{dt} = - \frac{m_k}{\rho_p} \nabla p + m_k \underline{g} + D_k (\underline{u}_g - \underline{u}_{pk}) \quad , \quad (6)$$

where ρ_p is the particle density and D_k is the particle drag function. The pressure gradient term in this equation is usually small but it is retained for consistency with the corresponding term in the two-fluid equations.¹⁷ The drag function is taken to be,

$$D_k = 6\pi\mu_g r_k + 1/2 \pi r_k^2 \rho_g C_D |\underline{u}_g - \underline{u}_{pk}| \quad , \quad (7)$$

where μ_g is the gas viscosity, r_k is the particle radius, and C_D is the drag coefficient. This assumes that the drag force is the sum of the Stokes' drag and the form drag.

Briefly, the solution procedure through one time cycle is accomplished in the following way.

- (1) Equation (5) is used to update particle positions using velocities from the previous time step. The new void fraction is then computed.
- (2) Using a predictor-corrector method, the particle drag function is evaluated, and intermediate particle and gas velocities are obtained using a linearly implicit technique.
- (3) The final advanced time velocities and pressures for the gas are obtained by iteration using a

technique similar to that used in the MAC method.¹⁸

- (4) Finally, the particle velocities are updated to account for the changes in gas velocities and pressure obtained in the iteration.

b. Numerical Examples

Spray Injection

The first application of this technique is to the problem of droplet spray injection into a quiescent gas medium. This problem is a comprehensive test of the method because the penetration and spread of the spray are strong functions of the particle size distribution and the coupling between the droplets and the gas. The spray has sufficient momentum to entrain the surrounding gas. In turn, the motion of the gas in the vicinity of the spray reduces the resistance to droplet motion and allows the spray to penetrate much further than would otherwise be the case.

Figure 71 summarizes the results of a number of calculations for a spray from a single-orifice injector. Excellent agreement between computations and experimental data of Hiroyasu and Kadota¹⁹ is obtained for a wide range of gas pressures. The figure also shows a scaled cross section of the spray indicating the shape of the spray. The shape of the droplet size distribution function was determined experimentally while the mean droplet size was inferred from a Weber number criterion for droplet stability.

Upper Head De-entrainment

Another example solution deals with the de-entrainment phenomena in which droplets carried by an air stream are removed by obstacles in the flow. The motivation for such studies is to determine the rate of de-entrainment of water by the presence of structures in the upper plenum of a PWR during the reflood phase of a postulated accident sequence.

This particular calculation was performed to give insight for the design of the upper plenum of the Japanese Slab Core Test Facility (CCTF). The upper plenum in this facility has a width of approximately 25 cm. Two configurations for the placement of upper plenum structures were considered: a staggered arrangement in which no line-of-sight exists in the flow direction, and an in-line

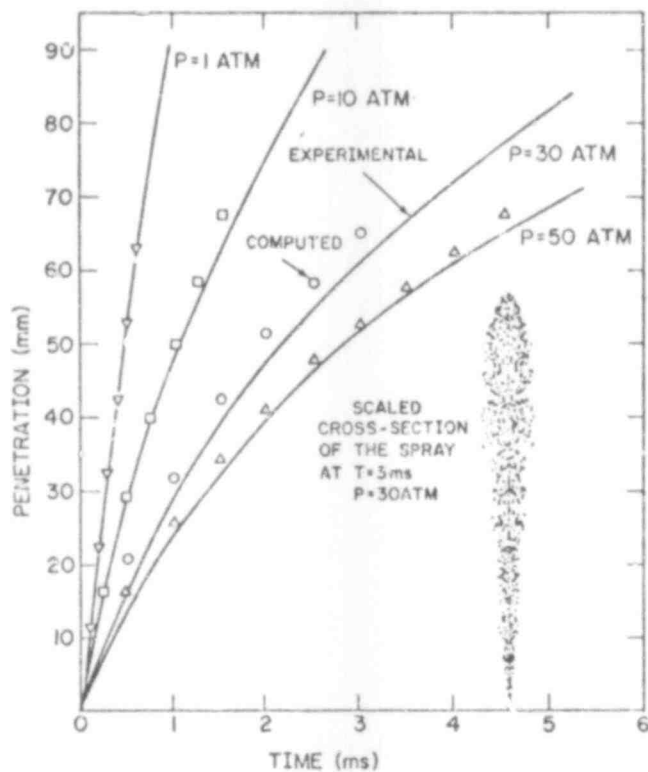


Fig. 71. Spray tip penetration comparison with experiment.

configuration in which the structures are placed in the center of the channel, permitting line-of-sight communication along the channel. The staggered configuration is more typical of present PWR designs.

Figures 72 and 73 show the results for an idealized staggered configuration. In this idealized calculation the droplets are assumed to enter the channel at the left boundary of the mesh with the same velocity as the air stream. The velocity vectors for the air are seen in

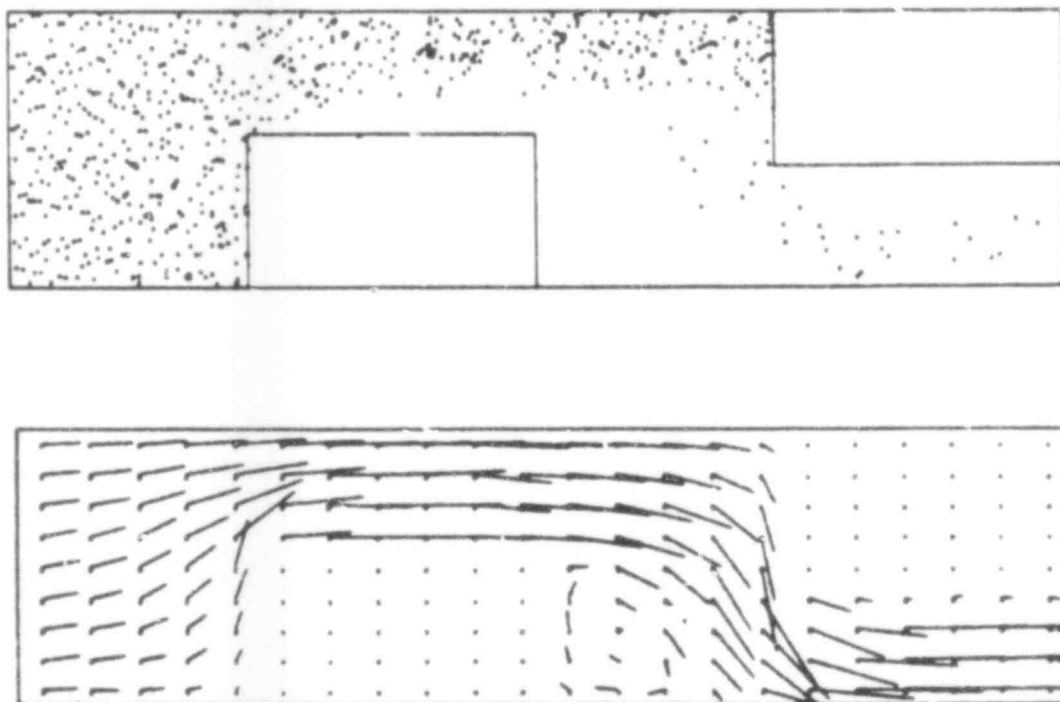


Fig. 72. Particle plots and velocity vectors in the staggered control rod configuration.

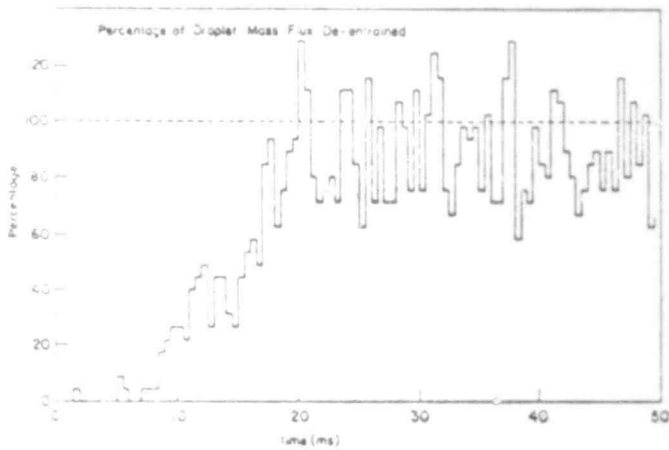


Fig. 73. Percentage of droplet mass flux de-entrainment in the staggered control rod configuration.

the lower portion of Fig. 72. The air accelerates around the control rods and forms a recirculation region in the wake of the first obstacle. Droplets with a spectrum of sizes are introduced. Because of their inertia, droplets cannot follow the velocity changes of the air stream. The large droplets impact the obstacles and are de-entrained. Only the smallest droplets of the spectrum can follow the flow path sufficiently to get through the channel. The upper portion of Fig. 72 shows the particle distribution within the channel after a statistical steady state has been reached. The particles in the downstream end of the channel are all below the lowest quartile of the particle size spectrum. Figure 73 presents the percentage of droplet mass flux de-entrained by the rods as a function of time. The results indicate an efficiency of droplet mass removal of approximately 90% at steady state. Similar calculations were performed for the in-line configuration. These indicated a much less efficient removal of the droplets from the air stream.

Experimental studies along these lines are currently under way at Harwell²⁰ and LASL.²¹ These correspond to air-water systems in simple geometries. We anticipate applying our technique in support of these experiments. Preliminary results from these experiments show the structures to be very effective in removing droplets from the air stream, a conclusion supported by the calculations performed thus far.

D. LWR Experiments

(H. H. Helmick, Q-8)

The objectives of LASL's LWR Safety Experimental Program are to provide experimental support for model development activities and to develop advanced instrumentation techniques. This program is conducted in close coordination with code and model development efforts at LASL and is coordinated with other experimental programs for which advanced instrumentation is required.

During the last quarter, significant accomplishments in the video stereogrammetry development program included the completion of a steam test loop. A heat pipe cooling shroud designed for use with the German PKL rod lens system was shown to be very successful by testing in the steam loop. Using methanol as the heat pipe working fluid, a flat temperature profile at approximately 297 K was obtained. Improvements in video recording with increased signal-to-noise ratio have been accomplished and fabrication of the equipment for synchronization of flash illumination with video framing is under way. Measurements on the upper plenum de-entrainment experiment continued this quarter. Experiments with cylinders of three different diameters were performed. A structural member of square cross section was also studied. A test section is being designed to accommodate up to five rows of prototypical cylinders. De-entrainment was studied for a slab upper plenum section simulation of the proposed Japanese Slab Core Test Facility (SCTF). The flow patterns from this preliminary qualitative study are shown. A new method of numerical analysis of hot-film anemometry data is under investigation. Some tentative conclusions about the results are given.

1. Video Stereogrammetry

(C. R. Mansfield and J. F. Spalding, Q-8)

During this quarter, progress in five areas of work was made in the development of the video stereogrammetry (VS) system. The majority of the equipment has been fabricated, and testing of the system is in progress.

a. Steam Test Loop

A remotely operated steam loop was assembled and is being used for testing of the VS system. This loop can provide 45.5 kg/h (100 lb/h) of saturated steam at 0.689 MPa (110 psi) and superheated steam to 623 K. Noncondensable gas (N_2) can be added to the system. By using additional spool pieces, VS probes of up to 3.5 m in length can be tested. Cold water can be injected into the test section to determine the effects of thermal shock on the VS system. Instrumentation of the loop to monitor pressure and temperature by the PDP-11/34 computer has begun.

b. Video Electronics Development

The stereo video head has been assembled and testing has begun. Stereo video signals have been successfully encoded into a National Television Standards Committee (NTSC) format and recorded. It has been found experimentally that greater resolution can be obtained by also using the green channel of the encoder and using edge enhancement in that channel. The camera head has been modified for this and the NTSC encoder readjusted for maximum resolution. Video imaging of entrainment/de-entrainment experiments have continued using various optical and illumination systems. Final design of all pulsing electronics has been completed and the assembly of the final unit begun. This equipment provides timing for strobe illumination and synchronization with video framing. Video images have been digitized and work is in progress to interface the video digital memory with the PDP-11.

c. VS Probe Development

A VS probe for the PKL Ib experiment is nearing completion. The design of this probe is as general as possible so that future probes can use many identical parts.

d. Heat Pipe Cooling

The operation of the heat pipe cooling system has been tested with the steam test loop. Thermocouples were spaced along the tube which will hold the optical components. The results of this test are shown in Fig. 74.

For this test the VS probe was in steam at 438 K. Coolant water flow to the heat exchanger section was maintained at 297 K.

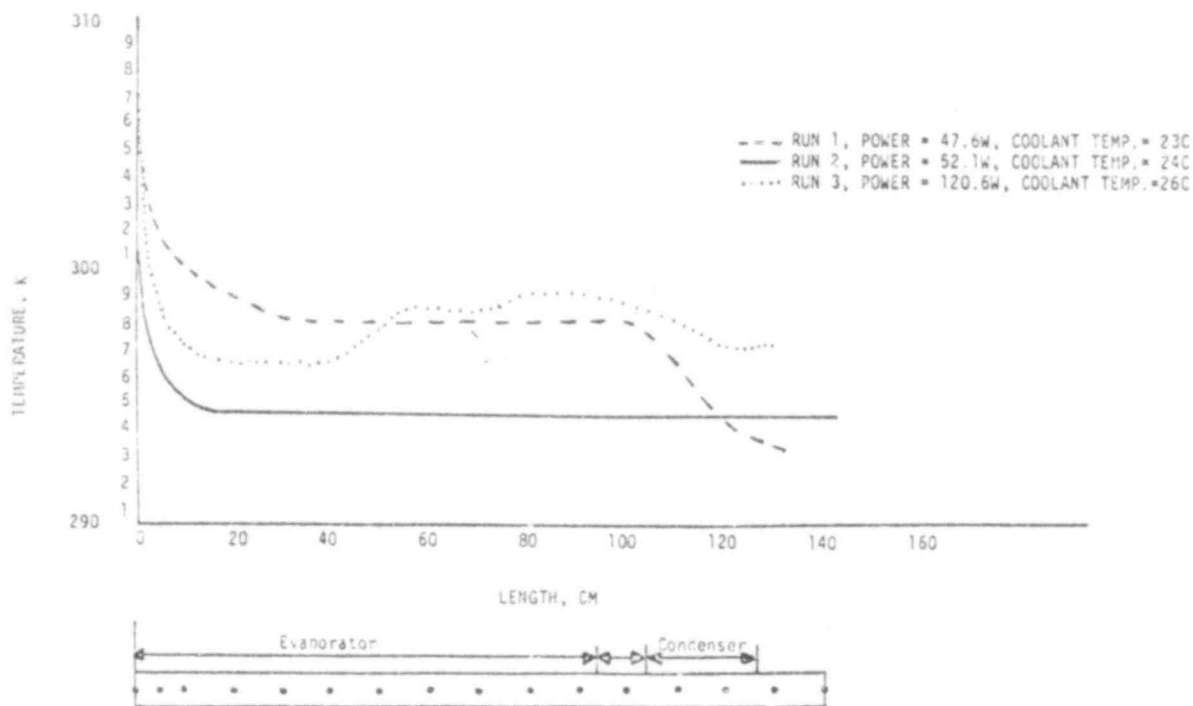


Fig. 74. Performance of PKL stereographic lens system.

During steady-state operation the heat flux through the probe was 52.1 W. As seen in Fig. 74, the temperature of the optical tube was maintained at 297.4 K over most of its length.

e. PKL Adaptor

A vessel penetration adaptor has been designed by the PKL staff. We are fabricating portions of this adaptor which will be attached to the VS probe before shipment to PKL.

2. Upper Plenum De-entrainment Experiment

(V. S. Starkovich, Q-8; and W. L. Kirchner and J. C. Dallman, Q-6)

Initially unsatisfactory droplet spray uniformity led to continued testing and design of spray systems. An array of 25 separately controllable nozzles is now in use. This system provides a good distribution of mass over the cross section of the 560 mm square test section. Using this upgraded system, single pin measurements were performed with improved results. To carry out a wide range

of single pin measurements, 25.4, 63.5, and 101.5 mm right circular cylinders as well as a 76.2 mm square pin (for examination of non-circular reactor internals), have been designed and fabricated.

Using the improved spray system, measurements comparing the single pin de-entrainment efficiencies for 25.4, 63.5, and 101.5 mm right circular cylinders are nearing completion. In addition, these measurements are being compared to those made with the 76.2 mm square pin.

During this quarter, a major modification of the test section was undertaken. This included a test section designed to accommodate a 17-pin "infinite" symmetric array of 101.5 mm circular cylinders. This section will be used to determine the de-entrainment for up to five rows of prototypical cylinders. Additional efforts have included designs for "dry" side ports necessary for the use of laser sizing and velocimetry equipment, for a 101.5 mm cylindrical pin which will be used to study the thickness and distribution of liquid layers which form on the cylinders during de-entrainment, and for a large liquid supply system to be used for conditions of very high liquid flow rate and/or with reduced surface tension liquids.

Diagnostic equipment to be used in this system was also extensively examined. Those examined included automated de-entrainment liquid measurement techniques, droplet sizing and velocimetry techniques, and liquid film thickness and flow rate measurement instrumentation. Of these, only the droplet sizing and velocimetry technique need further investigation.

In addition to the fundamental de-entrainment experiments, a more prototypical simulation experiment was performed. This was a slab upper plenum section simulation of a proposed design for a SCTF to be built in Japan.²² Figure 75 illustrates a top view of the proposed upper plenum design with the simulation overlaid (thicker lines). The objective of this test was to investigate the influence of the walls in the proposed design and compare the results to what is observed in more prototypical upper plenum simulations. The test section was installed in the wind tunnel used for the fundamental de-entrainment experiments. Air and dispersed

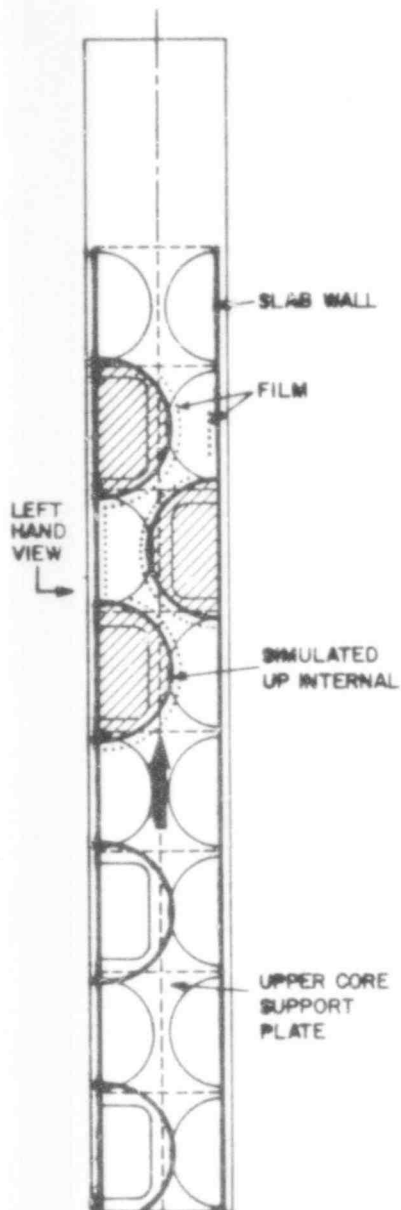


Fig. 75. Slab upper plenum simulation experiment.

water drops were introduced in a cross-flow mode at velocities on the order of 10 m/s. As expected, most liquid was de-entrained from the flow stream since the geometry allowed no line-of-sight path for the drops from entrance to exit. The major conclusion of this preliminary qualitative study was that the presence of the walls modifies the film drainage patterns as compared to more prototypical configurations (e.g., an "infinite" rod bundle). The film locations are shown in Fig. 75. Figure 76 illustrates photographically the flow field as seen through the left-hand side (LHS) of the plexiglas test section. In the absence of walls, more liquid would collect on the rods and therefore drain at locations closer to the exit (outer periphery of the core). Further investigation is warranted for possible design alterations which would yield more prototypical flow patterns.

3. Hot-film Anemometer

(P. F. Bird, Q-8)

Based on the formalism described by Underwood,²³ it is possible to relate a distribution of relative lineal measurements to particle size distributions and also to relate the ratio of the integral of lineal measurements of a test line length directly to the relative volume of particles present. These observations are being implemented

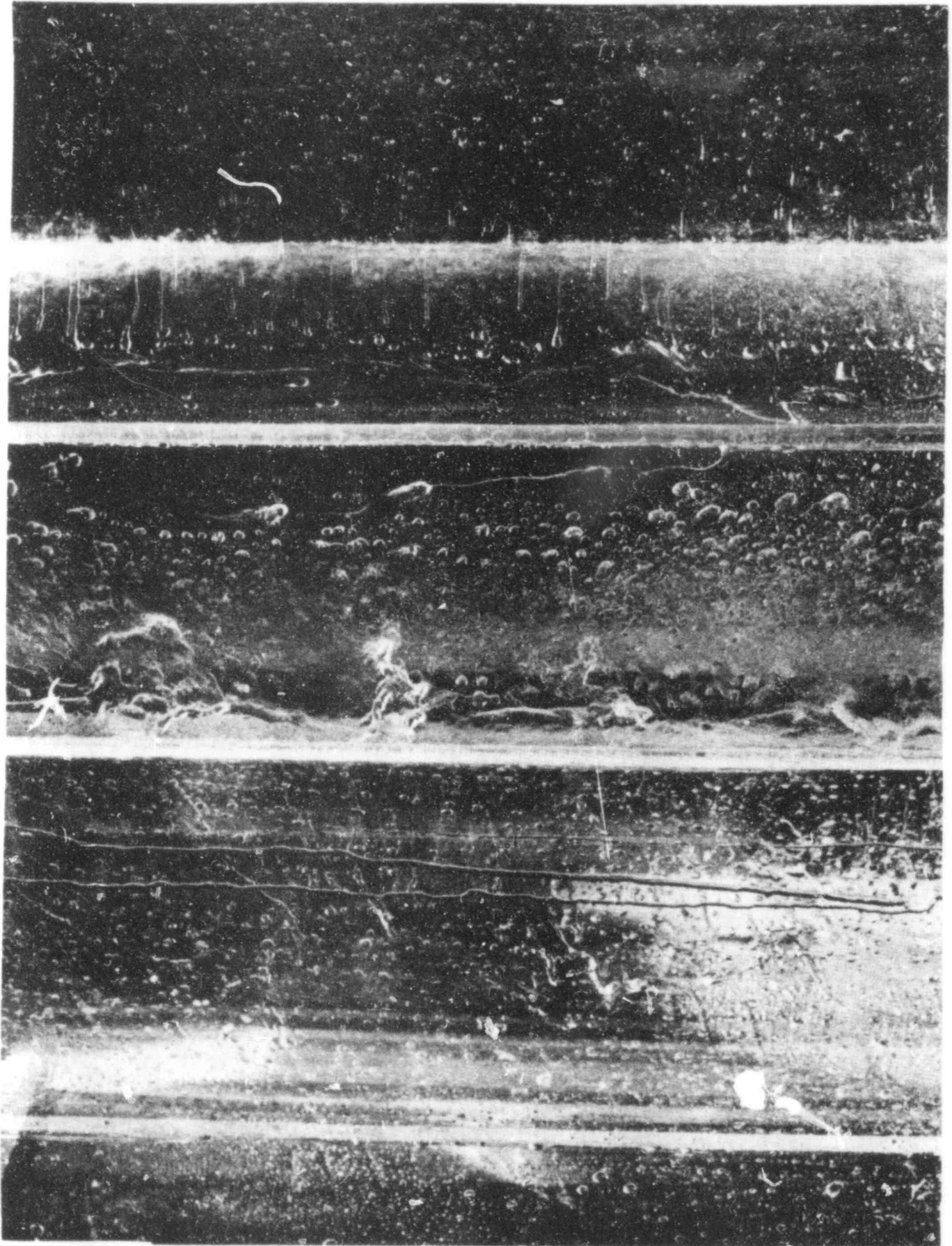


Fig. 76. Droplet cross flow in slab upper plenum simulator (10 m/s and 3.8 kg/m).

with a hot-film anemometer serving as an edge detector and velocity measuring device for water droplets.

Using the hot-film anemometer as an edge detector and with appropriate electronics, we have recorded transit time distributions of water droplets over the hot-film anemometer for a number of experimental conditions. We have deconvolved some of the distributions to arrive at equivalent transit times through the diameter of the water droplets assuming they are spheres. Conversion from equivalent diametral transit times to particle size distributions depends on an accurate measurement of the velocity distribution. The accurate measurement of the velocity distribution of water droplets is being investigated.

The following observations are made.

1. For transit times which are long enough not to be affected by the physical size and frequency response of the hot-film anemometer, well defined diametral transit time distributions are obtained.
2. The shape of these distributions are consistent with droplet size distributions obtained from the laser sizing system developed and demonstrated by Spectron Development Laboratories.
3. Some questions have arisen regarding our ability to measure average droplet velocities, a measurement essential to reducing the diametral transit time distributions to droplet size distributions. These questions are being investigated.

4. Data Acquisition System

(P. F. Bird, Q-8)

Acquisition and analog playback of video frames have been demonstrated using our CAMAC-based video digitizer under PDP-11/34 computer control. Recording of simulated data on magnetic tape in a format suitable for data reduction in the LASL Central Computing Facility (CCF) has been demonstrated.

III. LMFBR SAFETY RESEARCH

(M. G. Stevenson, Q-DO; and J. E. Boudreau, Q-7)

The Liquid Metal Fast Breeder Reactor (LMFBR) safety research effort at LASL consists of several programs. In the first of these, the SIMMER code is being developed and applied to core disruptive accident (CDA) analysis with support from the Division of Reactor Safety Research (RSR) of NRC. SIMMER is a two-dimensional, coupled neutronics-fluid dynamics code intended for transition phase, core disassembly, and extended fuel motion analysis. The second version of the code, SIMMER-II, has been completed and is now being used in the analysis of CDA problems.

In a separate, but closely related, program funded by the U.S. Department of Energy (DOE), models are being developed for phenomena important to the progression and consequences of CDAs. Some of this work is basic research on phenomena, but in most cases the developed models will be included directly in accident analysis codes and, particularly, in SIMMER. Another part of this DOE program is focused on the application of the accident codes, particularly the SIMMER code, to the study of specific aspects of accident sequences. The work in the SIMMER model development, code development, and code application areas is reported in Sec. III.A.

Experimental investigation, including confirmation of reactor safety analysis methods, is an important part of safety research. Section III.B provides a summary of recent work involving out-of-pile experiments and related analysis in support of SIMMER model development and verification.

Finally, Sec. III.C reports recent work in the LASL LMFBR Safety Test Facility (STF) study, a program funded by NRC/RSR.

A. SIMMER Code Development and Applications

(L. L. Smith and C. R. Bell, Q-7)

The sensitivity analysis of the voided core postdisassembly expansion study²⁴ was completed. For this particular case it was determined that the primary contributor to the variation in the

maximum system kinetic energy was the assumed uncertainty in the relationship between the fuel vapor pressure and the fuel temperature. This effect on the kinetic energy is overestimated because the same vapor pressure variation in the disassembly phase would tend to compensate for the subsequent postdisassembly effect.

The whole-core transition phase analysis presented in the last report¹⁴ indicated reactivity effects initiated by the interaction of hot core material with sodium in the lower axial blanket region of the reactor. The SIMMER-II modeling of this process is uncertain and has not been supported by experiment analysis. To provide some insight into this and other modeling in SIMMER-II, an analysis of TREAT test R-7 was performed. In general, the comparison of calculated and experimental results discussed in a following section is encouraging.

Finally, a technique was developed to optimize the isotopic composition for the two-fuel (fissile and fertile) treatment currently used in SIMMER-II. Thus, the fuel in core regions with isotopic compositions different from those assigned to the two input base compositions will have minimal errors in macroscopic cross sections.

1. Application of Statistical Correlation Methods to the Sensitivity Analysis of SIMMER-II Input Parameters

(R. D. Burns, III, Q-7)

A previous SIMMER-I²⁵ calculation by Bell and Boudreau²⁴ of voided core postdisassembly energetics in the Clinch River Breeder Reactor (CRBR) gave a system kinetic energy of 3 MJ at the time of sodium pool impact with the reactor head. This result was significantly different from the 100 MJ result for a conservative isentropic expansion of a two-phase mixture of fuel, with an initial average temperature of 4 800 K, to the cover gas volume (21 m³). More sophisticated calculations of the same expansion problem were performed with SIMMER-II,²⁶ and modeling sensitivities were explored. The results of this sensitivity study and the analysis method used are summarized here.

The possibility of performing sensitivity analyses with SIMMER was first considered when work with large water reactor safety codes²⁷ showed that useful information could be obtained from a relatively small number of code calculations. To gain experience with the sensitivity analysis approach, a simplified study of postdisassembly expansion energetics was performed with SIMMER-I, and the results have been reported.²⁸ The methods have since been revised,¹⁴ and also applied to experiment analysis.²⁹ This report provides comprehensive information about the relative sensitivity of postdisassembly expansion energetics results to modeling assumptions in SIMMER-II.

The base calculation for the sensitivity study and the selection of the parameter uncertainties were discussed in an earlier report.³⁰ The study used 15 SIMMER-II calculations in which 25 input parameters were independently and simultaneously varied. The results of the study can be summarized as follows.

1. The observed variation in system kinetic energy at pool impact with the reactor head is primarily the result of the assumed uncertainty in the fuel vapor pressure. This variation does not account for a countereffect in the disassembly phase which would cause fuel vapor pressures to develop earlier and thus limit the disassembly energetics.
2. The sensitivity of the expansion to the detailed modeling of the exchange processes is small for the voided core problem.
3. Interactive mitigating effects dominate the expansion even when large variations in their magnitudes are included.
4. Accident conditions prior to the postdisassembly expansion phase are likely to be more important in determining the magnitude of the maximum energetics than uncertainties in SIMMER-II modeling.

These conclusions are valid only in the context of the current SIMMER-II modeling, and the sensitivity to models not included in SIMMER-II [e.g., triggered fuel coolant interaction (FCI)] is difficult to evaluate without specifically modeling the processes.

The output quantities used in this study as indicators of accident energetics include maximum system kinetic energy, head impulse, and maximum pressures calculated at key locations within the reactor vessel. The "maximum values" are the largest observed in the time history of individual calculations. Other output values for the 15 SIMMER-II runs are reported elsewhere.¹⁴ In these 15 runs, the kinetic energy varied a factor of 8 from minimum to maximum (2.5-20 MJ). None of the other output parameters noted above varied by more than this factor. Table XI summarizes the variations of the output quantities for the 15 runs.

The objective of the sensitivity analysis was to discover which, if any, of the input parameter variations correlated well with the variation observed in system kinetic energy and thus indicate to which modeling uncertainties the SIMMER-II results are most sensitive. However, the conclusions resulting from this analysis are constrained by the sizes of the 25 input variations, the version of SIMMER used, and the particular problem description.²⁶ The conclusions are also dependent on the probability distributions selected for each input variation and the fact that there are 25 independent variations, because this information determines the likelihood of selecting certain combinations of input parameter variations in the 15 runs. For example, the selection of an input set with the worst-case (i.e., most conservative) value for each of the 25 input parameters is highly unlikely.

The procedure used is to calculate a correlation coefficient between kinetic energy and each of the 25 input variations. Then the best correlated input among the 25 is tested for significance of the correlation. That is, the magnitude of the correlation coefficient is tested to determine whether the apparent correlation could be simply a chance configuration of random noise. Note that there is a finite probability of observing an apparent correlation between two entirely independent sequences.

Various correlation methods are available. The most commonly used in engineering applications are linear, exponential, logarithmic, and power regressions. With these methods, the analyst determines how well the data conforms to the functional form being

TABLE XI
SUMMARY OF RESULTS OF 15 SIMMER-II CALCULATIONS

Statistical Quantity	Max. KE (MJ)	Impulse to Head (MNs)	Max. Press. at Head (MPa)	Max. Avg. Press. at Head (MPa)	Core Press. at Impact (MPa)	Peak FCI Zone Press. ^a (MPa)	Avg. FCI Zone Press. (MPa)	Time of ot Peak Press. ^a (MPa)	Time of Impact (s)
Average	8.30	1.04	5.64	3.27	1.39	2.08	1.56	0.08	0.24
Std. Dev.	4.50	0.32	1.35	1.03	0.68	1.03	0.77	0.03	0.07
Maximum	20.57	1.79	8.70	5.74	3.08	5.09	3.60	0.13	0.41
Minimum	2.52	0.57	2.72	1.73	0.76	0.80	0.62	0.03	0.14
Key Input Sensitivity	P_1^*	P_1^*	P_1^*	P_1^*	P_1^*	P_1^*	P_1^*	P_1^*	P_1^*
S-Score	61	59	51	57	77	49	51	-49	-41
Confidence in Correlation	97%	96%	85%	94%	99%	82%	86%	82%	78%

^aFirst peak.

tested. None of these methods are suitable for the present analysis because they are all specifically related to functional forms. Rather than discovering the functional forms of input-output relationships, the purpose in the present analysis is simply to find monotonic relationships, regardless of functional form.

A correlation method that tests only for monotonicity is the Kendall's tau method.^{31,32} The procedure is to look for like patterns of variation between two sequences of numbers, for example, (x_1, \dots, x_n) and (y_1, \dots, y_n) . The x sequence could represent the values of an input parameter used in n different runs, and the y sequence could represent the corresponding values of an output quantity. This basically involves comparing each possible pair of values in the first sequence (e.g., x_2, x_5) with its corresponding pair in the second sequence (y_2, y_5), scoring +1 if the first member of each pair is smaller (or larger) than the second in each pair ($x_2 > x_5$ and $y_2 > y_5$, or $x_2 < x_5$ and $y_2 < y_5$), and scoring -1 otherwise ($x_2 > x_5$ and $y_2 < y_5$, or $x_2 < x_5$ and $y_2 > y_5$). These are referred to as positive and negative scores, respectively. For sequences of length n there are $n(n-1)/2$ possible pair combinations, and the total score S can be between $-n(n-1)/2$ and $n(n-1)/2$. Hence, the Kendall's tau is defined:

$$\tau = \frac{S}{n(n-1)/2} .$$

For perfectly positively correlated sequences the tau value is +1, and for perfectly negatively correlated sequences it is -1. This is consistent with the more common correlation methods. Values of tau between these two extremes indicate less than perfect correlation, and values around zero indicate randomness, i.e., no correlation.

The best correlation of input value sequence with the output kinetic energy sequence is with PSTAR(1), or p_1^* , a parameter in the fuel vapor pressure equation relating vapor pressure to saturation temperature.²⁵ The S score for this correlation is 61, counting ties as -1 ($\tau = 61/105 = 0.58$). The significance of S

scores can be determined from statistical tables.^{31,32} The probability of selecting two independent sequences of length 15 at random and obtaining $S \geq 61$ is found in the tables to be only 0.0014, indicating that the apparent correlation is probably not random noise. The significance of the $S = 61$ score can be further re-evaluated as follows.

The probability that any one of the 25 correlations has an S score less than 61 is $1 - 0.0014$, or 0.9986, if the sequences are truly random and independent of the output sequence of kinetic energy values. The probability that all 25 S scores are less than 61 is then 0.9986^{25} , or 0.97. Hence, the probability that the best correlated of the 25 correlations has $S \geq 61$ is $1 - 0.97$, or 0.03. This 3% probability translates to 97% confidence in the rejection of the claim that kinetic energy and p_1^* are not correlated.

This result warrants further qualitative discussion. As previously stated, tau values of unity indicate perfect monotonic correlation; hence, the value of 0.58 for the S score of 61 indicates positive, although less than perfect, correlation. Lesser sensitivities of the kinetic energy to other input variations still show up as noise, because the p_1^* sensitivity is not sufficiently strong to completely dominate the results. This is apparent in the scatter in Fig. 77, which shows the general trend of the p_1^* -kinetic energy relationship and illustrates the degree of noise due to lesser sensitivities to the other 24 input variations.

It can be seen from Fig. 77 that the correlation depends on the size of the p_1^* variation. If the range of variation of p_1^* were smaller than 0.5 to 4 times nominal, the size of the bandwidth for the random noise (i.e., the degree of vertical deviation of the scattered points in Fig. 77 from a common, monotonic curve) could become larger than the p_1^* variation, and the correlation would no longer be apparent. Further, if the size of other input variations were increased, this could increase the noise bandwidth and mask out the apparent p_1^* correlation. It is interesting that, while the p_1^*

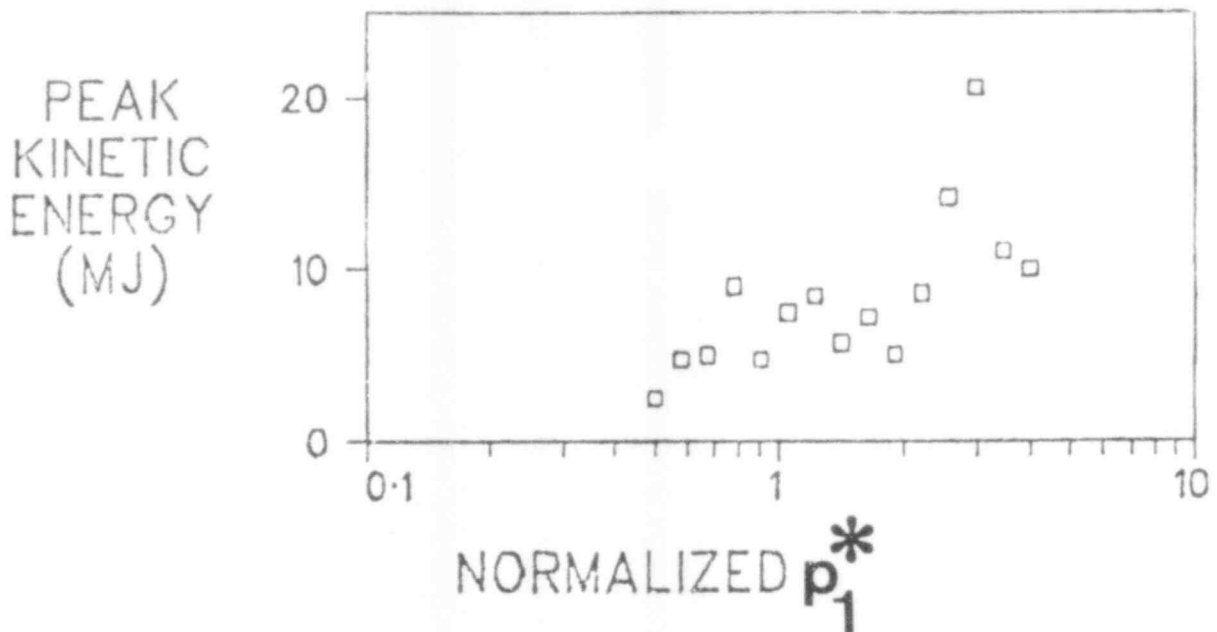


Fig. 77. Scattergram of p_1^* and kinetic energy.

correlation is fairly strong on a statistical basis, visually the correlation is not so obvious, as can be seen in Fig. 77.

To determine the impact on the sensitivity analysis of decreasing the range of the p_1^* variation to 0.5 to about 2 times nominal, the results of 11 runs in which p_1^* was less than 2.2 times nominal were examined. This reduced the number of possible pair combinations to $11(11-1)/2$, or 55.

The best S scores were found for two of the 25 correlations -- the multicomponent stratification parameter α_2 , which describes the preference for either liquid fuel or liquid steel to transfer heat to the flow channel wall when both liquids are flowing together, and the liquid fuel-to-liquid steel heat transfer multiplier, $RLL(1,2)$.²⁶ The S scores for these were +25 and -25, respectively. The confidence that each correlation is not coincidence is 97.5% when considered individually, but only 53% when considered as the best of 25 possible correlations (i.e., $0.975^{25} = 0.53$). Hence, no single input variation was found to dominate the kinetic energy in the low p_1^* region (i.e., low kinetic energy).

However, for those pairs wherein α_2 increased from the first run to the second run and $RLL(1,2)$ decreased, the kinetic energy was observed to increase from the first run to the second in 33 of

the remaining 40 pairs. The confidence in the correlation of α_2 and RLL(1,2) with kinetic energy is 99.7%. S scores cannot be determined for multiple correlations using available tables. The confidence was determined by calculating S scores for comparing α_2 and RLL(1,2) with 1 285 other sequences chosen at random. Only three of these had higher S scores than the correlation with kinetic energy.

For those pairs wherein α_2 increased, RLL(1,2) decreased, and the liquid fuel-to-liquid sodium heat transfer multiplier, RLL(1,3)²⁶ decreased, the kinetic energy was observed to increase in 20 of the remaining 21 pairs. The confidence in this correlation is greater than 99.5%. [None of the S scores for comparing α_2 , RLL(1,2), and RLL(1,3) with 1 285 random sequences equaled or exceeded 20.]

Large α_2 implies decreased liquid fuel-to-structure heat transfer (stratification favors liquid steel, rather than liquid fuel, in contact with structure), and small RLL(1,2) and RLL(1,3) imply similarly decreased heat transfer from the fuel. Further, large α_2 , small RLL(1,2), and small RLL(1,3) correlate with higher system kinetic energy. Therefore, it appears that if heat is removed from liquid fuel more slowly, then the kinetic energy is higher. This is the main statistical sensitivity at low energies and certainly is in accord with intuition.

The situation is different at higher energies, however. For this analysis, only those runs with p_1^* values from about 2-4 times nominal were considered. There are 6 runs with p_1^* greater than 1.9 times nominal, reducing the number of possible pair combinations to $6(6-1)/2$ or 15. The droplet size distribution multiplier (DSDM) (which produces a shift in the single droplet size used to represent the distribution) was found to be the best correlated input variation for high p_1^* values (high kinetic energy), with an S score of 11. The confidence in the correlation is 99%, when considered as a single correlation, but is only 78% when considered as the best of 25 correlations ($0.99^{25} = 0.78$).

Since large DSDM implies larger droplet sizes, the coalescence multiplier, COAL (which controls the rate at which coalescence occurs), was considered in further analysis. It was found that in nine pairs, both DSDM and COAL increased. In each of these,

kinetic energy also increased. The confidence in this correlation is greater than 99%. (Only one of the S scores for comparing DSDM and COAL with 1 285 random sequences was as large as 9.)

Large DSDM and COAL imply larger droplet sizes. These imply slower momentum exchange (i.e., less coupling of fields in two-phase flow) and slower heat transfer. Since heat transfer rates were already determined not to impact sensitivities at high energies, it is apparent that kinetic energy is sensitive to momentum exchange rate, since slower rates yield higher energy.

Now, we can determine the probability that some combination of the variation in the 25 input parameters would have given a kinetic energy greater than the 20 MJ observed in the 15 runs. The selection of the input parameter values was random as was previously described; therefore, assume that there is a probability P that the energy will be less than or equal to 20 MJ in any given SIMMER-II run. Thus, the probability that the energy would not have exceeded 20 MJ in the 15 runs is P^{15} . This is used to determine how large P must be in order for there to have been a probability of 0.5 of exceeding 20 MJ in 15 runs and a 0.5 probability of not.

$$0.5 = P^{15} \text{ or } P = 0.95.$$

Therefore, the best estimate is that there is only a 5% chance of exceeding 20 MJ in another run.

A more conservative estimate is obtained by finding how large P must be for it to have been unlikely not to have exceeded 20 MJ in 15 runs. "Unlikely" is quantified as a 5% chance (which translates to 95% statistical confidence in the result). Thus,

$$0.05 = P_{\text{cons}}^{15} \quad \text{or} \quad P_{\text{cons}} = 0.82,$$

and the conservative estimate is that there could be as high as an 18% chance of exceeding 20 MJ in another run.

2. SIMMER-II Analysis of the R-7 TREAT Test

(W. R. Bohl, Q-7)

The R-7 TREAT loss-of-flow experiment³³ was a seven-pin simulation of thermal and hydraulic accident conditions such as might develop in the central channels of a high power-to-flow subassembly in a loss-of-flow accident (LOFA) in the Fast Test Reactor (FTR) beginning-of-life (BOL) core. The test scenario included four stages:

1. induced undercooling,
2. coolant boiling and voiding,
3. relocation of molten cladding, and
4. fuel melting and subsequent fuel motion.

For SIMMER verification purposes, the R-7 test appears to be the most useful of the R-Series experiments due to the existence of a power pulse timed to coincide with the onset of fuel slumping.

SIMMER-II has some attractive features for undertaking this analysis in that it can treat consistently the interconnected channel effects as they influence all four accident stages. Coupled with this multipin capability, SIMMER-II can also represent the large radial heat sink in the experiment, the area change effects at the test section inlet and outlet, and the inertial and frictional characteristics of the R-Series apparatus.

The set-up of the SIMMER-II input for the R-7 test geometry used a two-dimensional 3 x 45 node mesh. In the test section region, the inner coolant channel, the surrounding pin surfaces, and the spacer wires were represented by the first radial node. The outer coolant channel, associated pin surfaces, spacer wires, extra filler wires, and the hexcan were represented by radial node two. The third radial node simulated the molybdenum heat sink and the space outside the hexcan, which was available for material relocation following hexcan failure. Axially, the SIMMER representation used:

- a. 10 nodes of unequal length below the test section,
- b. 25 nodes in the Inconel reflector and fuel pellet region,
- c. 4 nodes in the fission gas plenum, and
- d. 6 nodes above the test section.

Spatial and temporal power shapes, as well as inlet and outlet pressures, were transcribed from the available reports.^{33,34} In general, the nominal SIMMER-II code was used, except where modifications were required to better simulate the unique features of this test or to correct or bypass specific calculational problems with the SIMMER-II models.

A reasonable representation of the preboiling temperature profile development was achieved with SIMMER-II. Boiling initiation was within 0.2 s of the experimental result. The can wall temperature in the experiment at a point 254 mm (1 in.) above the top of the heated zone was measured to be 1 105 K (1 530°F) at the time of boiling initiation. The calculated value was 1 118 K.

The calculational details of the voiding process are interesting; however, it is difficult to compare to the experiment such features as the degree of upstream voiding in the central channel and flow diversion to the periphery. Flow reversal is calculated at 0.8 s after boiling initiation, as was measured. Beyond this point, the flow meter trace does not possess the fine structure or the same frequency of oscillation as does the calculation. The explanation for the discrepancies is not obvious. Nevertheless, the calculated voiding profile development is similar to the experiment and seems to depend mainly on the heat capacity effects of the large structures which are present, as can be inferred from the model of Grohmes.³⁵

There are no data available on the details of cladding relocation. The calculated results not only depend significantly on sodium chugging phenomenology, but also on the lack of a model in SIMMER-II for the flooding phenomenon and subsequent augmentation of liquid-vapor frictional coupling. The general motion of molten cladding is calculated to be downward until the additional steel

and vapor provided by can wall melting and failure produce upward motion and plugging. It can be noted that the final SIMMER pre-burst result of a complete blockage in the outer channel and a partial blockage in the central channel has also been obtained by Ishii³⁶ using a different multichannel model. Nevertheless, this result could still be incorrect and data are not available to check this result.

The assumed 0.5 fuel melt fraction for motion initiation causes fuel motion to begin slightly before the burst. Initially, the calculated fuel motion is slow because most of the unmelted fuel is assumed to remain in the structure field. The motion does have a predominantly downward characteristic, which agrees with the preliminary hodoscope analysis reported.³³ A mild eructation due to fuel and steel vaporization is calculated beginning at 22.06 s as the power is decreasing. Some similar event may well have occurred in the test based on the results obtained in the posttest examination. Following the burst, the calculated configuration develops into an upper blockage consisting mainly of steel (with some fuel) and a massive lower blockage starting in the highest node of the lower Inconel reflector.

Table XII shows a summary comparison of the experimental and calculational timing. The agreement with experiment is quite respectable in some aspects. Where agreement is less satisfactory it is still possible to obtain interesting insights from the comparison and suggest ways to improve SIMMER models. The experiment appears to be largely controlled by quasisteady-state phenomenology; consequently, the complete compressible hydrodynamics treatment of SIMMER is somewhat inefficient. However, the intimate coupling with the neutronic feedbacks of an LMFBR accident requires such a transient treatment, and the eventual completely successful calculation of such experiments by such methods should be feasible and may be required, for code validation.

TABLE XII
TIMING OF SIGNIFICANT EVENTS FOR TREAT TEST R-7

<u>Event</u>	<u>TREAT Time, s</u>	<u>SIMMER Time, s</u>	<u>Notes</u>
Reactor Power Up	3.5	3.5	
Start of Flow Coastdown	8.38	8.38	
Local Boiling	14.6	14.4	
Inlet Flow Reversal	15.4	15.2	
Upper Cladding Blockage	18.2	19.7	SIMMER does not model the flooding phenomenon
Flow-tube Failure	19.11	19.44	SIMMER requires melting of the can wall before failure
Onset of Fuel Motion	21.6	21.4	
Reactor Power Pulse Begins	21.6	21.6	
Lower Cladding Blockage	22.0	22.0	
Mild Eruption of Molten Material	--	22.06	Final hodoscope results are not yet known.
Power Termination	22.16	22.2	

3. Minimizing Errors in the Fertile/Fissile Fuel Model in SIMMER-II

(R. G. Steinke, Q-7)

SIMMER-II models the different fuel isotopic compositions throughout the reactor with two fuel mixtures, fertile and fissile. Errors are introduced when the actual isotopic percentages are approximated by the percentages assigned to each fuel type. In the past, the practice has been to assign all uranium isotopes to the fertile fuel type and all plutonium isotopes to the fissile fuel type. This practice produces a significant error in reactors having fuel in advanced burnup states.

This error could be eliminated by increasing the number of fuel types or components in SIMMER-II to equal the number of

different fuel isotopes or fuel compositions. This possibility becomes unattractive when considering the increased computational effort of more density components and the required reprogramming effort. A better choice at the present time is the approach of minimizing the errors introduced by the existing two-fuel model. This involves only input changes and no direct changes to SIMMER-II.

SIMMER-II users can minimize the mass error in the two-fuel model by generalizing the past approach in two ways. First, allow all fuel isotopes to be present potentially in each fuel type. Second, partition the mass of each isotope between the two fuel types such that the overall mass error

$$E = \sum_i^I w_i^I \sum_j^J w_j^J \left[(R_{1i} \left\{ \sum_\ell^I I_{\ell j} \right\} - I_{ij})^2 + \left(R_{2i} \left\{ \sum_\ell^I (I_{\ell j}^{\text{total}} - I_{\ell j}) \right\} - (I_{ij}^{\text{total}} - I_{ij}) \right)^2 \right], \quad (8)$$

is minimized. Here, I is the number of different fuel isotopes; J is the number of different fuel compositions; w_i^I and w_j^J are constant weighting factors for the relative importance of minimizing the mass error associated with isotope i and composition j ; R_{mi} is the mass fraction of fuel isotope i assigned to fuel type m ($m = 1, 2$); and I_{ij} is the mass of fuel isotope i in fuel composition j that is to be assigned to the first fuel type. This is a least squares minimization procedure where R_{mi} and I_{ij} are the free parameters whose values are to be determined for a best fit. A program called ISOMASS has been written to perform this evaluation and to provide R_{mi} for input to the neutronics of SIMMER-II.

Applying this procedure to the CRBR initial and equilibrium cores removed 70-90% of the mass error associated with the past approach. The infinite medium reactivity for each core type had a similar level of error reduction. The fractional error in a weighted average estimate of the reactivity was reduced from

0.06% to 0.01% for the initial core, 0.6% to 0.2% for the beginning of equilibrium cycle core, and 1.0% to 0.1% for the end of equilibrium cycle core. While the initial core error is negligible, equilibrium core errors of 0.6 and 1.0% are significant. They can be reduced to an acceptable level by using the proposed procedure.

B. SIMMER Verification

(J. H. Scott, Q-7; and H. H. Helmick, Q-8)

Analyses of the bubble expansion experiments performed by Stanford Research Institute (SRI) International have continued with the SIMMER-II code. These analyses have indicated that the nonisentropic effects in the absence of core structure are due to pressure and density gradients within the gas bubble. Although SIMMER-II calculations of the local pressures in the experiments have been greater than the experimental values, additional structure has the same effect on both the experimental and calculated results.

Simulant materials and a preliminary design have been chosen for the upper core structure simulation experiments. This experiment series will provide data for assessing the SIMMER-II modeling of two-phase fuel ejection through the above-core structure following core disassembly.

1. Analysis of SRI International Expansion Experiments

(P. E. Rexroth and A. J. Suo-Anttila, Q-7)

In the SRI International bubble expansion experiments, as described in the previous quarterly report,¹⁴ a source gas (either pressurized nitrogen or flashing water) is allowed to expand into a vessel of room temperature water. The covered vessel, a transparent 1/30-scale model of the CRBR, is shown schematically in Fig. 78. The dynamics of the expansion and the impact of the water on the vessel head is monitored by pressure gages in the lower core and the upper plenum, a water surface gage protruding from the cover, and high-speed photography. The general behavior of the expansion and the effects of the simulated upper core structure

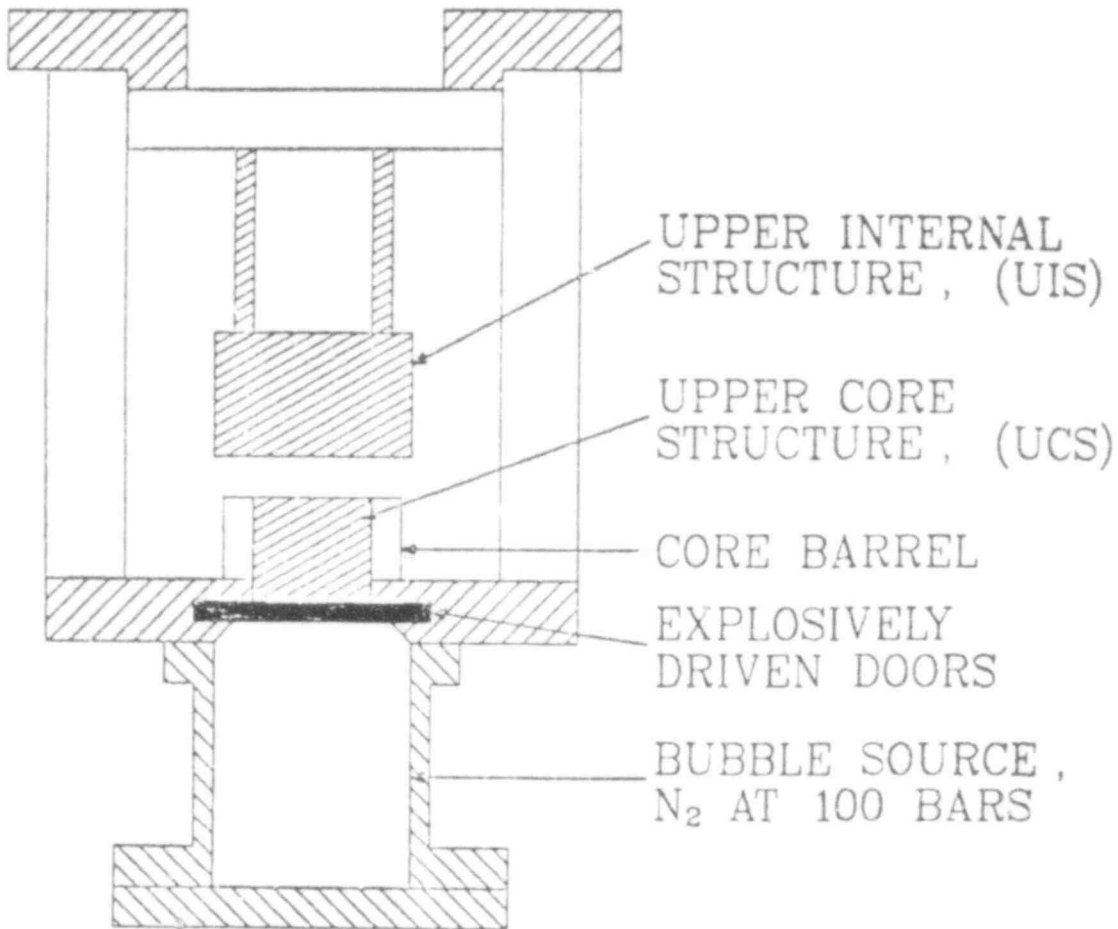


Fig. 78. SRI International experimental apparatus.

(UCS) and flow-guide tube upper internal structures (UIS) on the fluid kinetic energy at vessel head impact are being investigated. Four geometric configurations were run as follows:

1. with no structure other than the core barrel,
2. with the UCS,
3. with the UIS, and
4. with both UCS and UIS.

The following important conclusions were drawn from the experiment.

1. Even with no structure present, the kinetic energy of the liquid slug at impact was considerably less than that predicted from an isentropic expansion of the gas.

2. Presence of either the UCS or UIS or of both delays the time of slug impact and diminishes the kinetic energy and peak pressure of the impact.
3. The UIS is more effective than the UCS in degrading the impact energy.

Analysis of these experiments focused on three goals:

1. To determine if SIMMER could adequately simulate the hydrodynamic behavior observed in the experiment,
2. To determine what effects contribute to the degradation in impact kinetic energy, and
3. To determine whether or not similar effects would be calculated for the full-scale case.

The results of SIMMER simulations of the four experimental configurations showed generally good agreement with the observed results. Table XIII summarizes some of those results and compares them with experimental observations. The impact times are reproduced reasonably well, particularly for tests D-006, D-003, and D-004. Although calculated impact pressures are greater than those observed experimentally, their values relative to the no structure case are in reasonably good agreement. It is believed that the lower pressures observed in the experiments are due, at least in part, to elasticity in the real vessel as compared to the absolute rigidity of the vessel in the SIMMER calculations.

Kinetic energy of the impacting slug is not presented for the experiment because it is not a directly measurable quantity. Instead, water surface locations vs time, as obtained from the water level gage, are compared in Fig. 79 with those calculated for the no structure and for the UCS and UIS cases. Again, reasonable agreement was obtained. It is our conclusion that SIMMER simulates the overall fluid dynamics of the test fairly well.

An analysis of the partition of energy in the SRI International experiments was performed to explain why the kinetic energy in the water slug falls short of the theoretical isentropic kinetic energy limit. In addition to the SRI International D-006 experiment, two other cases were analyzed to show how these effects can be reduced.

TABLE XIII
ANALYTICAL VS EXPERIMENTAL RESULTS FOR THE
SRI INTERNATIONAL BUBBLE EXPANSION EXPERIMENTS

Test Number	Structure Present	Impact Time (ms)	Impact Pressure (bars)	Impact Kinetic Energy (kJ)
D-006	None	3.5 (3.4)	434 (338)	2.38
D-003	UCS	3.9 (3.8)	340 (269)	1.82
D-005	UIS	4.1 (3.9)	320 (165)	1.81
D-004	UIS and UCS	4.6 (4.1)	246 (159)	1.07

Note: Figures in parentheses are experimental values.

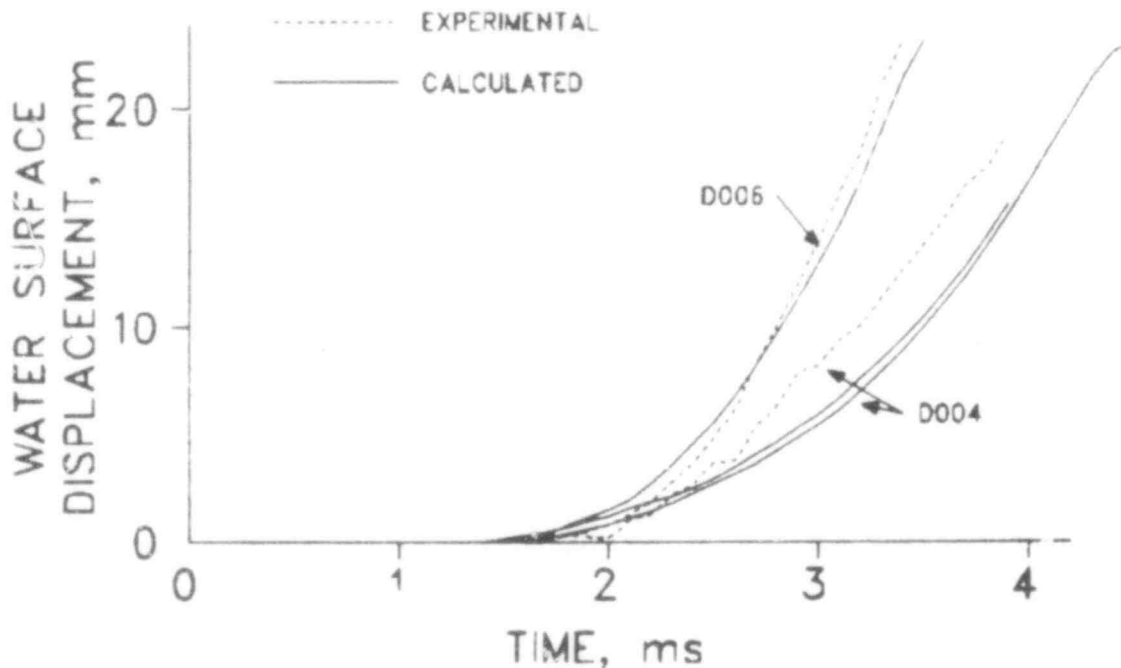


Fig. 79. Water surface displacement vs time for Experiments S-006 (no structure) and D-004 (UCS and UIS).

If the expansion were purely isentropic, then the work and kinetic energy of the slug could be calculated from the first and second laws of thermodynamics. The high-pressure gas in the core does work on the water slug, which, in turn, does compression work on the cover gas. The point of maximum kinetic energy occurs when the depressurized core pressure equals the compressed cover gas pressure. Thus, the kinetic energy of the slug is equal to the work done by the core on the slug less the work done by the slug in compressing the cover gas.

The results for a purely isentropic expansion are:

Work done by the core	4 076	J
Work done in compressing the cover gas	371	J
Net maximum kinetic energy	3 705	J
Initial core pressure	1.0	MPa
Final core and cover gas pressure	4.14	MPa
Final core temperature	243	K

The results of the SIMMER calculations are shown in Table XIV for a variety of cases. The standard SRI International case is equivalent to the SRI International D-006 case of Table XIII. The slight differences are due to the different initial conditions (i.e., no shutter doors in the calculation). As can be seen, only 77% of the maximum kinetic energy is developed (vapor plus liquid). The liquid slug only develops 65% of the maximum isentropic kinetic energy.

The nonisentropic effects are due primarily to pressure gradients in the expanding core gas and in the kinetic energy of the gas. The pressure gradients in the core are caused by the inertia of the gas. The bubble pressure accelerating the liquid slug is considerably less than the pressure of the gas in the center of the core; thus, the kinetic energy developed in the liquid slug is less than the isentropic value. Another effect which contributes to the degradation of the slug kinetic energy is the kinetic energy of the gas itself. This effect can be isolated by using a high-temperature core gas (5 000 K). The gas density is very low; hence,

TABLE XIV
SUMMARY OF SIMMER-II ENERGETICS ANALYSIS

Case	Liquid Slug Kinetic Energy	Vapor Kinetic Energy	Time to Maximum Kinetic Energy (ms)	Per cent Isentropic Energy ($E_0 = 3\ 705\ J$)
Base case				
SRI D-006	2 436	422	2.05	77 %
High Core Temperature				
(5 000 K)	3 083	268	2.00	89.3%
High Slug Density				
($10^6\ kg/m^3$)	3 600	0.2	75	97 %
Large Scale (CRBR)	62 MJ	10.8 MJ	62.25	72.8%

the pressure gradients in the core and bubble are virtually eliminated. However, the bubble driving pressure is 38 atm vs the isentropic 41.5 atm at head impact. The lower driving pressure is due to the motion of the gas and results in slug kinetic energies less than isentropic values.

As shown in Table XIV, all nonisentropic effects can be nearly eliminated by using a very dense liquid slug ($10^6\ kg/m^3$), which increases the expansion time to approximately 75 ms.

Finally, a calculation was made to see how well these experiments scale, within the context of the SIMMER modeling, to a full-size CRBR vessel. The results for this case are also shown in Table XIV. The slight differences from the standard SRI International D-006 case are due primarily to effects which do not scale. Effects which do not scale are the ratio of slug acceleration to gravitational acceleration and the core sound speed distance relationship that characterizes a pressure gradient relaxation time. The effects are quite small, however.

The SIMMER-II code adequately predicts the behavior of the SRI International nitrogen core experiments. With the absence of core structure, the expansions were found to be nonisentropic

due primarily to pressure gradients and motion of the gas within the expanding core bubble. Inclusion of the UCS and UIS reduces the rate of expansion and the ultimate kinetic energy developed by restricting the flow area available for expansion and by diverting some of the flow radially. Including effects which reduce pressure gradients and gas motion within the core allows the calculations to approach the isentropic kinetic energy values. Some small scaling effects do appear when scaling to the full-size CRBR vessel.

2. Feasibility Study of UCS Simulation Experiment

(E. J. Chapyak, Q-7; and V. S. Starkovich, Q-8)

The preliminary feasibility study of a ballistic piston compressor experiment, reported in the previous quarterly,¹⁴ has been extended to include the development of scaling requirements and the selection of simulant materials. This analysis has led to the selection of a simpler experimental apparatus than the ballistic piston, largely because only modest source pressures and temperatures are necessary when the appropriate simulant materials are employed.

Scaling requirements have been developed for the UCS simulation experiment by requiring that the relative magnitude (but not absolute magnitude) of the various terms in the momentum and energy equations be preserved for both prototypic and simulation conditions. Primary emphasis has been placed on phase-change-related scaling criteria, since flashing and melting play a primary role in the accident sequence. For example, we assume that Reynolds number scaling can be relaxed because anticipated large velocities and surface roughness characteristics in the UCS imply that the friction factor is independent of Reynolds number. These requirements have been used to choose simulant materials and operating conditions for a wide range of experimental objectives. For example, a preliminary test series might serve to establish a non-flashing simulation data base, in which case promising simulant materials are propylene glycol for liquid UO_2 or steel, CO_2 for UO_2 vapor, NH_3 for steel vapor, and helium for sodium vapor. Promising simulants for the main test series where UO_2 and steel phase-change phenomena are modeled are propyl alcohol for UO_2 , NH_3

for steel, and helium for sodium vapor. It appears that a satisfactory simulant for liquid sodium is not available.

A schematic design of an apparatus that could be used in this experimental program is presented in Fig. 80. For simplicity, only a single subassembly at 2/5 linear scale reduction is represented. A vacuum line is used to evacuate the area in and above the UCS, which is then filled with helium at a partial vacuum. Note the presence of a movable piston designed to simulate approximately the effects of sodium inertia. The two most complicated engineering features are a fast opening valve (opening time about 3 ms) just below the UCS and an injector mechanism to supply liquid and gas simulant in known amounts to the core region. With regard to the valve, attention is being focused on explosively driven gate valves and pneumatically actuated ball valves. It appears likely that a commercially available version could be used in this program. Construction of the UCS itself can be accomplished with off-the-shelf hardware.

Initial instrumentation will consist of pressure and temperature measurements in the core, UCS and on the piston surface, and visual observation of the piston and the area above the UCS. Measurements of void fraction, droplet size, and velocity will also be included if they prove to be feasible and cost effective.

C. STF Study

(M. G. Stevenson, Q-DO)

1. STF Simulation with Critical Assemblies

(A. E. Evans, B. Pena, R. E. Malenfant, L. R. Creel, E. A. Plassmann, and M. B. Diaz, Q-14)

Hodoscope scanning of the 127-pin FTR bundle, which began last quarter, has continued during this reporting period. We made scans both across flats and across corners of the hexagonal assembly to determine the effect of a pin-sized void as a function of its position in the assembly.

Figure 81 shows the results of scanning with a stilbene scintillation detector biased for neutrons > 1.3 MeV with a corner

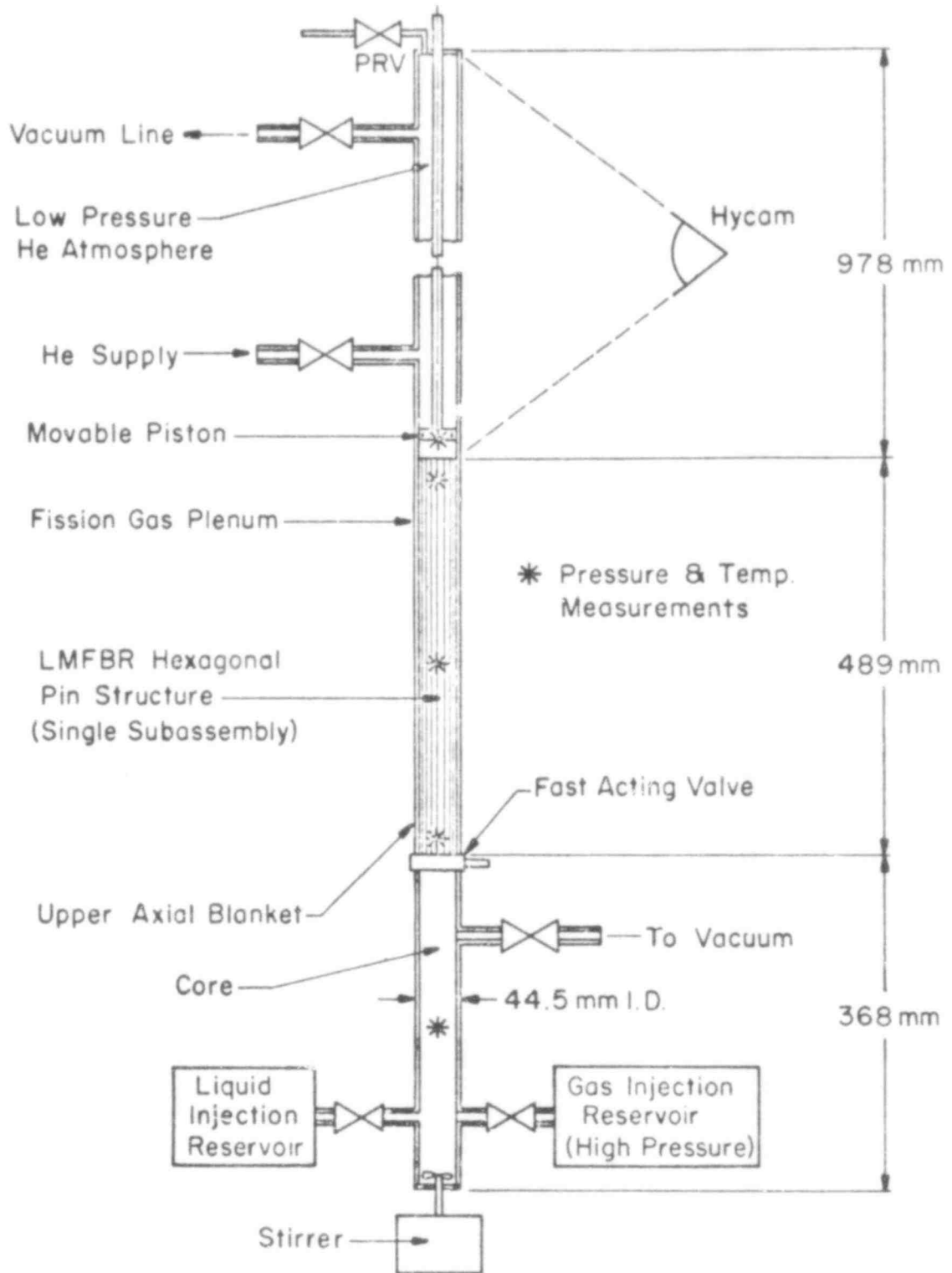


Fig. 80. Schematic of upper core structure simulation experimental apparatus.

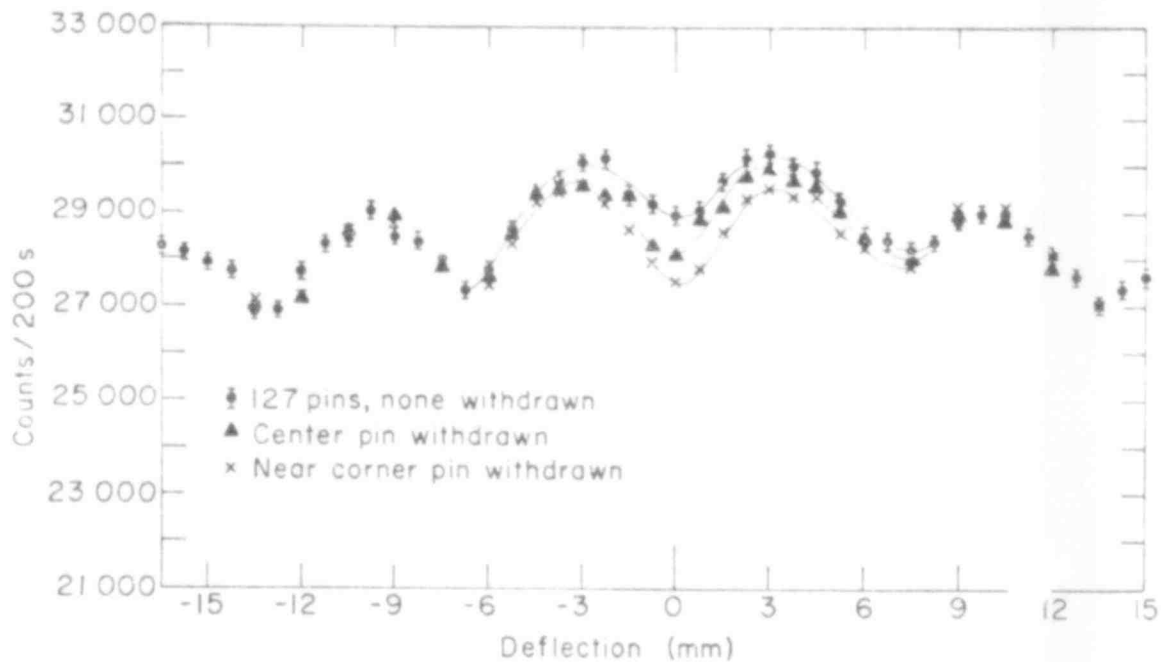


Fig. 81. Results of hodoscope scans across corners of a 127-pin assembly.

of the pin bundle pointed toward the hodoscope. In this orientation, the rows of fuel pins are aligned in the direction of scanning, so that definite maxima and minima appear in the scan. Since the distance between rows of fuel is 6.29 mm and the field of view (to half-maximum intensity) of a hodoscope slot is 7.14 mm at the center of the test section, the hodoscope slot actually "sees" more fuel when the slot is pointed between two rows than when the slot is centered on a row of pins. As a result, a counting rate minimum occurs when the hodoscope slot is pointed at a row of pins.

The figure shows the effect of withdrawing the central pin from the bundle compared with withdrawing the corner pin nearest the hodoscope. Some of the difference between the two pin voids is due to the power distribution within the assembly.¹⁴ It is evident, however, that the response of the hodoscope to a void is dependent on the position of the void within the test assembly. In Fig. 82 we plot the results of scanning the assembly with a single missing pin at various depths within the bundle for both

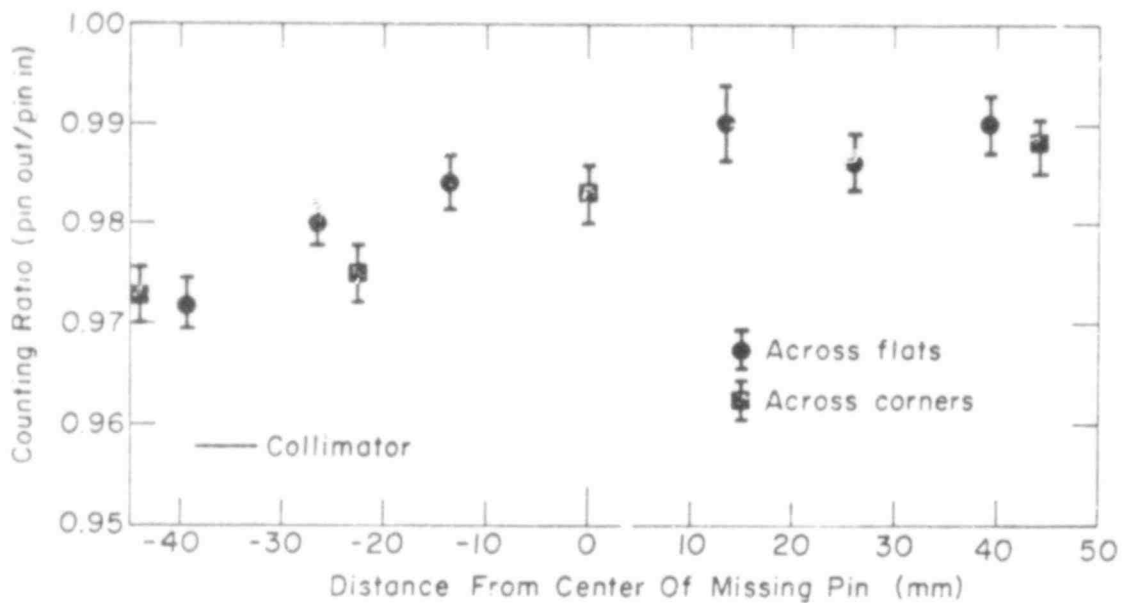


Fig. 82. Hodoscope sensitivity to a single-pin void as a function of the position of the void in test bundle.

across-corners and across-flats scans. The data, again taken with the stilbene detector biased for neutrons above 1.3 MeV, show that the total counting rate reduction for a single-pin void in a 127-pin assembly varies from 3% for a void in the near edge of the assembly to 1% at the far edge. These data, which have been normalized to a constant power distribution within the assembly, show the need for a detailed static hodoscope study of every large bundle test before a destructive experiment is run. The desirability for three-dimensional test data, as from crossed hodoscopes, is also evident.

IV. HTGR SAFETY RESEARCH
(M. G. Stevenson, Q-DO)

Under the sponsorship of the NRC/RSR, LASL is conducting a program of research in High-Temperature Gas-Cooled Reactor (HTGR) safety technology in the following task areas:

- Structure Evaluation
- Phenomena Modeling, Systems Analysis, and Accident Delineation
- Fission Product Release and Transport

Progress for this quarter in the first two areas is reported below.

A. Structural Investigations
(C. A. Anderson, Q-13)

Single impact tests of small (50.8 mm x 50.8 mm x 50.8 mm) graphite and plastic two-dimensional model blocks have been completed. Good agreement between predicted and measured impact force vs time histories indicates that the scaling laws being used are appropriate. Modifications to the White Sands Missile Range (WSMR) servohydraulic shaker are under way and testing of the two-dimensional core block systems may begin in November 1978.

The NONSAP-C user's manual has gone to press, and the source code and test problems have been sent to the HTGR Safety Code Library at the Brookhaven National Laboratory (BNL). Numerical difficulties have occurred in the application of the elastic-plastic concrete constitutive law to a three-dimensional finite element model.

1. Code Development for Analysis of Prestressed Concrete Reactor Vessels (PCRVs)

(C. A. Anderson and P. D. Smith, Q-13)

The user's manual for the NONSAP-C code has gone to press. A tape containing the NONSAP-C source code and several test

problems has been sent to the HTGR Safety Code Library at BNL. In both cases, the source code is a version that contains standard FORTRAN coding. Execution efficiency can be gained by local revision of input/output routines to take advantage of installation-dependent capabilities.

The elastic-plastic concrete model of Chen and Chen has worked on simple cube and ring meshes, but has not yet been successful on a three-dimensional mesh of a model PCRV. The elastic portion of the response of the PCRV is obtained, but the onset of yielding in only a few elements causes the iterative solution to fail to converge. The difficulty appears to be associated with the discontinuity in the yield surface at the junction of the compression-compression and tension-compression regions.

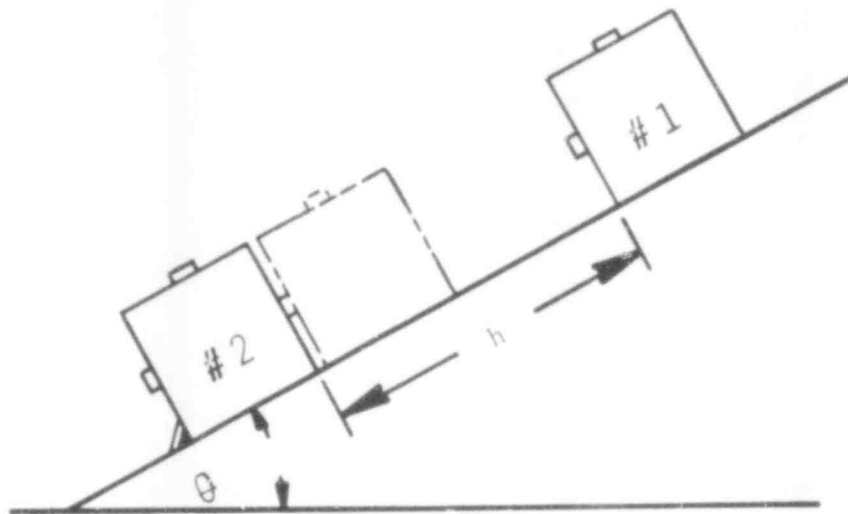
Two changes were made in the NONSAI-C code. The membrane element has been modified to allow the user to specify initial stresses in the element. When used in conjunction with the linear orthotropic material model, the membrane element with initial stress simulates a prestressing tendon. In an effort to conserve computer time, the three-dimensional element integration routines have been modified to permit use of from one to four integration points in each of the three coordinate directions.

2. Experimental Seismic Program

(R. C. Dove and W. E. Dunwoody, Q-13)

As a result of several conferences with the personnel in charge of the servohydraulic shaker at WSMR, it was agreed that necessary modifications to the shaker facility would be made (by WSMR) during September and October. As a result, testing of our block model systems may begin as early as November 1978. The necessary contractual arrangements for these two-dimensional tests have been completed.

The single impact tests of the small (50.8 x 50.8 x 50.8 mm) graphite and plastic two-dimensional model blocks were completed. These tests were conducted by impacting two model core blocks one on the other as shown in Fig. 83. Contact force vs time was recorded for the impact by means of the contact force transducer which is an integral part of each block. The calibration of this



h - SLIDING DISTANCE

θ - SLID ANGLE

BLOCK #1 SLIDES AND IMPACTS WITH A VELOCITY OF V_1 INTO BLOCK #2 WHICH IS CLAMPED IN PLACE

Fig. 83. Single block impact test.

transducer was discussed in the previous progress report.¹⁴ Considering the plastic blocks to be models of the graphite blocks it is possible to predict the force vs time history for the graphite blocks. Comparison of this prediction to the actual force vs time history (obtained by testing of the graphite blocks) is used to check the scaling laws.

Figure 84 shows the general shape of the impact force vs time signal that was obtained together with the parameters measured and compared. Table XV shows values measured for plastic block (model) impact, together with the values predicted for and measured on the graphite block (prototype). The good agreement between the predicted and measured values indicates that the scaling laws being used are appropriate.

Single impact tests on the large (175 x 175 x 175 mm) graphite blocks are now in progress.

Two complete sets of small (50.8 x 50.8 x 50.8 mm) blocks have been fabricated. One set consists of 24 plastic blocks, the other of 24 graphite blocks. Figure 85 is a photograph of the

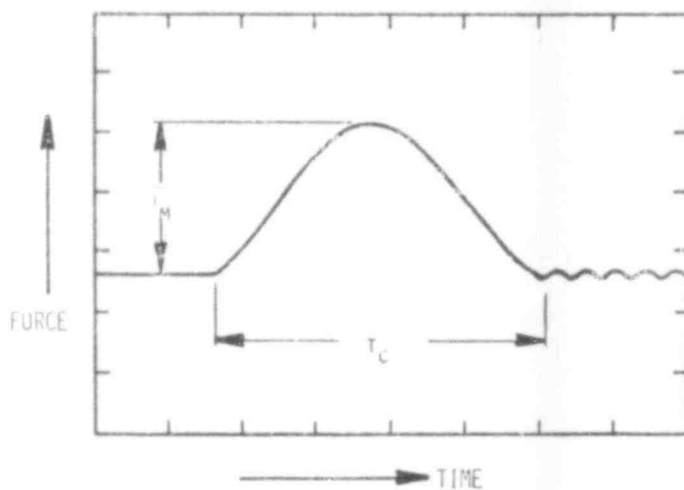


Fig. 84. Force-time history.

complete set of small plastic blocks assembled but without the mounting fixture. The fixture for assembling these models on the servohydraulic shaker is 50% completed. These model blocks are now being strain gaged and calibrated in preparation for testing on the servohydraulic shaker at WSMR. Figure 86 is a photograph showing each of the blocks to be tested.

TABLE XV
SINGLE BLOCK IMPACT PREDICTIONS AND TEST RESULTS

	Measured on Plastic ^a	Predicted for Graphite ^b	Measured on Graphite ^c
Peak Force ^d			
F_M - Newtons	270	1 419	1 366
(lbs)	(60.8)	(319)	(307)
Contact Time			
t_c -microsecond	755	400	392

^aAverage of 4 tests, sliding distance $h_m = 3.63$ cm.

^bFor this system of plastic and graphite with a length scale (N_x) of unity (blocks of the same size), the force scale (N_f) is 5.25 and the time scale (N_t) is 0.53.

^cAverage of 8 tests, sliding distance $h_p = 12.71$ /cm.

$$h_p = \frac{N_E}{N_o} \times h_m = \frac{5.25}{1.5} \times 3.63 = 12.71 \text{ cm.}$$

^dPeak force computed from strain gage reading using static calibration data.

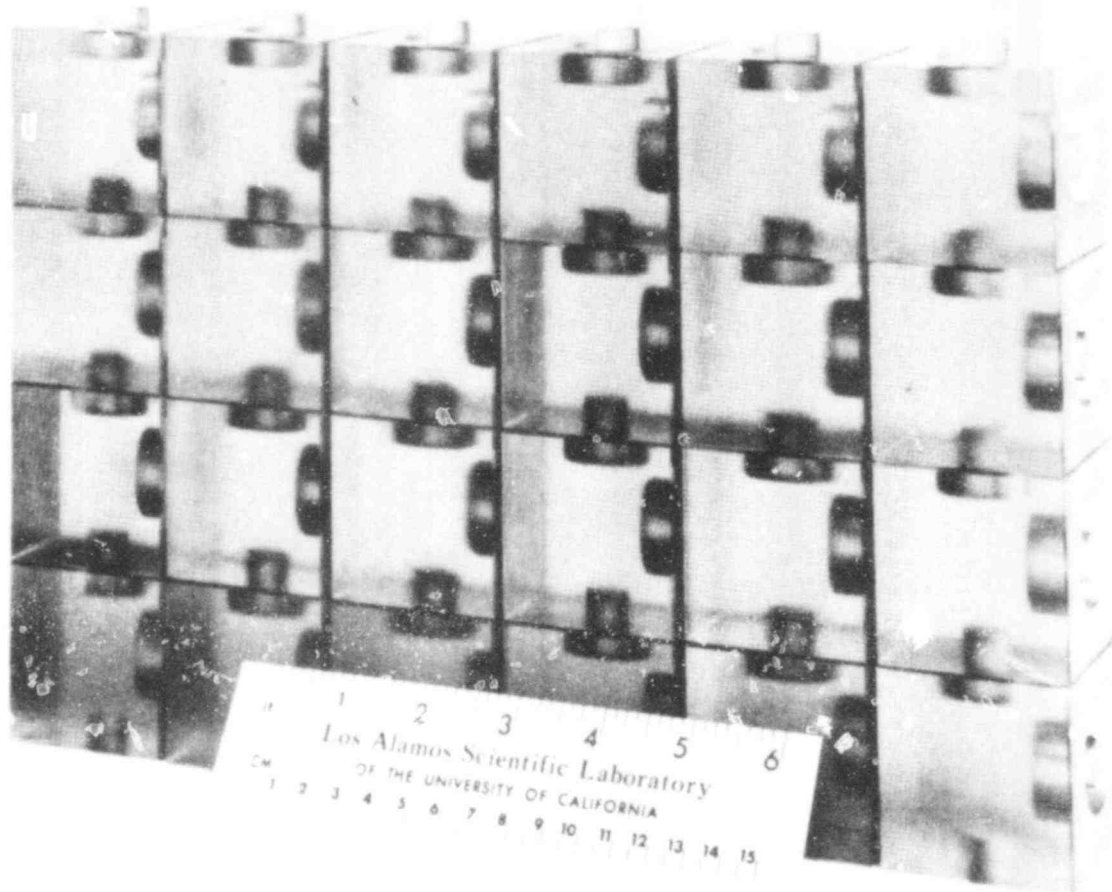


Fig. 85. Assemblage of plastic (model) blocks.

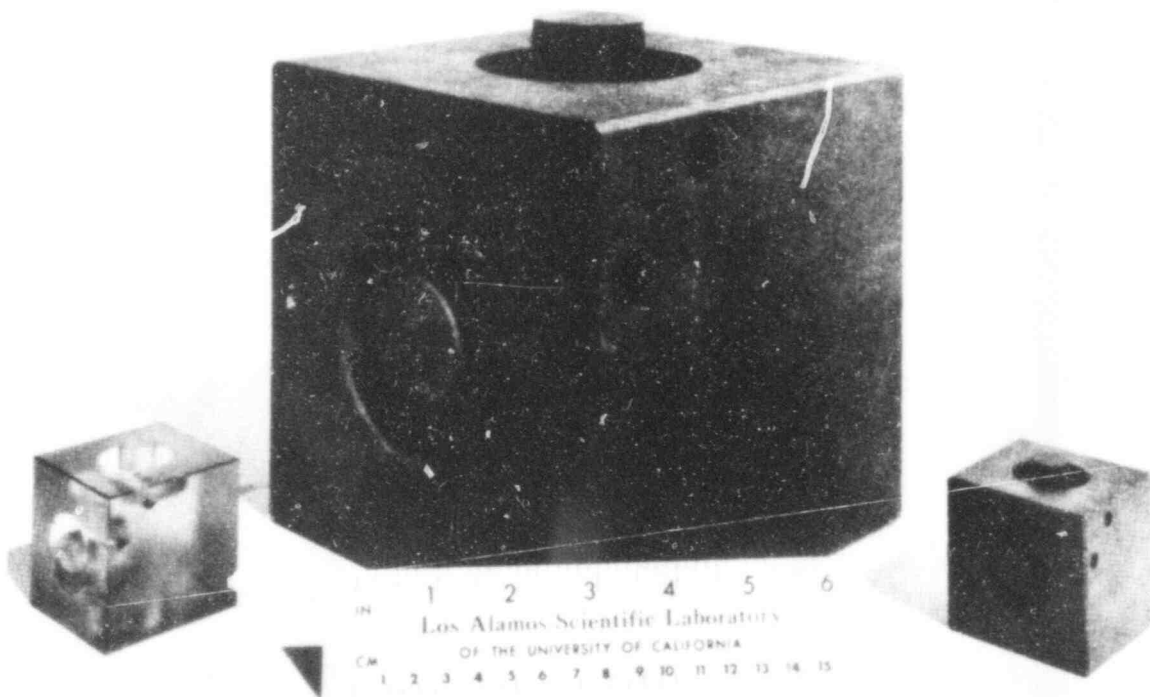


Fig. 86. Graphite model, graphite prototype, and plastic model blocks (right to left) for two-dimensional seismic tests.

From left to right these are the small plastic, large graphite, and small graphite blocks, respectively.

B. Phenomena Modeling and Systems Analysis

(P. A. Secker, Q-6)

The phenomena modeling and systems analysis task is primarily concerned with the development, verification, and application of Gas-Cooled Reactor (GCR) consolidated plant simulation computer programs. The Composite HTGR Analysis Program (CHAP) consists of a model-independent systems analysis program called LASAN which has steady state, transient, and frequency response solution capabilities. The model-dependent portion of CHAP consists of linked modules, each representing a component, subsystem, or phenomenon of the overall HTGR plant model and having a standardized modular structure. The program organization facilitates modification of component models, modification of solution algorithms, and addition of new solution techniques. Overlay and nonoverlay versions of the code have been developed. The initial version (CHAP-I) models the 3 000 MW(t) HTGR. CHAP-II is currently under development and models the Fort St. Vrain (FSV) HTGR.

During the past quarter, the FSV component modules were completed. Refinements were made to the water equation-of-state (EOS) subroutine which reduce computer running times by 60%. The EOS data were extended below atmospheric pressure and above the critical pressure for water.

Transient studies were made for rapid depressurization of the HTGR with air and steam ingress to the reactor core and the reactor containment building. Feedwater transients were run to study the natural harmonic frequencies of the plant thermal hydraulics.

1. FSV Modeling

(P. A. Secker, G. J. E. Willcutt, Jr., and P. L. Rivera, Q-6; R. B. Lazarus, C-3; and T. McDonald, E-4)

Modeling of the FSV Nuclear Electric Generating Station was completed during this quarter. The overall plant model consists

of 22 coupled modules. These modules have been incorporated into both the overlay and nonoverlay versions of CHAP. The current versions of the code permit the user to study either a 3 000 MW(t) HTGR (CHAP-I) or the FSV HTGR (CHAP-II). A single option parameter, namely IOPFSV, is used to select the appropriate model.

Two independent data files have been compiled for the separate versions of CHAP. Table XVI is a list of the modules included in the two versions of CHAP, with a description of the function of each module.

A nonoverlay version, without formal documentation, was prepared for release to BNL. Documentation of the code is 60% complete.

2. Reactor Containment Analysis

(P. A. Secker and D. Dube, Q-6)

We previously reported the development of the reactor containment building module for CHAP.¹⁴ During the past quarter, a number of containment building accident scenarios were studied involving depressurization of the FSV PCRV. In these scenarios, a specified area of flow restrictor failure was postulated. Pressurized helium then flows from the PCRV into the containment building.

In the first study, the break occurs in the reactor upper plenum where the helium has a pressure of 5 000 kPa and a temperature of approximately 600 K. Figure 87 shows the response of the upper plenum pressure and loss of helium mass in the PCRV for a 645 cm² break in the vessel. This represents the design basis depressurization accident (DBDA) for FSV. Figures 88 and 99 show the reactor containment building pressure and gas mixture average temperature response during the DBDA. Within a few seconds after the postulated break occurs, louvered vents in the building are opened allowing the building pressure to drop rapidly. The peak temperature obtained is 365 K which is about 15 K greater than the maximum temperature reported in the FSV Final Safety Analysis Report.³⁷ Figure 90 shows the mass fraction of helium in the containment building following the depressurization event.

TABLE XVI
CHAP MODULES

<u>Name</u>	<u>Function</u>
BOUNDS	Universal boundary condition module
CACS	Core auxiliary cooling system helium/water thermal hydraulics [used in 3000 MW(t) model only]
RHTDUC	Reheater helium duct thermal hydraulics
REHTR	Steam reheater helium/water thermal hydraulics
FEDWTR	Feedwater components including heaters, pumps, valves, pipes, and main condenser.
STMGEN	Main steam generator helium/water thermal hydraulics
HPTBYP	High-pressure turbine and turbine bypass water thermal hydraulics
HECIRC	Helium circulator compressor/turbine helium/water thermal hydraulics
CIRDUC	Helium circulator exit helium duct thermal hydraulics [used in 3000 MW(t) model only]
UPPLER	PCRV upper plenum/helium thermal hydraulics
KINET	Reactor point kinetics and decay heat
CORE	Reactor core/helium thermal hydraulics
REFL	Reactor side reflector/helium thermal hydraulics
LOWPLN	PCRV lower plenum/helium thermal hydraulics
LPTBYP	Intermediate/low-pressure electric turbine water thermal hydraulics with bypass
CTFFOD	Reactor control
CNTMNT	Reactor containment building thermal hydraulics
CTLHEC	Helium circulator control
CTLHPT	High-pressure turbine control
CTLLPT	Intermediate/low-pressure turbine control
CTLFED	Feedwater components control
HAZARD	Radiation release model for failed HTGR fuel and fission product transport in the PCRV and containment building

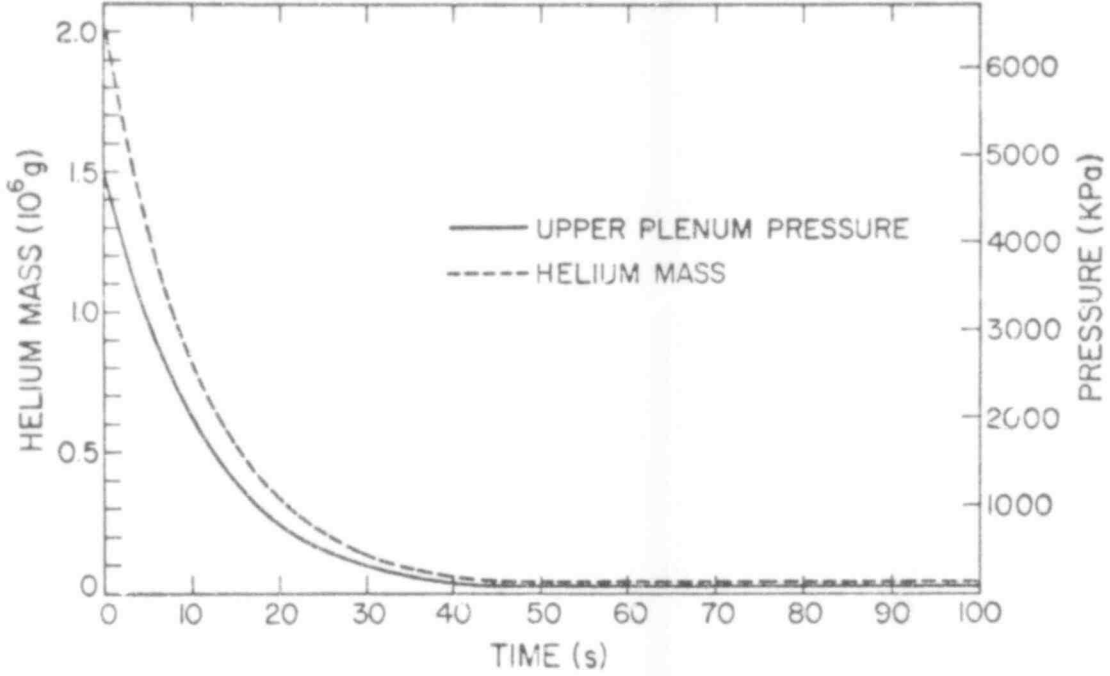


Fig. 87. PCRV pressure and helium mass response for the FSV DBDA.

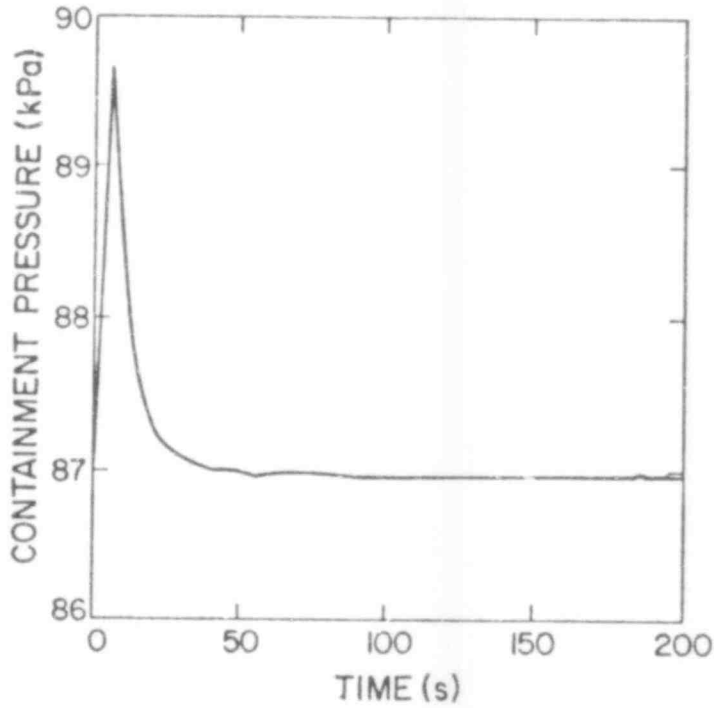


Fig. 88. Containment pressure response for the FSV DBDA.

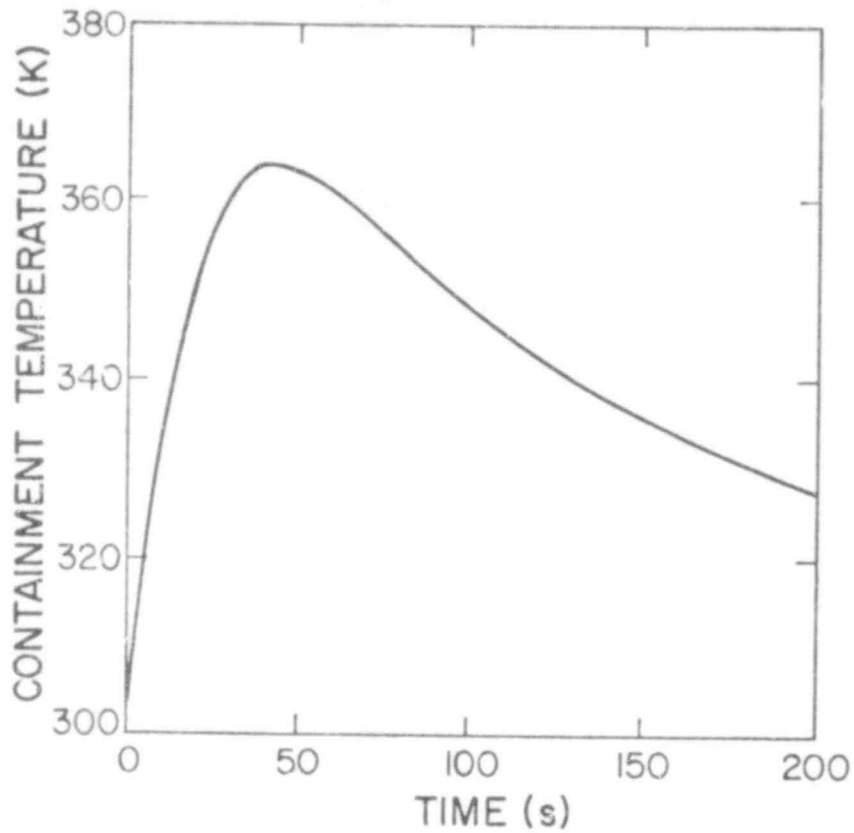


Fig. 89. Containment temperature response for the FSV DBDA.

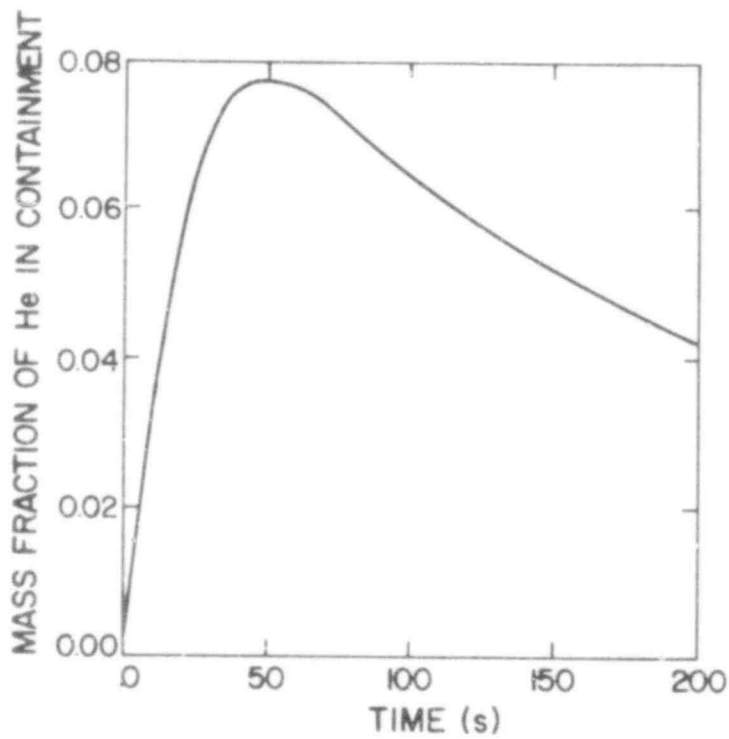


Fig. 90. Containment helium mass fraction following the FSV DBDA.

We also studied a steam line break into the containment building. The steam conditions corresponded to main steam generator exit conditions, and are given below, along with the assumed leak rate.

Steam pressure	16 650 kPa
Steam temperature	812 K
Steam leak rate	0.52 kg/s

Figures 91 and 92 show the containment building pressure and gas mixture mean temperature for the break. Figure 93 shows the containment building molecular weight as steam continues to enter the building.

3. Feedwater Transients

(P. A. Secker, Q-6; and R. B. Lazarus, C-3)

During this quarter, we studied the natural frequencies of the feedwater component thermal hydraulics using step changes in boundary conditions. For example, the helium inlet temperature on the shell side of the steam reheater was stepped by 100 K from its equilibrium condition of 990 K.

Figures 94 and 95 show the system closed loop (with controllers operative) response of the steam generator exit steam temperature and the exit reheat steam temperature to this perturbation. The

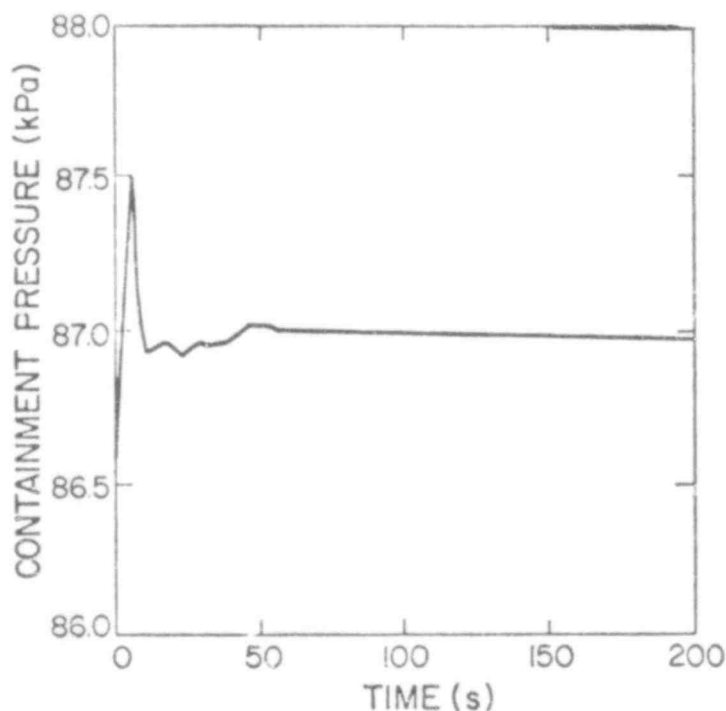


Fig. 91. Containment pressure response to a FSV steam line break accident.

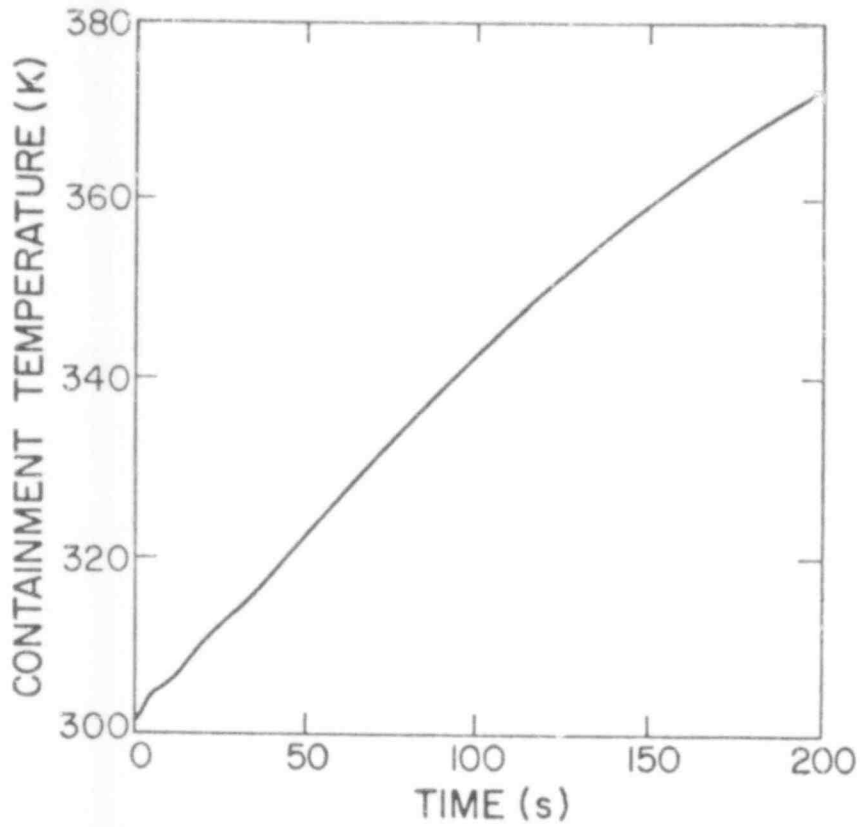


Fig. 92. Containment temperature response to a FSV steam line break accident.

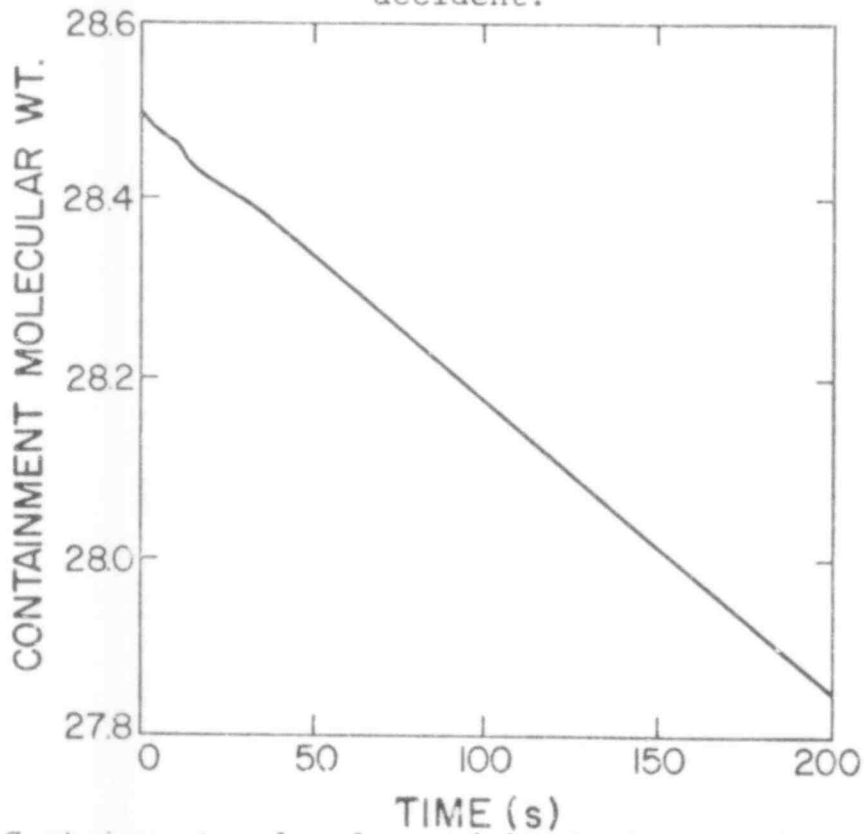


Fig. 93. Containment molecular weight during a FSV steam line break accident.

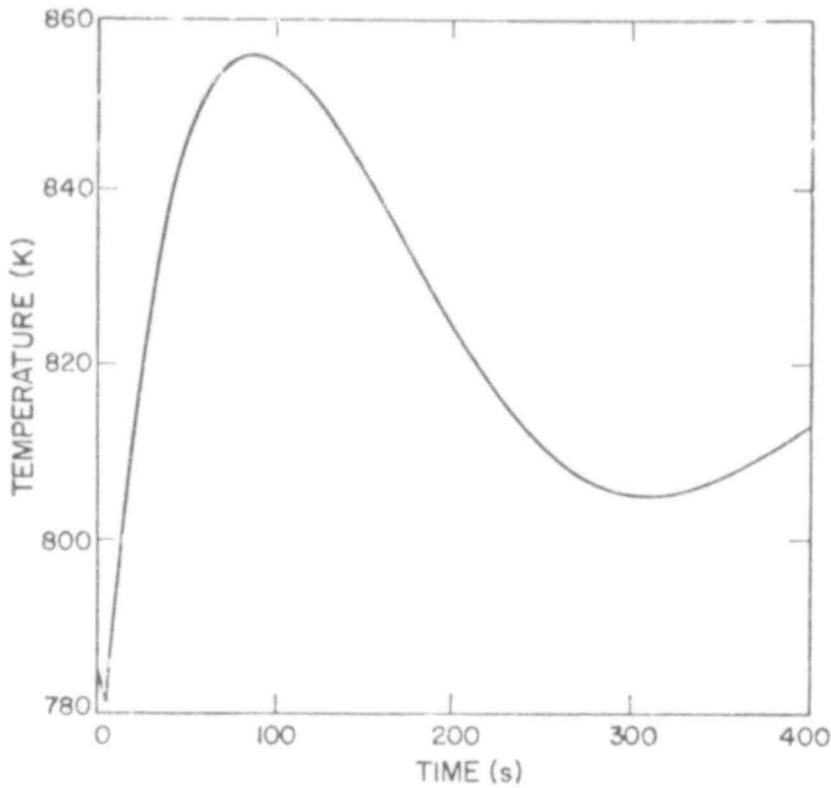


Fig. 94. Steam generator outlet steam temperature response to a 100 K step increase in reheater inlet helium temperature.

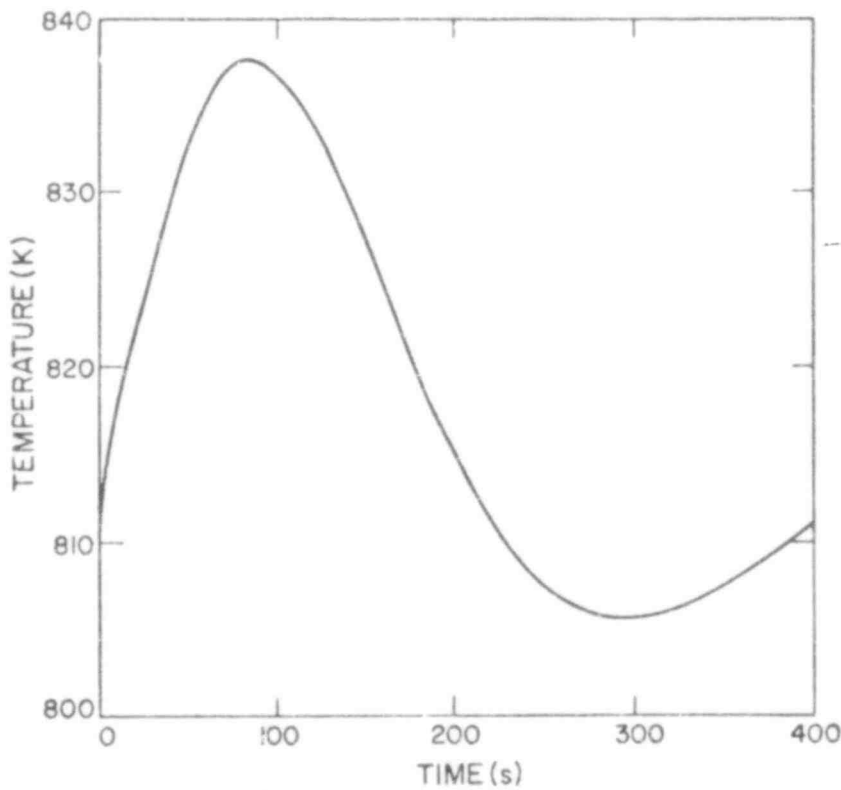


Fig. 95. Reheater outlet steam temperature response to a 100 K step increase in reheater inlet helium temperature.

period of oscillation of these two temperatures is 440 s. The transient reaches equilibrium within 1 600s. This period of oscillation is important because it closely matches that observed in the FSV power oscillations. We are continuing our feedwater transients to determine whether the natural frequencies of the feedwater thermal hydraulics can contribute to the observed power oscillations by coupling through steam generator/reheater heat transfer, helium circulator response, plant control, etc.

4. Water Equation of State

(P. A. Secker, Q-6)

The water EOS routine in the CHAP code is based on tabular ASME data.³⁸ The range of pressures for which we have tabulated data is from 102-22 104 kPa, i.e., standard atmospheric pressure to the critical pressure of water. However, EOS data are required from approximately 7 kPa (condenser conditions) to 23 500 kPa (feedpump exit conditions).

We extended the EOS range within the routine using Van der Waal's relationship. At the same time, we maintained continuity of state properties and thermodynamic derivatives with the tabular ASME data.

Van der Waal's EOS for water has the form:

$$V = \frac{C_1 V^2 T}{C_2 + V^2 P} + C_3, \quad (9)$$

where

- V is specific volume,
- T is absolute temperature,
- P is absolute pressure, and
- C_1 , C_2 , and C_3 are constants.

Equation (9) is a transcendental equation for specific volume when temperature and pressure are known. Several assumptions were used to take advantage of Eq. (9) for single-phase liquid or vapor. Where V occurs on the right-hand side in Eq. (9), we chose to

approximate its value using a Taylor series expansion about the tabular ASME data at atmospheric pressure or the critical pressure.

$$V' = V_o + \left(\frac{\partial V}{\partial P}\right)_o (P - P_o) + \left(\frac{\partial V}{\partial T}\right)_o (T - T_o) , \quad (10)$$

where P and T are known and P_o , T_o , $\left(\frac{\partial V}{\partial P}\right)_o$, $\left(\frac{\partial V}{\partial T}\right)_o$, and V_o are obtained from tabular data.

The constants C_1 , C_2 , and C_3 are evaluated so that V , $\left(\frac{\partial V}{\partial P}\right)$, and $\left(\frac{\partial V}{\partial T}\right)$ match the tabular data at $P = P_o$ and $T = T_o$. The values of the constants are

$$C_2 = -V_o^2 \left[P_o + \frac{T_o \left(\frac{\partial V}{\partial T}\right)_o}{\left(\frac{\partial V}{\partial P}\right)_o} \right] , \quad (11)$$

$$C_3 = V_o - \frac{1}{2 \left[\frac{1}{V_o} + \frac{P_o \left(\frac{\partial V}{\partial P}\right)_o}{V_o T_o \left(\frac{\partial V}{\partial T}\right)_o} + \frac{1}{2 T_o \left(\frac{\partial V}{\partial T}\right)_o} \right]} , \quad (12)$$

and

$$C_1 = \frac{(V_o - C_3)(C_2 - V_o^2 P_o)}{V_o^2 T_o} . \quad (13)$$

The extended relationships match actual data within 0.7% for the range of interest in CHAP. Two-phase water relationships have also been incorporated by extending the tabular saturation curve data below atmospheric pressure.

We determined that, for feedwater transients, initially 75% of computer running time was spent in the water EOS routine. A bi-linear search routine was added to the routine and an LCM storage feature of water data was written which reduces feedwater transient solution times by 60% for a complete plant model.

5. LASAN Improvements

(P. A. Secker, Q-6; and R. B. Lazarus, C-3)

Several improvements were made to the LASAN analytical methods. The steady-state logic was modified to reflect the min.-max. limits on all state variables. When a state variable reaches one of its limits during the steady-state computation, the Jacobian matrix is reduced in size by one row and one column, and the state variable is treated mathematically as an input parameter.

The iterative linear system solution method used for transient, frequency response, and steady-state calculations was modified to treat several N-tuple's rather than one. The code now investigates the Jacobian matrix for banded structure and solves all N-tuples greater than $N = 2$ using the appropriate bandwidths. All matrix data used in the linear system solver are stored in LCM.

V. GCFR CORE DISRUPTIVE TEST PROGRAM
(D. L. Hanson, Q-13)

The basic assembly module of the Gas-Cooled Fast Reactor (GCFR) core is a subassembly comprising 264 fuel rods, 6 corner support rods, 1 central rod (instrumented), and their surrounding duct. The duct is a right hexagonal cylinder. The purposes of this out-of-pile experimental program are to demonstrate the behavior of one of these GCFR core modules in the event of loss-of-core coolant flow or pressure and subsequent shutdown of reactor power to the level resulting from decay heat alone. The LOFA will be simulated in the Duct Melting and Fall-away Test (DMFT) and the loss of pressure accident will be simulated in the Depressurized Accident Condition (DAC) test. These experiments require the development of an electrically heated fuel rod simulator capable of delivering 2 kW of power while operating at surface temperatures exceeding 1 650 K, and the development of a fixture that will permit operation of an ensemble of 450 such rods (1 core module thermally guarded by segments of the 6 surrounding modules) at helium pressures up to 9.1 MPa. This Guarded Core Module (GCM) fixture will be the largest in a sequence of four test fixtures developed in the course of this program. The others are:

- Ten-inch, single-rod fixture,
- One-meter, seven-rod fixture, and
- Full-length Subgroup (37-rod) fixture.

The GCM fixture will be used first for the DMFT and subsequently for the DAC test.

A. Program Planning

(D. L. Hanson, Q-13)

The Full-length Subgroup-2 (FLS-2) test is being delayed pending the outcome of the spacer-grid/cladding mechanical interaction investigation. It is tentatively scheduled to be performed in February 1979. A follow-up test, FLS-3, is scheduled for the following June, if required.

The first Duct Melting and Fall-away Test (DMFT) is now scheduled for October 1979. This represents a delay from earlier estimates, primarily due to the fact that the Guarded Core Module (GCM) pressure vessel now has an anticipated delivery time of 40 weeks.

B. Analysis

(A. J. Giger, D. L. Hanson, and C. Prenger, Q-13)

1. Spacer-grid/Cladding Friction

Formulas have been derived for empirical determinations of friction coefficient between spacer grid cells and cladding in one-point, two-point, and three-point contact. The formulas and the test conditions under which they apply are given in Table XVII.

The parameters used in the formulas are defined as follows:

- μ = coefficient of sliding friction,
- μ_c = critical friction coefficient (i.e., coefficient of static friction at incipient lockup in a cocked configuration),
- P = horizontal load,
- W = vertical load,
- h = axial length of clad-guiding surface in grid,
- e = transverse displacement of the line of action of the motion-inducing force from clad centerline,
- Y = distance from center of clad-guiding surface in grid to center of gravity of clad (measured along the clad axis),
- β = angular displacement of each side-riding contact point from a point diametrically opposite the center-riding contact,
- α = angle between the clad centerline and the clad-guide centerline, and
- λ = angle between axial and total friction forces.

The formulas will be used to analyze data acquired from the investigation of the mechanical interaction between spacer grids and cladding. Experiments related to this investigation are described in Sec. E, below.

TABLE XVII

SPACER-GRID/CLADDING CONTACT CONFIGURATIONS AND FRICTION FORMULAS

CONFIGURATION					FORMULA
ATTITUDE				No. of Contact Points	
Grid Plane	Clad Axis	Motion-Inducing Force			
		Direction	Location		
Vertical	Horizontal	Horizontal	Concentric	1	1 ^a
				2	2 ^a
Near-Vertical (Max. Cocking)	Horizontal	Horizontal	Eccentric	2	3 ^a
				3	4 ^a
Horizontal	Near-Vertical (Max. Cocking)	Near-Vertical	Eccentric	2	5 ^a
				3	6 ^a

^aFORMULA

1. $\mu = P/w$

4. $\mu_c = \left(1 + \frac{\cos\lambda}{\cos\beta + \mu_c \sin\lambda \sin\beta}\right) = \frac{h}{\epsilon}$

2. $\mu = \frac{\cos\beta}{\frac{w}{p} \cos\lambda - \sin\lambda \sin\beta}$

5. $\mu_c = \frac{h}{2\alpha y}$

3. $\mu_c = \frac{h}{2\epsilon}$

6. $\mu_c \left(1 + \frac{\cos\lambda}{\cos\beta + \mu_c \sin\lambda \sin\beta}\right) = \frac{h}{\alpha y}$

2. FLS-1 Postmortem AnalysisVisual Examination of the Tube Bundle

Visual access to one side of the FLS-1 tube bundle was gained by removing half of the stainless steel duct (i.e., half of the circumference removed over the entire length). Alumina sleeves exposed by sloughing of melted cladding from the upper part of the core region are shown in Fig. 96. The molten cladding flowed downward as far as the second spacer grid below the core midplane station. Accumulated steel is evident at that location, as shown in Fig. 97. The same accumulation and another on the next higher spacer grid are shown in Fig. 98 as indicated by radiography.

There also are indications of mechanical interaction between the cladding tubes and the spacer grids. Among these are serpentine curvature of cladding tubes, cocking of cladding guide tubes in spacer grids, scoring of cladding near the spacers, and cocking of spacer grid planes.

Heater Rod Failure

The analysis of spacer-grid/cladding interaction has been prompted by the belief that frictional lockup of cladding tubes in spacer grids was responsible for the heater rod failures that occurred during the FLS-1 test. The presumed mechanism for rod failure from this cause consists of the sequence of steps.

1. Axial clad growth due to the increasing temperature.
2. Clad bowing due to radial nonuniformity of temperature.
3. Lockup of the cladding tube in at least one spacer grid remote from the fixed end of the tube.

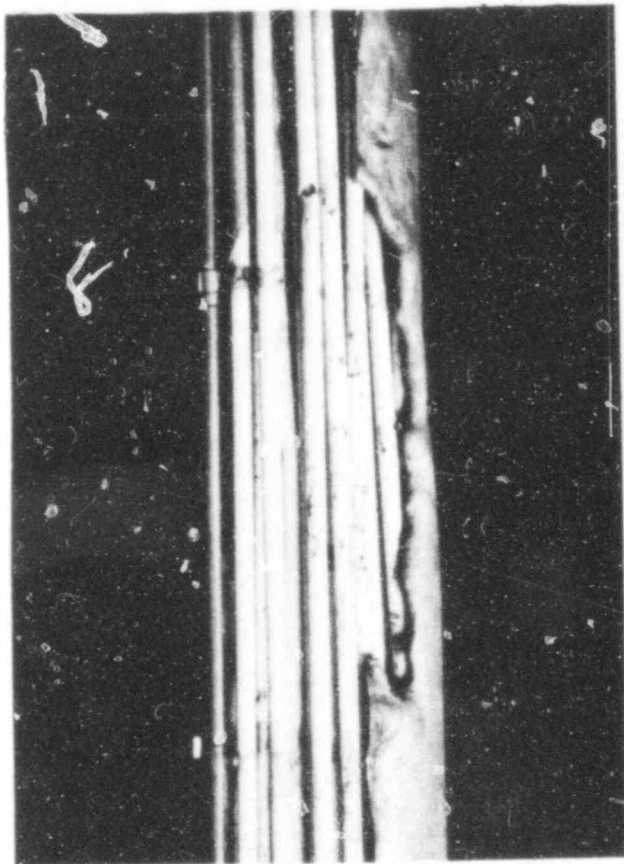


Fig. 96. Alumina sleeve exposed by sloughing of SS cladding.

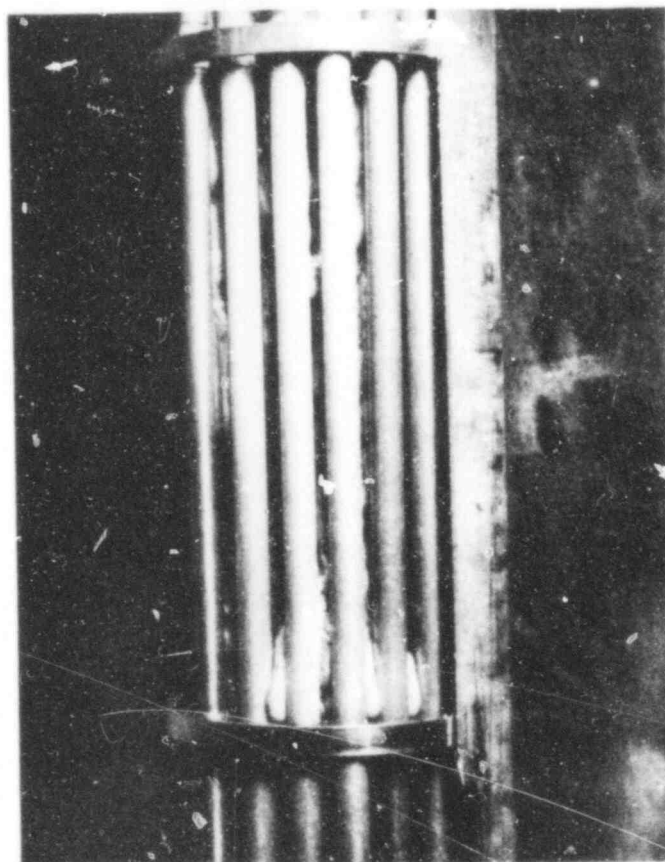


Fig. 97. Photo shows steel accumulated above spacer grid #7.

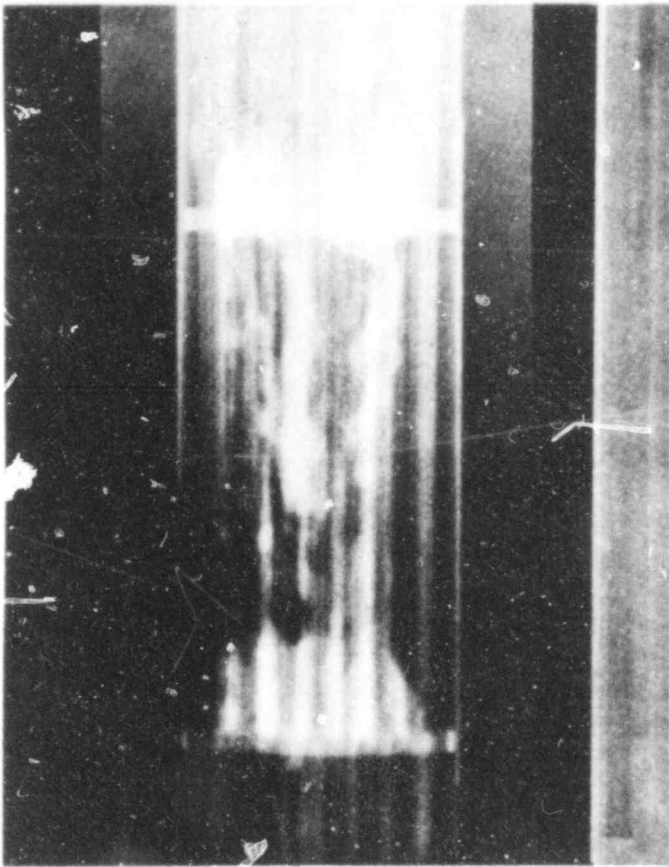


Fig. 98. Radiograph shows steel accumulated above spacer grids #6 and #7.

4. Further axial expansion of the cladding, causing the tube to bow and/or buckle in the region of highest temperature.
5. Heater rod fracture due to buckling of its outer support structure.
6. In the FLS-1 test (which was performed under a constant-current mode of power control), the current from each failed rod was distributed among the survivors, thereby raising their temperature and restarting the cycle.

In regard to this postulated failure mechanism, two points are worthy of special note. First, the potential for frictional lockup of the cladding tubes in the spacer grids is easily demonstrated to be good (discussed further under Sec. E, below). Second, each rod failure would become successively worse in terms of its impact on the operating assembly of rods because later failures dump larger current increments into fewer survivors. Presumably, this would increase the failure rate with time, as was observed (by inference from the exponential increase of voltage with time).

3. DMFT Support Frame Thermal Analyses

A short FORTRAN program was written to analyze support frame cooling. It was found that, depending on material, the uncooled forming rings can maintain reasonable temperature by conduction to the water-cooled stanchions. The program indicates it is feasible to use C-1015 rather than more costly beryllium-cooper for the rings. Nominal design of the support frame has the characteristics shown in Table XVIII.

TABLE XVIII

DMFT SUPPORT FRAME NOMINAL DESIGN

Ring Material	C-1015
Clamp Bolts Preload	0.517 GN/m ²
Stanchions (34.9 o.d. x 4.76 mm)	C-1015
Annulus Gap	1.59 mm
Coolant Flow Rate	1.26 kg/s
System Pressure Drop	33.4 kN/m ²
Water Temperature Rise	3.4 K
ΔT , Film	7.74 K
ΔT , Stanchion Wall	3.64 K
ΔT , Clamp Joint	0.13 K
$\Delta T_{\text{max average}}$, Ring	30.51 K
Ring Diameter Increase	0.304 mm

losses through the relatively thick insulation to the 293 K sink at the boundary.

Results of the guard heater analysis allow a more accurate analysis of the structural support for these heaters.

C. Design

(A. J. Giger and W. E. Dunwoody, Q-13)

271-Rod GCM Experiment

Because of its approximately 13 600 kg mass, the pressure vessel (PV) for GCM tests will be fixed in place, and DMFT experiments, previously assembled into a support frame, will be lowered into the PV and service connections made thereto. Design of the support frame for DMFT, shown in cross section in Fig. 100, is

4. DMFT Guard Heater Thermal Analysis

A thermal analysis of a guard heater for the core module was completed using a 5-node finite difference model. The lumped parameter network representing the guard heater is shown as Fig. 99. A steady-state power for the heater rods which resulted in temperatures close to the melting point of 316 SS was found and used for the analysis (0.44 w/cm).

The analysis showed the temperature difference between the inner and outer walls of the guard heater was 275.6 K. The small difference is attributed to high heat transfer from radiation and convection within the cavity compared to very low

LEGEND



INDEX

- 1 Gas
- 2 Inside Wall
- 3 Heater Rods
- 4 Outside Wall
- 5 Environmer.

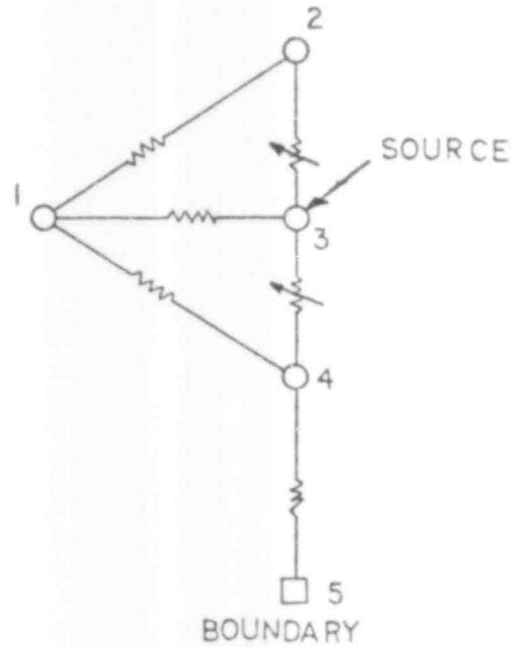


Fig. 99. Guard heater cavity thermal model network.

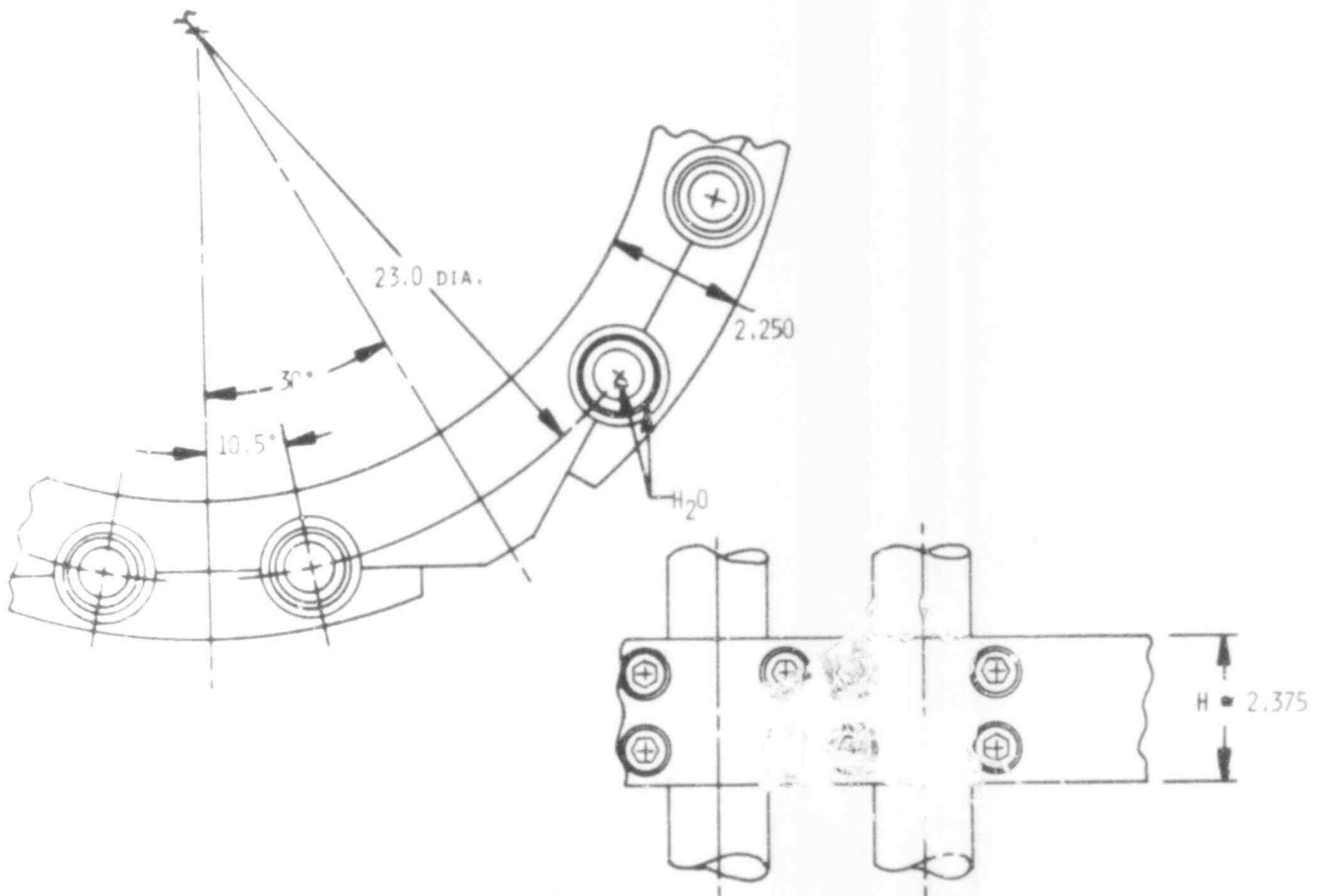


Fig. 100. Support frame.

about 75% complete. The frame will comprise 12 vertical water-cooled stanchions, manifolded at the top and approximately 10 bolted-on forming rings on which are mounted electrical connections, structural supports, and insulation.

By this design, distortion from welding and the expense of machining on a large structure (4.7-m-high x 0.63-m-diam) are avoided. The PV will be used as a jig to accurately locate pass-through connections (principally electrical) on the test frame. Because of the high degree of dimensional stability of the PV in operation and the longitudinal stability of the frame, satisfactory operation is expected from the radial PV pass-throughs.

Support of the core module on the test frame is accomplished using a thick piece of material cut out to form a six-spoke plate. This permits drop-in assembly of the insulated guard heaters around the core module. Preliminary analysis has indicated that the plate design selected has relatively low stresses and that it will be possible to use thoria dispersed (TD) nickel for this uncooled component.

Guard heater supports have been designed that permit longitudinal thermal expansion with minimum radial motion. A special support link has been designed that, considered by itself and at constant temperature, allows a maximum radial deviation of ± 0.053 mm over an axial growth range of 37.7 mm. This link is employed at the bottom support point to help maintain a prototypic gap between the core module and the guard heaters.

Design of the guard heaters themselves is about 50% complete. Arrangement of the heaters within these units will be analogous to that used for the 37-rod FLS experiment (the spacer grid design being held in abeyance).

The fabrication drawings for the DMFT pressure chamber cooling panels have been completed and revised to the latest update on the pressure vessel and internal test package.

508 170

D. Fabrication and Procurement

(W. E. Dunwoody, Q-13)

The purchase order for the 271-pin GCM pressure chamber has been completed.

E. Testing

(R. Renfro and D. L. Hanson, Q-13)

No furnace testing was conducted during this reporting period due to emphasis on the diagnostic analysis of FLS-1 test results. In the course of this analysis, however, many cladding/spacer-grid interaction tests were performed at room temperature (in air), using both simulated and prototype hardware. The effect of surface treatment of the spacer-grid material on frictional interaction with the cladding was studied in an effort to find a friction-reducing treatment for existing spacer-grids intended for the FLS-2 assembly. Treatments studied were electropolishing, electroless nickel plating, carburizing, and chromium electroplating. In addition to these tests, the LASL simulated spacer-grid design used in FLS-1 and intended for FLS-2 was compared with a 31-rod spacer-grid of GCFR prototype configuration furnished by General Atomic Company (GAC). Tentative conclusions from this work are:

1. Significant reduction in friction by surface treatment appears doubtful and
2. Friction forces in the GAC hardware are significantly greater than in the LASL hardware due to both increased friction factor and the geometry of the GAC spacer grid.

Examination of alternate means of expanding data acquisition capabilities of the present HP 3052-A system was begun. Requirements in DMFT tests for 160 data channels and 4 control functions have been identified (we now have 50 data channels and 1 control). Much higher data sampling rates are required than the minimum of 3s observed in 37-rod FLS tests.

A benchmark program has been initiated to clean up software on the present HP system to assess more truly its full capabilities.

508 172

VI. CONTAINMENT SYSTEMS EVALUATION AND STUDIES

(R. G. Gido, Q-6)

The following sections summarize the technical accomplishments for two FY 78 projects in the reactor containment area funded by the NRC/Division of Systems Safety (DSS). Work for the first project titled "Containment Evaluation," is described in Sec. A. Progress in the second project titled "Containment Subcompartment Analysis," is presented in Sec. B.

A. Containment Evaluation

(R. G. Gido, Q-6)

The MOD-2 version of COMPARE has been prepared for release to the National Energy Software Center and a user's manual has been drafted. This version features solution of the one-dimensional compressible flow equations by the method of characteristics. References 6, 39, and 40 discuss this feature and provide comparisons of MOD-2 and MOD-1⁴¹ calculated results. The following capabilities are also available in conjunction with the method of characteristics solution: (i) discontinuous area change, (ii) internal duct orifice, (iii) branching flow,⁴² and (iv) closed-end duct. The necessary future evaluations of the MOD-2 version are scheduled for FY 79.

B. Containment Subcompartment Analysis

1. Insulation Blockage Sensitivity Study

(J. S. Gilbert, Q-6)

The sensitivities of reactor vessel pressures, forces, and moments to blockage of reactor cavity flow areas were determined. The blockages simulate the closure of specific flow areas by pieces of insulation loosened during a hot- or cold-leg piping break. In all cases, the selected flow areas are completely blocked at the beginning of blowdown and remain so during the transient.

The description of the insulation blockage locations and the reactor cavity flow areas is given in Table XIX and Figs. 101-103.

Forces and moments on the reactor vessel are defined using the x-, y-, z-coordinate system of Fig. 103. The z-axis is the vertical centerline of the reactor vessel with the top of the reactor vessel in the positive z-direction. The x- and y-axes form a horizontal plane through the centerlines of the reactor vessel nozzles. The break volume is located along the positive x-axis; hence, maximum net forces on the reactor vessel are in the negative x-direction with resulting moments about the y-axis. Because of

TABLE XIX
INSULATION BLOCKAGE LOCATION DESCRIPTION

Case No.	Connected Nodes of Blocked Junction (See Figs. 101 and 102)	Description of Blocked Flow Area
1	8 to 14	Blowdown volume junction with inspection tunnel volume.
2	7 to 1 and 1'	Nozzle 1 piping penetration volume junction with annulus volume.
3	9 to 2 and 2'	Nozzle 2 piping penetration volume junction with annulus volume.
4	17 and 18 to 44	Remote inspection tunnel volume junctions with containment volume.
5	28 and 29 to 44	Upper annulus volume junctions with containment volume.
6	22 and 23 to 34	Annulus volume junctions below nozzles 1 and 2.
7	29 to 30 23 to 24	Annulus volume junctions above and below nozzle 2.
8	31 to 32 25 to 26	Annulus volume junctions above and below nozzle 3.
9	42 to 43	Junction between lower reactor cavity and instrumentation tunnel.
10	1 and 2 to 1' and 2'	Junctions between nozzles 1 and 2.

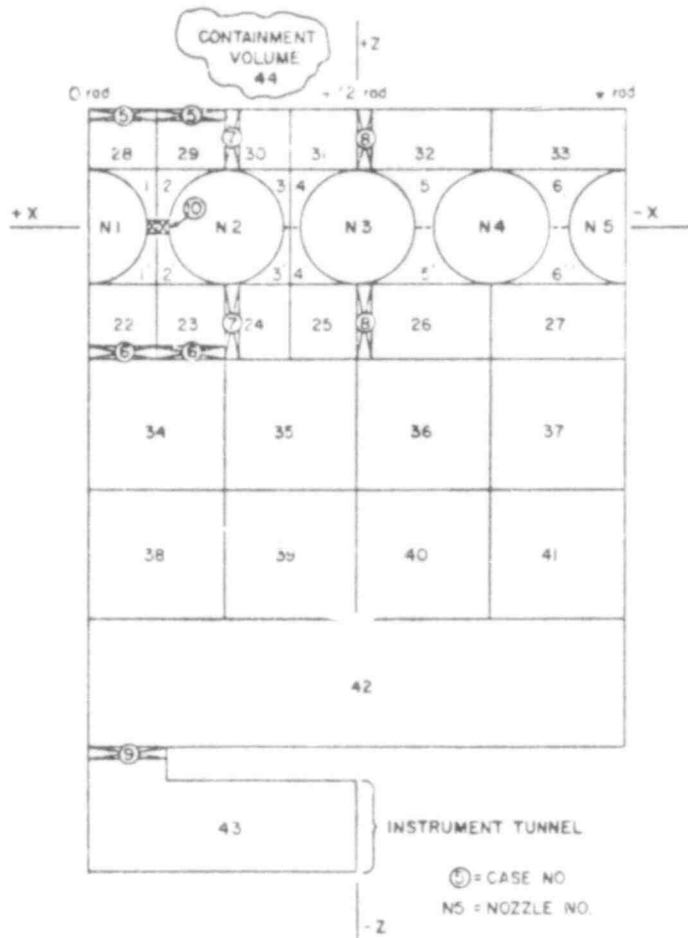


Fig. 101. Unwrapped side view of reactor cavity annulus nodes with insulation blockage locations indicated.

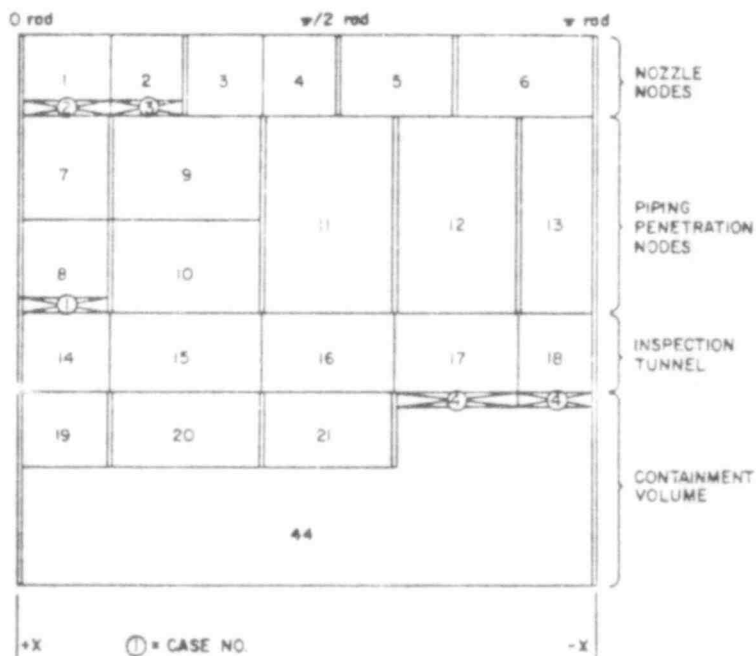


Fig. 102. Insulation blockage locations indicated in unwrapped top view of nodes around the nozzles and piping penetration nodes.

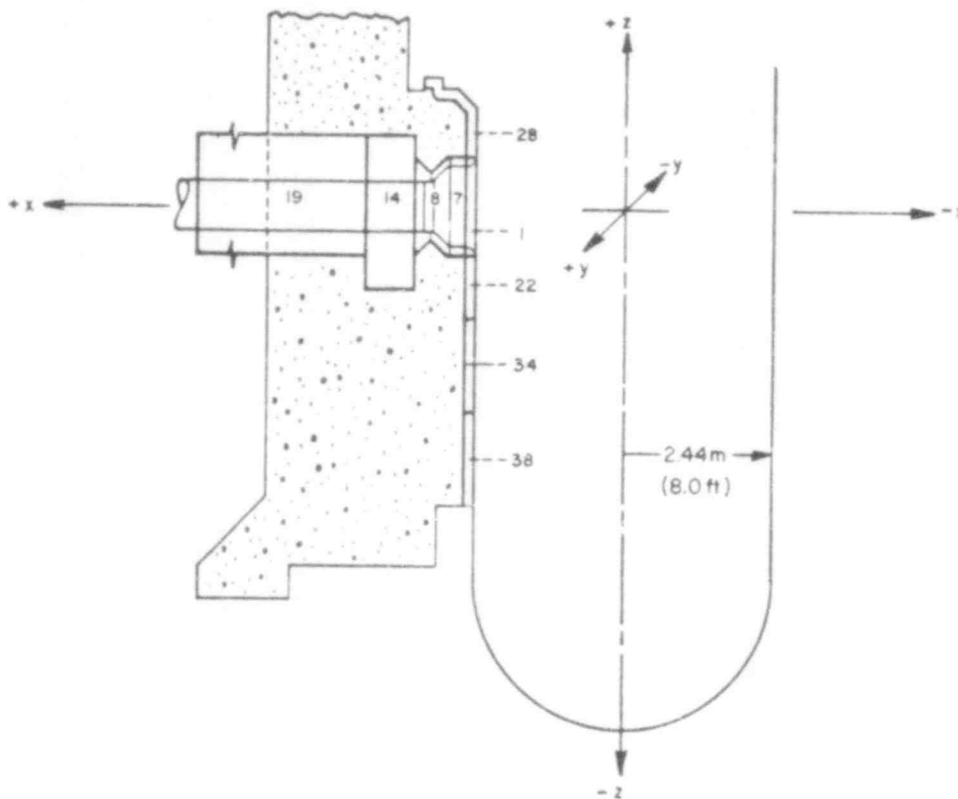


Fig. 103. Vertical cross section of the reactor vessel with nodalization and coordinate system indicated.

the assumed symmetry of blowdown flow about the reactor vessel, there are no net y -forces on the vessel and thus there are no net moments about the x -axis.

The results of the study are given in Table XX. As used in this study, the term "sensitive" is defined as a positive or negative variation, from the best estimate value results, of more than 35% of either maximum pressures, maximum forces, or maximum moments. The results are briefly summarized as follows.

1. The maximum pressure is sensitive to the reduction of flow areas near the blowdown volume. This reduction of area increases the flow resistance for the blowdown mass and energy exiting the blowdown volume.
2. The maximum x -force is sensitive to the reduction of flow areas near the x -axis. This reduction of area reduces the dispersion of blowdown mass and energy to regions away from the x -axis.

TABLE XX

MAXIMUM VALUES OF SELECTED PRESSURES, FORCES, AND MOMENTS
RESULTING FROM INSULATION BLOCKAGE OF VARIOUS
REACTOR CAVITY FLOW AREAS

Case No.	Positive Moment about y-axis (kN-m)	Negative Moment about y-axis (kN-m)	Positive z-force (kN)	Negative x-force (kN)	Pressure in Blowdown Volume (kPa)
1	1458.	570.	734.	8585.	9701.
2	249.	82.	138.	231.	3296.
3	1232.	284.	343.	2544.	3054.
4	1164.	391.	369.	1704.	3054.
5	637.	1548.	325.	2678.	3054.
6	2204.	--	334.	3083.	3054.
7	2339.	--	374.	3554.	3054.
8	1164.	1175.	311.	2740.	3054.
9	1164.	383.	907.	1802.	3054.
10	1345.	570.	311.	1868.	3054.
Best Estimate Value	1164.	383.	302.	1802.	3054.

3. The maximum z-force is sensitive to significant mass and energy increases or decreases in the region below the reactor vessel.
4. The maximum moments about the y-axis are sensitive to the reduction of flow areas near the nozzles. These reductions alter the dispersion of mass and energy above and below the nozzles, and therefore, the moment about the y-axis.

In conclusion, maximum pressure and reactor vessel forces and moments may be sensitive to insulation blockage. This conclusion may be altered for analyses which more mechanistically represent possible insulation blockage. For this reason, additional studies are required. In particular, analyses of the (1) mechanisms for breakup of the insulation, (2) transport of the insulation, and (3) blockage characteristics (i.e., resistance to displacement) are recommended.

2. Loss-Coefficient Compressibility Effects

(A. Koestel, LASL Consultant; and R. G. Gido, Q-6)

Comprehensive quasistatic compressible flow relationships were developed to account for compressibility and two-phase effects for abrupt area changes. In particular, a method of accounting for the vena contracta at an abrupt area decrease (contraction) and the effect of compressibility on an abrupt area increase (expansion) were developed. Figure 104(a-c) describes the geometry

considered. Two-phase accounting is accomplished through the isentropic exponent utilized in the analytical relationships.

Flow through an abrupt enlargement in area, as shown in Fig. 104(a), experiences a loss in total pressure. This loss in total pressure is conventionally represented by a velocity head loss coefficient (K) defined as:

$$K = \frac{P_{T1} - P_{T2}}{\frac{\rho_1 u_1^2}{2}}, \quad (14)$$

where

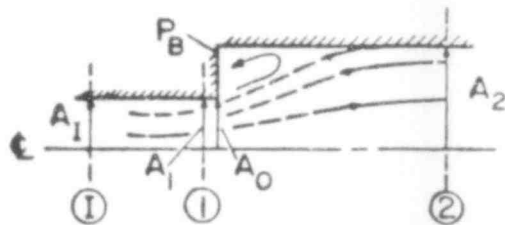
P_T = total pressure,

u = velocity,

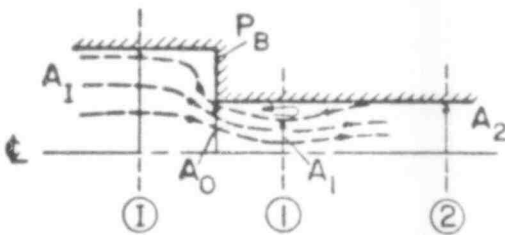
ρ = density, and

1,2 = station number.

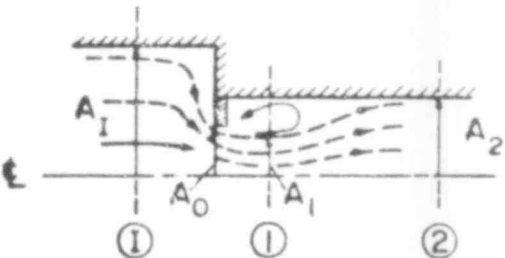
A similar expression can be used to represent a contraction loss, turning loss, etc. Figure 104 depicts flow streamlines for an abruptly contracting flow [Fig. 104(b)] and a general case of



(a) EXPANSION (NO CONTRACTION)
 $A_1 = A_0 < A_2, A_1 = A_0, \hat{C} = 1.0$



(b) CONTRACTION (ISENTROPIC CONTRACTION + EXPANSION)
 $A_1 > A_0, A_0 = A_2 > A_1, A_1 = \hat{C} A_0$



(c) GENERAL CASE
 $A_1 > A_0, A_0 < A_2, A_1 = \hat{C} A_0$

Fig. 104. Abrupt flow area change geometries.

contracting and expanding flow [Fig. 104(c)], which includes the previous two cases. Note that the contracting flow entails an expansion from the vena contracta to the downstream flow area. In Fig. 104, station I represents the upstream or inlet conditions, station 1 is the minimum flow area (maximum velocity) point and station 2 the downstream location, A_0 is the minimum geometric area, and \hat{C} is the ratio A_1/A_0 . The face pressures (P_B) shown appear in conservation of momentum equations.

In all cases shown in Fig. 104, the loss in total pressure results from an expansion. Friction during the acceleration part of the contraction process is known to be negligibly small.⁴³⁻⁴⁵ As an example, consider the determination of flow losses for the general case of Fig. 104(c), which includes the simple contraction and expansion cases. First, the flow conditions at station 1, based on the flow at station I and the area ratio A_I/A_0 , would be determined. Then, the ratio of vena contracta area (A_1) to the minimum geometric area (A_0), i.e., \hat{C} , would be calculated. Finally, the expansion loss from station 1 to station 2 would be determined.

The general approach used is based on the ideal gas compressible flow relations, e.g., Refs. 46 and 47. A homogeneous air-steam-liquid water mixture is assumed. As a result, the effect of two-phase flow is readily incorporated into the equations via the isentropic exponent (γ), an inherent parameter. The procedures were developed for convenient use in conventional subcompartment analysis codes such as the COMPARE code.⁴¹

References 48 and 49 have developed the relationship between the vena contracta coefficient \hat{C} and compressibility. The resulting equations are:

$$\hat{C} = \frac{z}{r^{1/\gamma} B} \left[1 - \sqrt{1 - \frac{Br^{2/\gamma}}{z^2}} \right], \quad (15)$$

where

$$z = \frac{\gamma}{\gamma-1} \left(\frac{r^{2/\gamma} - r^{\frac{\gamma+1}{\gamma}}}{1 - r} \right),$$

$$B = z \left[\left(\frac{A_0}{A_I} \right)^2 + \frac{2}{\hat{C}_i} - \frac{1}{\hat{C}_i^2} \right] - \left(\frac{A_0}{A_I} \right)^2 r^{2/\gamma} ,$$

$$r = \frac{P_1}{P_I} ,$$

P_1 = station 1 station pressure, and

P_I = station I static pressure.

Note that the incompressible vena contracta \hat{C}_i value is required. This is a well-founded relationship.⁴⁵ Figure 105 is an example of applying these compressible vena contracta equations.

The effect of compressibility on the expansion loss coefficient, defined by Eq. (14), was developed by application of the conservation of momentum and the compressible flow equations. A similar development, in terms of Mach number (M), was made in Ref. 43. The pertinent equations that result are

$$K = \frac{\left(1 + \frac{\gamma-1}{2} M_1^2 \right)^{\frac{\gamma}{\gamma-1}} \left(1 - \frac{P_{T2}}{P_{T1}} \right)}{\frac{\gamma}{2} M_1^2} ,$$

$$\frac{P_{T2}}{P_{T1}} = \frac{A_1 M_1}{A_2 M_2} \left[\frac{1 + \frac{M_2^2}{2}(\gamma-1)}{1 + \frac{M_1^2}{2}(\gamma-1)} \right]^{\frac{\gamma+1}{2(\gamma-1)}} ,$$

$$M_2^2 = \frac{1 - 2\gamma J^2 \pm \sqrt{1 - 2J^2(1+\gamma)}}{2J^2\gamma^2 - \gamma + 1} , \text{ and}$$

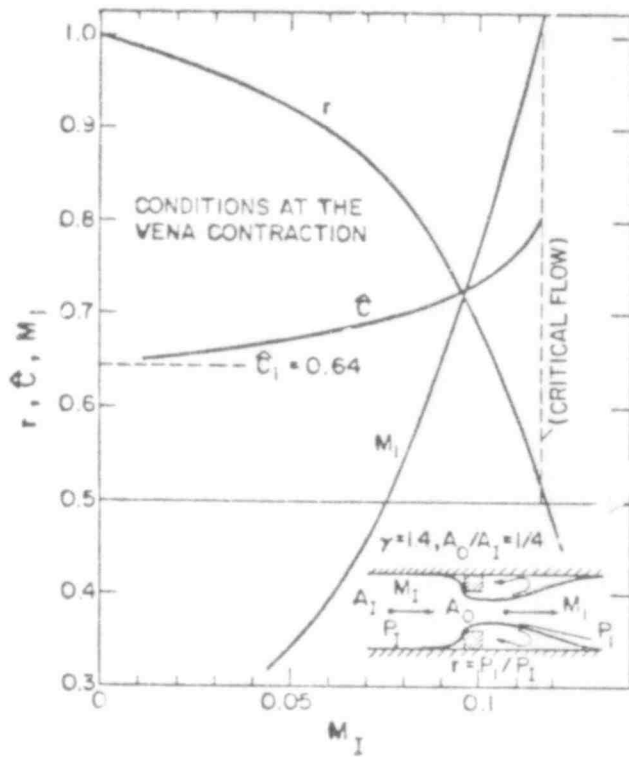


Fig. 105. Curves for r , \hat{C} , and M_1 for $\gamma = 1.4$ and $A_0/A_1 = 1/4$ (M is Mach number).

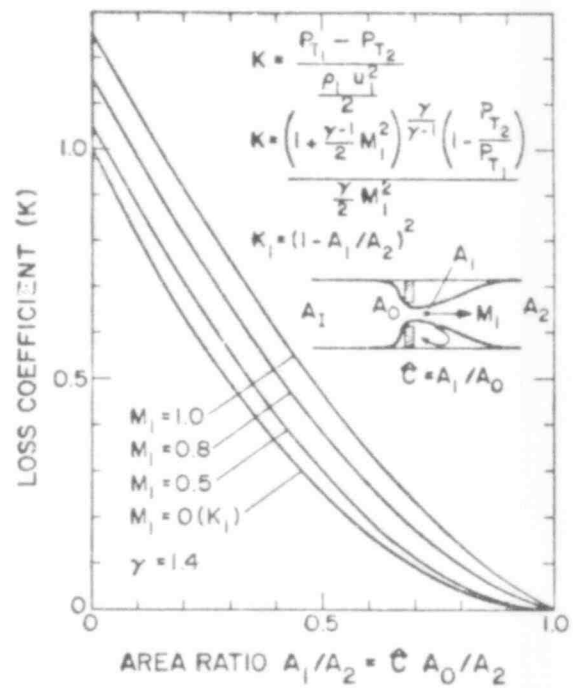


Fig. 106. Compressible expansion loss coefficient for $\gamma = 1.4$.

$$J = \frac{M_1 \sqrt{1 + \frac{M_1^2}{2}(\gamma - 1)}}{1 + \gamma M_1^2 + \frac{P_B}{P_1} \left(\frac{A_2}{A_1} - 1 \right)}$$

Values of γ and M_1 are known from the conditions at the minimum area, which could be a vena contracta. In addition, a convenient and reasonable assumption is that $P_B/P_1 \approx 1$.^{43,44} Figure 106 presents the results of applying these equations for $\gamma = 1.4$.

REFERENCES

1. E. M. Sparrow and R. D. Cess, Radiation Heat Transfer (Brooks/Cole Publishing Co., Belmont, California, 1966).
2. R. Siegel and J. R. Howell, Thermal Radiation Heat Transfer, (McGraw-Hill Book Co., New York, NY, 1972).
3. R. Deruaz and B. Petitpain, "Modeling of Heat Transfer by Radiation During the Reflooding Phase of a LWR," presented at the Specialists' Meeting on the Behavior of Water Reactor Fuel Elements Under Accident Conditions (Spatind, Norway, September 1976).
4. S. S. Dua and C. L. Tien, "A Generalized Two-Parameter Relation for Conduction-Controlled Rewetting of a Hot Vertical Surfaces," Int. J. Heat Mass Transfer, 20, 174-176 (1977).
5. S. K. W. Yu, P. R. Farmer, and M. W. E. Coney, "Methods and Correlations for the Prediction of Quenching Rates on Hot Surfaces," Int. J. Multiphase Flow 3, 415-443 (1977).
6. J. F. Jackson and M. G. Stevenson, "Nuclear Reactor Safety Quarterly Progress Report for the Period January 1-March 31, 1978," Los Alamos Scientific Laboratory report LA-7278-PR (1978).
7. B. Collins, H. Craps, and K. Sackett, "Experimental Data Report for Semiscale MOD-1 Test S-02-6," EG&G Idaho report TREE-NUREG-1037 (January 1977).
8. J. F. Jackson and M. G. Stevenson, "Nuclear Reactor Safety Quarterly Progress Report for the Period July 1-September 30, 1977," Los Alamos Scientific Laboratory report LA-7039-PR (1977).
9. Ericson, L. Gros d'Aillon, D. Hall, J. Ravensborg, O. Jervag, and H. Akesson, "The Marviken Full-Scale Critical Flow Test Interim Report, Results from Test 4," Marviken report MX3-40 (May 1978).
10. Michael D. McKay, W. J. Conover, and Richard J. Beckman, "A Comparison of Three Methods for Selecting Input Variables in the Analysis of Output from a Computer Code," to appear in Technometrics.
11. Robert V. Hogg and Allen T. Craig, Introduction to Mathematical Statistics, 2nd Edition (MacMillan Co., New York, NY, 1965), p. 182.
12. Albert H. Bowker and Gerald J. Lieberman, Engineering Statistics (Prentice-Hall, Inc., New York, NY, 1959), p. 224.

13. S. S. Shapiro and M. B. Wilk, "An Analysis of Variance Test for Normality (Complete Samples)," *Biometrika* 52, 591-611 (1965).
14. J. F. Jackson and M. G. Stevenson, "Nuclear Reactor Safety Quarterly Progress Report for the Period April 1-June 30, 1978," Los Alamos Scientific Laboratory report LA-7481-PR (1978).
15. J. R. Travis, C. W. Hirt, and W. C. Rivard, "Multidimensional Effects in Critical Two-Phase Flow," to be published in *Nuclear Science and Engineering*.
16. J. K. Dukowicz, "A Particle-Fluid Model for Liquid Sprays," (to be published in *J. Comp. Phys.*).
17. J. R. Travis, F. H. Harlow, and A. A. Amsden, "Numerical Calculation of Two-Phase Flows," *Nuclear Science and Engineering* 61, 1-10 (1976).
18. C. W. Hirt, B. D. Nichols, and N. C. Romero, "SOLA-A Numerical Solution Algorithm for Transient Fluid Flows," Los Alamos Scientific Laboratory report LA-5852 (1975).
19. H. Hiroyasu and T. Kadota, "Fuel Droplet Size Distribution in Diesel Combustion Chamber," Society of Automotive Engineering paper no. 740715 (1974).
20. D. A. Barnard, J. A. Ward, and P. B. Whalley, "Two-Phase Flow in a PWR Upper Plenum -- An Experimental Study Using Air and Water," Atomic Energy Research of England Harwell report G 1047 (1978).
21. J. C. Dallman, W. L. Kirchner, and V. Starkovich, "De-entrainment Phenomena from Droplet Cross Flow in Vertical Rod Bundles," Proc. of the ANS Winter Meeting (Washington, DC, 1978).
22. Minutes of 2D/3D Technical Consultation Meeting, U.S. Nuclear Regulatory Commission (July 13, 1978).
23. Ervin E. Underwood, Quantitative Stereology, (Massachusetts, Addison-Wesley Publishing Co., 1970).
24. C. R. Bell and J. E. Boudreau, "Application of SIMMER-I to the Postdisassembly Fluid Dynamic Behavior Within an LMFBR Reactor Vessel," Los Alamos Scientific Laboratory, (private communication).
25. C. R. Bell, P. B. Bleiweis, J. E. Boudreau, F. R. Parker, and L. L. Smith, "SIMMER-I: An S_n , Implicit, Multifield, Multi-component, Eulerian, Recriticality Code for LMFBR Disrupted Core Analysis," Los Alamos Scientific Laboratory report LA-NUREG-6467-MS (January 1977).

26. L. L. Smith, "SIMMER-II: A Computer Program for LMFBR Disrupted Core Analysis," Los Alamos Scientific Laboratory report LA-7515-M (November 1978).
27. M. D. McKay, J. W. Bolstad, and D. E. Whiteman, "An Application of Statistical Techniques to the Analysis of Reactor Safety Codes," Proc. ANS Topical Mtg., Probabilistic Analysis of Nuclear Reactor Safety (Los Angeles, California, 1978), p. II-9.
28. R. D. Burns, III and L. B. Luck, "Statistical Analysis of SIMMER-II Results," ANS Trans. 28, 513 (1978).
29. R. D. Burns, III and J. H. Scott, "Statistical Analysis of Seventeen TREAT Experiments," Accepted for presentation by the American Nuclear Society Winter Meeting (Washington, DC, November 1978).
30. C. R. Bell, R. D. Burns, III, and L. B. Luck, "Impact of SIMMER-II Model Uncertainties on Predicted LMFBR Postdisassembly Dynamics," Los Alamos Scientific Laboratory (private communication).
31. W. J. Conover, Practical Nonparametric Statistics (Wiley Publishing Co., New York, New York, 1971), p. 249.
32. M. G. Kendall, Rank Correlation Methods (Hafner Publishing Co., New York, New York, 1955).
33. R. E. Holtz, B. W. Spencer, J. J. Testa, and N. A. Kramer, "Loss-of-Flow Test R-7 (Interim Report)," Argonne National Laboratory report ANL/RSA 76-8 (January 1976).
34. B. W. Spencer, "Summary and Evaluation of R-Series Loss-of-Flow Safety Tests in TREAT," Chicago Fast Reactor Safety Meeting paper CONF 761001 (1976), pp. 1647-1657.
35. M. A. Grolmes, "Heat Capacity Effects in Sodium Boiling," Trans. Am. Nucl. Soc. 22, 407 (1975).
36. M. Ishii, W. L. Chen, and M. A. Grolmes, "Multichannel Clad Relocation Model for Fast Reactor Loss-of-Flow Accidents," Argonne National Laboratory report ANL/RAS 78-2 (January 1978).
37. Public Service Co. of Colorado, "Fort St. Vrain Nuclear Generating Station, FSAR," Atomic Energy Docket No. 50267 (undated).
38. W. A. Coffman and L. L. Lynn, "WATER: A Large Range Thermodynamic and Transport Water Property FORTRAN-IV Computer Program," Bettis Atomic Power Laboratory report WAPD-TM-568 (December 1968).

39. James F. Jackson and Michael G. Stevenson, "Nuclear Reactor Safety Quarterly Progress Report for the Period October 1-December 31, 1977," Los Alamos Scientific Laboratory report LA-7195-PR (February 1978).
40. R. G. Gido, R. G. Lawton, C. I. Grimes, and J. A. Kudrick, "Compressible Subcompartment Analysis," American Nuclear Society Trans. V 23, 307-308 (Toronto, Canada, June 14-18, 1978).
41. R. G. Gido, J. S. Gilbert, R. G. Lawton, and W. L. Jensen, "COMPARE-MOD 1: A Code for the Transient Analysis of Volumes with Heat Sinks, Flowing Vents, and Doors," Los Alamos Scientific Laboratory report LA-7199-MS (March 1978).
42. R. W. Meier and R. G. Gido, "One-Dimensional Calculation of Flow Branching Using the Method of Characteristics," Los Alamos Scientific Laboratory report LA-7306-MS (May 1978).
43. A. R. Shouman and J. L. Massey, Jr., "Stagnation Pressure Losses of Compressible Fluids Through Abrupt Area Changes Neglecting Friction at the Walls," ASME paper 68-WA/FE-46 (1968).
44. R. P. Benedict, J. S. Wyler, J. A. Dudek, and A. R. Gleed, "Generalized Flow Across an Abrupt Enlargement," ASME paper 75-WA/FM-1 (1975).
45. R. P. Benedict, N. A. Carlucci, and S. D. Swetz, "Flow Losses in Abrupt Enlargements and Contractions," J. Eng. for Power, 73 (January 1966).
46. A. H. Shapiro, The Dynamics and Thermodynamics of Compressible Fluid Flow, V.I. (Ronald Press, New York, New York, 1953).
47. H. W. Liepman and A. E. Puckett, Introduction to Aerodynamics of a Compressible Fluid (John Wiley and Sons, New York, New York, 1947).
48. R. G. Cunningham, "Supercritical Flow Through a Square-Edged Orifice," Proc. of the Midwestern Conference on Fluid Dynamics, University of Illinois (May 12-13, 1950), pp. 372-388.
49. E. Buckingham, "Note on Contraction Coefficients of Jets of Gas," Bureau of Standards J. of Research 6, 765-775 (1931).

POOR ORIGINAL

Available from
US Nuclear Regulatory Commission
Washington, DC 20555

Available from
National Technical Information Service
Springfield, VA 22161

Microfilm	5.300	126.350	7.25	251.275	10.75	376.400	13.00	501.525	15.25
901-025	4.00	151.175	8.00	276.300	11.00	401.425	13.25	526.550	15.50
026-050	4.50	176.200	9.00	301.325	11.75	426.450	14.00	551.575	16.25
051-075	5.15	201.225	9.25	326.350	12.00	451.475	14.50	576.600	16.50
076-100	6.00	226.250	9.50	351.375	12.50	476.500	15.00	601-up	- 1
101-125	6.50								

1. Add \$2.50 for each additional 100 page increment from 601 pages up.